Carnegie Mellon University

CARNEGIE INSTITUTE OF TECHNOLOGY

THESIS

SUBMITTED IN PARTIAL FULFILLMENT OF THE REQUIREMENTS

FOR THE DEGREE OF Doctor of Philosophy

TITLE   Probing the Phase Behavior of Complex Fluids using

Microliter Droplet Reactors

PRESENTED BY   Christopher William Nelson

ACCEPTED BY THE DEPARTMENT OF

Mechanical Engineering

Shelley L. Anna	5/2/2016
ADVISOR, MAJOR PROFESSOR	DATE
Allen L. Robinson	5/2/2016
DEPARTMENT HEAD	DATE

APPROVED BY THE COLLEGE COUNCIL

James H. Garrett Jr.	5/2/2016
DEAN	DATE

Probing the Phase Behavior of Complex Fluids using Microliter Droplet Reactors

Submitted in partial fulfillment of the requirements for

the degree of

Doctor of Philosophy

in

Mechanical Engineering

Christopher W. Nelson

B.S., Mechanical Engineering, University of South Florida
M.S., Mechanical Engineering, Carnegie Mellon University

Carnegie Mellon University
Pittsburgh, PA

April, 2016

Acknowledgements

During our first meeting, the weekend of my recruitment, Shelley said two things that have stuck in my mind. First, she said that it wasn't up to me to worry about my funding, that was her responsibility. Second, she said that her goal as my advisor was to train me to become her peer. Shelley has delivered on the former, but I'm still working on holding up my end of the latter!

This thesis is the product of the help, support, and opportunities I've been provided by a great number of people. First, of course, I would like to thank my advisor, Professor Shelley Anna, for her help, patience, and guidance both in my research and as a mentor. She has believed in me more than I've believed in myself. I would like to thank my committee members, Professors Lynn Walker, Steve Garoff, and Ryan Sullivan. In particular, Lynn has been an informal co-advisor for my work on and outside the Dow project and has contributed significantly to my academic and professional success. Steve has provided great discussions and comments regarding the work presented in Chapter 2 and the manuscript is better for it. Ryan has provided me with great feedback as well as opportunities to think about interesting problems outside my field, like how to entrain aerosols in microfluidic flows.

I would also like to thank the fantastic friends I've made during my time at CMU, especially the people I've worked with in the CFE offices. In particular, the friendship of Sharon, Anthony, Stephanie, Melissa, Javier, and Sarah and their continued willingness to put up with me for nearly 5 years. I'll be graduating with

my sanity mostly intact thanks to their companionship and kind words. I was adopted by the ChemE department and I'm grateful for all of the people I've been able to know.

Most of all, though, I would like to thank my wife, Sarah, for her endless support and encouragement. She has kept me in one piece for nearly a decade. I wouldn't be here today if not for her, and for the support and love of my family and my friends outside of CMU. Thank you!

> *"Nothing in this world can take the place of persistence. Talent will not; nothing is more common than unsuccessful people with talent. Genius will not; unrewarded genius is almost a proverb. Education will not; the world of full of educated derelicts. Persistence and determination alone are omnipotent. The slogan 'press on' has solved and always will solve the problems of the human race"*
>
> *-Attributed to Calvin Coolidge*

Abstract

Microfluidic droplet-based techniques allow for the formation of extremely uniform emulsions with precise control over the contents of each phase. In this thesis, we exploit these small scale fluid manipulation techniques to study several related phenomena in the area of complex fluids engineering: phase separation and dewetting in three-phase liquid systems, partitioning of high value nanomaterials, and the coalescence and creaming of dilute oil-in-water emulsions. Phase separation occurs, for example, in aqueous systems composed of two or more dissimilar polymers. Using a model system composed of polyethylene glycol, dextran, and water, we study dehydration-driven wetting transitions in a microfluidic array-type device, and then use this technique to estimate the very low interfacial tension between the aqueous phases as a function of polymer concentration. Next, we scale up the droplet-based fluid handling techniques to develop a millifluidic platform for screening the effect of water clarifiers on the stability of dilute crude-oil-in-water emulsions. Finally, the tools and techniques previously developed are adapted and extended to study aqueous two phase extraction, which has recently emerged as a promising technique for sorting synthetic nanomaterials such as single walled carbon nanotubes. The partition coefficient of a nanotube depends on many system parameters, including the presence and concentration of surfactants and salts, and the properties of the phase forming polymers. Knowledge of these relationships provides insight into the fundamental processes governing partitioning and are required for rational design of large scale separation processes. We demonstrate that a microliter scale

droplet-based fluid handling approach coupled with inline absorption spectroscopy can facilitate the identification and optimization of the critical parameters for aqueous two phase extraction of carbon nanotubes. The primary contribution of this thesis is a set of robust tools and techniques to quickly, and with high compositional resolution, quantify phenomena such as phase change and partitioning in complex fluid systems.

Table of Contents

List of Tables

List of Figures

Chapter 1. Introduction

Complex fluids are liquid mixtures containing polymers, particles, surfactants, or finely dispersed immiscible fluid droplets. The observed macroscale complexity associated with these systems results from the molecular and microscale interactions that occur between the various components. These interactions often give rise to striking, non–linear behavior. A familiar example is the mechanical response of a shear thickening fluid such as cornstarch (a high molecular weight polysaccharide) dispersed in water. At low shear rate conditions, such as slowly inserting one's hand into the solution, the mixture behaves like a viscous liquid. At high shear rate conditions, such as when the surface of the liquid is forcefully struck, the viscosity of the liquid increases dramatically. Complex fluids appear in applications as diverse as personal care products, in the form of foams, gels, and lotions, in food products, such as mayonnaise and salad dressing, and in coatings, pharmaceuticals and adhesives.

In addition to their interesting mechanical responses, complex fluids can exhibit unique phase behavior. Small compositional changes can transform liquids into gels, stable emulsions into separated phases, and particle suspensions into precipitated sediments. These phase changes are almost always accompanied by optical changes. The response of complex fluid systems to compositional changes is often non-linear and non-monotonic. Further complicating matters, many complex fluid systems, such as paints, include dozens of different additives. The competing effects of these additives make it challenging to predict the phase behavior of these systems. For most applications, quantitative understanding of

the phase behavior of a system requires conducting tens to hundreds of experiments spanning an often multi-dimensional parameter space. These experiments are time consuming, labor intensive, and require large quantities of analytes, which may be newly synthesized (in small quantities) or expensive.

Recently, small scale, high-throughput fluid manipulation techniques enabled by microfluidic devices have emerged. These technologies center on the manipulation of liquids in geometries with very small characteristic length scales, often of the order of tens to hundreds of microns. Fluid flow in devices with microscale dimensions is generally laminar, and interfacial effects, which often play a critical role in phase behavior, are significantly more important than inertia, gravity, and viscous stresses. Microfluidic techniques allow for the formation, manipulation, and observation of highly organized fluid structures, particularly emulsions. Droplet-based microfluidic techniques involve the formation of nanoliter to microliter scale fluid compartments dispersed in a second immiscible phase carrier fluid. While similar in character to macroscopically produced emulsions, the spatial distribution of the fluid compartments generated by microfluidics is often highly ordered, and the droplet size is extremely monodisperse. Individual droplets can be tracked and manipulated in repeatable and reliable ways. The composition of these fluid compartments can be varied from droplet to droplet, and changes in the optical and mechanical properties of the individual droplets can be monitored. These methodologies require microliters of sample and droplets can be generated at rates of the order of tens to hundreds per second.

In this thesis we use tools and techniques from droplet-based microfluidics to study the phase behavior of complex fluid systems.

In **Chapter 2**, a microfluidic device is used to generate arrays of approximately 40 identical droplets with volumes of 8 – 10 nanoliters. The droplets are physically immobilized such that they can be observed for durations of tens of hours. The droplets contain two incompatible polymers dissolved in water at low concentration. Due to the small but finite permeability of the microfluidic device, water diffuses out of the droplets, slowly changing the internal composition. As the droplets dehydrate, the overall concentration of the two polymers increases, leading to phase separation due to binodal decomposition at sufficiently large concentrations. Because the two-phase droplets are suspended in a third mineral oil phase, a three-phase contact line appears at the junction of the two droplet phase fluids and with the continuous phase oil. By measuring the evolution of the droplet volume as a function of time, as well as the contact angles between the three phases, we estimate the very low interfacial tension between the two polymer rich phases as a function of total polymer composition. This technique enables, in a single experiment, the determination of the interfacial tension as a function of polymer concentrations. In particular, the device can probe polymer compositions that are essentially inaccessible in macroscale experiments.

In **Chapter 3**, a new droplet-based fluid handling platform is introduced based on the idea of slightly scaling up the methods associated with microfluidics. By increasing the characteristic length scales of the device (i.e. the tubing

diameter) from hundreds of microns to one or two millimeters, we are able to design a platform which retains all of the fluid handling benefits of traditional microfluidics, but with an optical path length that allows for in-situ per-droplet measurements of optical absorption. An additional benefit of this scaled up approach is that the device can now be constructed from off-the-shelf commercial tubing and fittings, which decreases the cost and expands the materials available for construction. Finally, we evaluate the ability of the platform to generate trains of droplets with a linear gradient in composition, and detect compositional gradients using absorption spectroscopy.

In Chapters 4 and 5 we apply the millifluidic device that we developed and demonstrated in Chapter 3 toward two challenging and industrially relevant problems in the realm of complex fluids. In **Chapter 4** we investigate the effect of polyelectrolyte water-clarifiers on the stability of dilute crude-oil-in-water emulsions. This is accomplished by first forming oil-in-water emulsions using macroscale techniques, then injecting the emulsions into microliter aqueous droplet compartments, which are suspended in an immiscible perfluorocarbon carrier phase fluid. The droplets simulate the composition of produced water generated from oil recovery operations. The droplets are dosed with varying concentrations of potential water clarifying agents, and the effects are observed through optical microscopy and absorption spectroscopy. The platform enables these experiments to be performed quickly, and with very high compositional resolution, in contrast to the laborious macroscale 'bottle tests' that are typically

performed. We find a relationship between polymer molecular weight and concentration of polymer required to destabilize the emulsion.

In **Chapter 5** the millifluidic platform is employed to measure the partition coefficient of carbon nanotubes in an aqueous two phase system as a function of added surfactant concentration. This is accomplished by generating two-compartment droplets containing an aqueous two phase system similar to the one studied in Chapter 2. By carefully controlling the velocity of the droplets and the orientation of the droplets relative to gravity, we are able to affect spatial separation of the two aqueous phases and measure an effective partition coefficient of several different multi-species samples of single walled carbon nanotubes. The apparatus replaces the error prone, laborious, and time consuming process of measuring partition coefficients for these high value nanomaterials.

Finally, in **Chapter 6**, we summarize the findings and conclusions of the previous four chapters and discuss opportunities and challenges for future work.

Chapter 2. Using controlled dehydration of a compound nanoliter droplet to estimate the interfacial tension of phase-separated aqueous polymer mixtures

2.1.   Introduction

Complex fluid mixtures containing polymers, colloidal particles, surfactants, salts, and multiple liquid phases are widely used in applications as varied as bioseparations, food, cosmetics, and enhanced oil recovery. At the correct compositions, mixtures containing incompatible polymers or polymers and certain salts will phase separate into two or more liquid phases[1,2]. These aqueous two phase systems contain separated components that are mutually immiscible and exhibit a very low interfacial tension, of the order of 0.001 to 1 mN/m[3–5]. These properties are useful in many applications. For example, knowledge of the phase separation of incompatible biopolymers is used to control the consistency and mouth feel of foods[6]. In enhanced oil recovery, ultralow interfacial tension in emulsions and foams helps prevent capillary trapping phenomena that reduce extraction efficiency[7,8]. Extraction or separation methods using aqueous two phase systems are used to partition and purify biomolecules[9–11] and high value nanomaterials[12–14]. Their performance relies in part on the very low interfacial tension, the high water content[15], and the ability of the immiscible aqueous phases to be buffered.

Despite the importance of the interfacial tension in phase separated complex fluid systems, making accurate, precise, and repeatable measurements of their very low interfacial tension is extremely challenging. Standard techniques for measuring liquid-liquid interfacial tension[16] include approaches based on

measuring a force or a pressure, such as maximum bubble pressure, or drop weight methods, and approaches which rely on fitting the shape of a droplet or bubble, such as pendant drop and sessile drop methods. However, these techniques are generally ill-suited to making measurements of very low interfacial tension because the uncertainty associated with these measurements is often of the same order as the values being measured, or the very low interfacial tension between the phases makes it physically challenging to carry out the experiment without, for example, unwanted emulsification of the phases. In cases such as the pendant drop technique, the very small density difference between the phases, a defining feature of aqueous two phase systems, leads to unreliable measurements since gravitational effects are not able to sufficiently deform the droplets[17–19].

Progress has been made in addressing some of these limitations in the case of the pendant drop and sessile drop method, primarily through improved edge detection and shape fitting algorithms[18,20,21]. Still, we are aware of only a single report where the interfacial tension for an aqueous two phase system was made using drop shape analysis of a pendant or sessile droplet[22]. Additional challenges outside of limited precision include those associated with extensive sample preparation. Freshly mixed aqueous two phase systems can require days or even weeks to reach equilibrium when prepared at laboratory bench-top scales[22].

The most successful and widely used method for measuring extremely low interfacial tension with high precision is the spinning drop method[3–5,23–25]. The spinning drop method is a dynamic technique for measuring interfacial tension in which a small volume of one fluid phase is placed in the center of a transparent,

7

horizontally mounted tube filled with a second immiscible liquid phase. Rotating the tube at several thousand RPM leads to deformation of the droplet. The centrifugal force acting to elongate the drop is balanced by the interfacial tension, which acts to minimize the interfacial area. The interfacial tension is found by measuring the degree of droplet deformation as a function of the rotation rate and the densities of the two fluid phases[26,27]. The spinning drop method has several drawbacks; it requires relatively large sample volumes of at least one of the phases, extensive sample preparation, and many experiments must be performed at many different concentrations of the phase forming components in order to accurately determine the interfacial tension as a function of mixture composition. Additionally, the spinning drop method can be experimentally challenging to execute due to the nature of the rotating fluid-filled cylinder which must be spun up to several thousand RPM. The rotational motion of the tube induces recirculating flow patterns in the two liquid phases, which can lead to emulsification or migration of the droplet phase fluid, or lead to its contact with the container walls[28].

Construction of the phase diagram for a particular aqueous two phase system is also of considerable interest. A salient feature of the phase diagram is the binodal curve, which defines the threshold of concentrations of the two phase forming components that lead to phase separation, verses those that do not. The position and shape of the coexistence curve is a function of the type and concentration of phase forming species, temperature, and the presence and concentration of all additives, including salts and surfactants[29,30]. Rational design

of separation operations requires selecting an operating region of the phase diagram that optimizes extraction of the target product. Traditional methods for constructing phase diagrams, such as the cloud point method, involve carefully titrating in a concentrated solution of one of the phase forming components into a dilute mixture of the other until the solution mixture becomes cloudy. As with methods for measuring interfacial tension, this approach is labor intensive and time consuming.

We address some of these challenges and limitations by presenting a microfluidic approach and analysis methodology to estimate the interfacial tension that arises between the compartments of a phase separated mixture as a function of mixture composition. Additionally, we demonstrate the ability of this approach to simultaneously determine the phase diagram of the two phase system.

Several dynamic techniques for measuring interfacial tension using microfluidic approaches have been developed. The deformation of droplets as they pass through one or more expansions in a planar microchannel has been reported as a means to measure interfacial tension[31,32]. Similarly, interfacial tension was calculated based on the dynamics associated with droplet generation in a Y-shaped microfluidic device[33]. Other techniques use simultaneous measurement of the curvature of an interface, and the pressure drop across that interface, to solve the Young-Laplace equation for interfacial tension, in either a planar microfluidic device[34] or using a glass capillary submerged in a fluid reservoir[35]. To date, none of these techniques have been used to measure the interfacial tension of an aqueous two phase system.

Aqueous two phase systems have also been used extensively in other types of microfluidic devices. As summarized in a recent review paper by Hardt and Hahn[36], microfluidic techniques and methodologies have been combined with aqueous two phase systems for a variety of purposes, including separation of cells[37–40], and proteins[41–43], the generation of water-in-water emulsion droplets[44–49], in cell patterning[50,51], and more.

Microfluidic approaches have also been used separately to study phase separation in aqueous two phase systems. Silva et al[52] employed a coflowing device to map phase diagram for ATPS by monitoring for the location of the phase boundary as the fluids moved downstream. Other groups have generated droplets of initially homogenous mixtures of the phase forming compounds and then dehydrated them to induce phase separation. For example, Shim et al[53] used a complex multilayer PDMS device to trap an array of initially single phase droplets. The water content of the droplets, and thus the mixture composition, was controlled by adjusting the osmotic pressure difference between the droplets and an adjacent fluidic channel separated from the droplets by a thin semi-permeable PDMS film. Diffusion of water through the membrane mediated droplet volume and solute composition. Binodal curves were constructed and compared to bulk scale experiments for a system composed of polyethylene glycol and ammonium sulfate.

Other groups have used various types of droplet generators to study phase separation in microfluidics. Boreyko et al[54] used a 1 μm by 1 μm channel to generate a single femtolitre scale droplet composed of polyethylene glycol and

dextran and then observed phase separation due to spontaneous dehydration, or rehydrated a two phase droplet into a single phase by coalescence with a pure water droplet. Moreau et al[55] used a non-droplet based microevaporator to screen phase diagrams of polymer/polymer and polymer/salt systems by dead end filling channels with initially homogenous solutions and inducing phase separation via dehydration by flowing dry air over the semipermeable PDMS device.

Dehydration of aqueous two phase systems has been used to study phase outside of microfluidic platforms. Kojima et al[56] mapped the phase diagrams for several different aqueous two phase systems by measuring the change in volume of aqueous droplets resting at the interface between soybean oil and a perfluorocarbon fluid. The droplets were approximately 150 nL and dehydration occurred over the course of 50 – 80 hours.

The present study focuses specifically on aqueous two-phase systems composed of polymer-polymer and polymer-salt mixtures dissolved in water, but the technique can readily be extended to other phase separating complex fluid mixtures. The experiment monitors the evolution of a droplet as it dehydrates, therefore continuously traversing the concentration phase diagram. As a result, this approach results in measurements of interfacial tension at extremely high compositional resolution. Additionally, extremely high concentrations can be achieved that are not easily accessible using bulk-scale methods. Furthermore, the approach can also be useful for simultaneously constructing the phase diagram of a phase separating system, since evolution of the microstructure is also observed in the dehydration experiment.

2.2.   Materials and Methods

The aqueous two phase systems selected for the present study are two commonly used systems, one a polymer-salt mixture and the other a polymer-polymer mixture. The polymer-salt mixture is composed of polyethylene glycol (PEG) and sodium sulfate which are mixed with 18.2 MΩ-cm deionized water (EasyPure II, Barnstead) to achieve an initial bulk concentration of 10 % (w/w) PEG and 5 % (w/w) sodium sulfate. This initial mixture composition is known to be in the region of the PEG-sodium sulfate phase diagram in which the mixture is a homogeneous single-phase liquid[57]. The polymer-polymer system investigated is composed of PEG and dextran (DEX) mixed with deionized water. Several different initial bulk concentrations are considered in the present study; 3.5 % (w/w) PEG with 3.5 % (w/w) DEX, 1 % (w/w) PEG with 5 % (w/w) DEX, and 5 % (w/w) PEG with 1 % (w/w) DEX. The polyethylene glycol (*ca* 6000 g/mol) and dextran (*ca* 500,000 g/mol) are both obtained from Alfa Aesar (Ward Hill, MA) and used as received. Sodium sulfate is purchased from Fisher Scientific (Fair Lawn, NJ) and used as received. Mixtures are prepared using a vortex stirrer (Fisherbrand, Fair Lawn, NJ) for several minutes and are then left for several hours to ensure that the phase-forming components are completely dissolved prior to use.
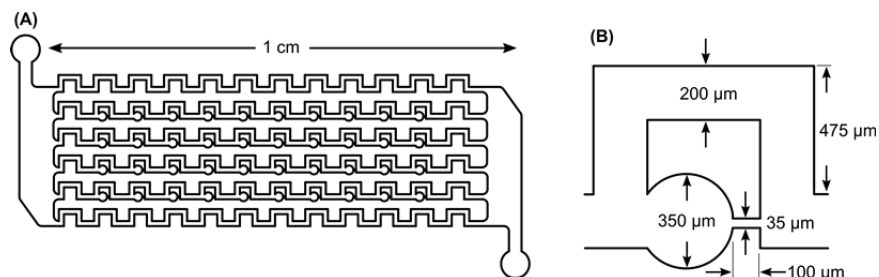
Figure 2.1. (A) Schematic diagram of the microfluidic array device used to generate and immobilize aqueous droplets. The device contains 40 droplet traps distributed among 4 parallel channels. **(B)** Close up drawing of a single droplet trap. Fluid enters from the left, is split between the bypass channel and the circular trapping region, and exits to the right. The height of the channels is 90 μm and droplets formed in this geometry have an initial volume of approximately 7 nL.

The initially homogenous aqueous two-phase systems are encapsulated in nanoliter droplets generated in the microfluidic droplet trapping device shown in Figure 2.1(A). The device is fabricated in polydimethylsiloxane (PDMS, Sylgard 184, Dow-Corning, Midland, MI) using standard soft lithography techniques[58]. The microfluidic channel pattern shown in Figure 2.1(A) is molded in PDMS and then the channels are closed by sealing the patterned PDMS with a flat piece of PDMS to ensure that all four channel walls have the same wetting properties and permeability. The device contains an array of droplets traps, shown schematically in Figure 2.1(B). After the device is filled, each trap contains a single nanoliter-scale droplet surrounded by an immiscible continuous phase liquid that fills the remainder of the device. The entire device contains a total of 40 droplet traps in the central four horizontal channels shown in Figure 2.1(A). The top and bottom channels contain no droplet traps, and serve to reduce differences in dehydration that may occur between droplets located in the center of the array and those located near the edges.

13

The droplet trapping device operates by using capillarity and hydrodynamics to generate droplets and immobilize them for long term observation[53,59–61]. The device is initially completely filled with the continuous phase fluid using a syringe pump (Braintree Scientific, Braintree, MA) at a constant flow rate of 90 μL/min. The droplet phase fluid is then introduced at a flow rate of $1 - 10$ μL/min, displacing the continuous phase liquid in the device with a large slug of droplet phase fluid, surrounded by a thin film of continuous phase liquid adhered to the channel walls. In an individual droplet trap, the droplet phase fluid enters from the left and flows simultaneously into the circular droplet trap region and into the bypass channel. When the droplet phase fluid reaches the 35 μm restriction at the opposite side of the droplet trap, it is retained due to the significant increase in pressure required to squeeze through the narrow gap. Finally, additional continuous phase fluid is pumped into the device at a flow rate of $1 - 10$ μL/min, displacing the droplet phase fluid and pinching off droplets of retained fluid as the new continuous phase fluid slug passes by each of the circular droplet trap regions. The volumetric flow rates in each step are manually adjusted during the filling procedure based on visual observations of the droplet formation process. With careful attention to the volumetric flow rates, this sequential filling procedure generates and immobilizes a monodisperse array of droplets with identical composition. The filling procedure takes approximately 10 to 30 min. In the present study, the continuous phase fluid consists of light mineral oil (Fisher Scientific, Fair Lawn, NJ) with added oil soluble surfactant Span 80 (Sigma-Aldrich, St. Louis MO) at concentrations from 0.1 to 3 % (w/w)

surfactant. The surfactant improves the wetting of the mineral oil to the PDMS device, which prevents the droplets from contacting the PDMS. Notably, this device geometry and filling method does not require complicated fluid handling or fabrication techniques, and can be accomplished by manually pumping the fluids if desired.

Once the array of droplets has been generated, the entire device is placed on the stage of an inverted microscope (TI-U, Nikon) to visualize the droplet dehydration process in bright field mode. The device is supported on the microscope stage by the right and left sides such that the top and bottom surfaces of the array are exposed to laboratory atmosphere (approximately 22 °C and 40-60 % relative humidity). The entire PDMS device is approximately 2 − 3 mm thick, with the fluidic channels located in the center. For purposes of this study, we image a subset of 1 to 4 neighboring droplets located in the center of the array. Imaging a larger number of droplets would be beneficial for monitoring highly stochastic processes, such as crystallization[53,62], but imaging a larger area would require a lower magnification, increasing the uncertainty in calculations of the composition of the droplets. A black and white CMOS camera (Guppy Pro, Allied Vision) is used to capture a digital still image every 250 seconds for a total of 12 to 24 hours.

The time sequence of images captured in each experiment is analyzed using an image segmentation algorithm, written in MATLAB, to crop, threshold (Sobel method), and detect the edges of the droplet. Prior to phase separation, the droplets are circular, and the output of the algorithm is the two-dimensional

projected circumference of the droplet at each time point. The projected circular diameter D is determined from the circumference, and the total volume of the droplet is calculated based on the projected diameter and the height of the microchannel. The height of the microchannel is approximately H = 90 μm, as confirmed by optical measurements taken of cross sections of the devices viewed in a microscope operating in bright field mode. Since the height of the channel is much smaller than the 350 μm diameter of the circular trap, the trapped droplet is confined in the z-direction and attains a pancake-like shape. Assuming that the edges of the droplet have curvature approximately equal to half of the channel height, then the volume of a pancaked-shaped droplet with circular projection may be calculated by the expression[63],

$$V_{pancake} = \frac{\pi H^3}{6} + \frac{\pi H}{4}(D-H)\left(\frac{\pi H}{2} + D - H\right).$$ (2.1)

For a non-circular droplet, the same image analysis algorithm is applied to threshold and detect the edges of the droplet, however rather than using Equation (2.1), the volume is estimated by integrating around the edges of the 2-D projection of the droplet[64], assuming that the curvature of the droplet in the z-direction is approximately equal to one half of the channel height. With knowledge of the instantaneous droplet volume and the starting concentration of solute contained within the droplet, the instantaneous concentration of solute can be estimated at any later time. The contact angles associated with the aqueous compound droplets that form at long times are measured manually from the

captured time sequence of images using the 'angle tool' in the ImageJ software (NIH).

In a typical macroscale experiment the two aqueous phases separate by gravity due to slight differences in the densities of the two phases. In microscale fluid statics, the effects of the force of gravity are often negligible compared to the forces arising from interfacial effects. The relative importance of those effects can be determined by calculating the dimensionless Bond number, $Bo = \Delta\rho g l^2 / \gamma$. Where $\Delta\rho$ is the density difference between the two fluid phases, l is the length scale, γ is the interfacial tension between the fluid phases, and g is the acceleration due to gravity. In the nanoliter droplet investigated in the work, the Bond number characteristic of the two aqueous phases is small, decreasing from approximately $Bo = 0.8$ immediately after phase separation for the polymer-salt system (Fig. 3(A), $t = 196$ min) to a minimum of approximately $Bo = 0.004$ as a result of the dramatic increase in interfacial tension between the two aqueous compartments of the droplet[4], and the decrease in the droplet size. As a result, throughout the text, we neglect the influence of gravity on the evolution of the droplet morphology.

The error bars associated with the data presented in this manuscript are obtained from error propagation analysis[65]. For the reported values of volume and concentration, the primary source of error arises from the uncertainty in determining the location of the edges of the droplet. This uncertainty results from a combination effects, including the contrast of the image, the quality and

17

uniformity of the lighting, the magnification provided by the microscope, the quantization of the image due to digital image capture, and the threshold value chosen during image analysis. As the final step in image processing, the thresholding process encompasses the majority of this uncertainty and we use the uncertainty in the volume that arises from choosing different threshold values to define the uncertainty in the calculations for droplet volume and concentration. For contact angle and interfacial tension values, the primary source of error is the uncertainty in the contact angle measurements made manually using the ImageJ software. In the present analysis, this uncertainty is ± 5 degrees based on the range of values recorded when the same contact angle was measured multiple times by hand.

2.3.   Results and Discussion

2.3.1.   Dehydration and Phase Separation

Dehydration of aqueous droplets trapped in a microfluidic device like that shown in Figure 2.1 occurs naturally at long timescales if water is sparingly soluble in the continuous oil phase and if the device is fabricated in a permeable material like cross-linked PDMS[53,54,66]. Mass transport of water out of the droplet is driven by a concentration gradient established between the droplet and the atmosphere external to the microfluidic device. Driven by the concentration gradient, water partitions into the continuous phase fluid and diffuses away from the droplet, through the permeable device material, and into the atmosphere. The loss of water results in a reduction in the droplet volume and a concomitant increase in the concentration of any dissolved solute that may be present.

Nanoliter droplets trapped in light mineral oil in a cross-linked PDMS microfluidic array and exposed to air will fully dehydrate in tens of hours. The rate of mass transport can be controlled, among other ways, by tuning the magnitude of the water concentration gradient, for example by increasing the humidity of the air to reduce the gradient, or by submerging the device in a solution isotonic to the droplet phase fluid to eliminate the gradient and arrest mass transport.
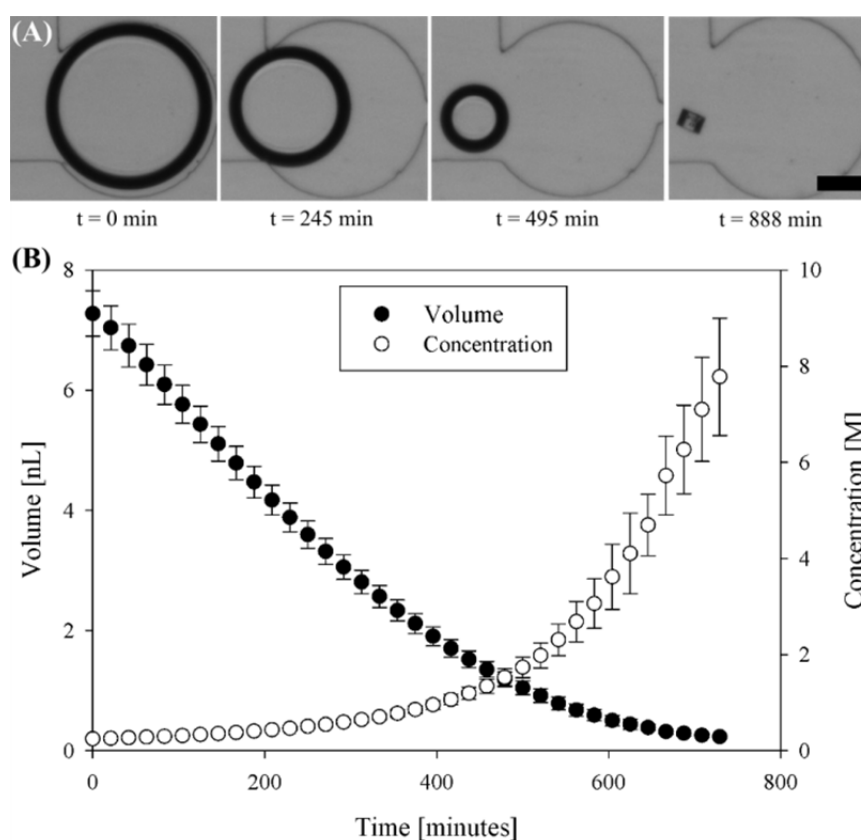
Figure 2.2. (A) Time sequence of images of a dehydrating aqueous droplet initially containing 250 mM sodium chloride. The diameter of the droplet shrinks as water is removed. At a very long time, after most of the water has been removed ($t = 888$ min), a single crystal of sodium chloride is observed in place of the droplet. The scale bar is 100 μm. **(B)** Measured volume and corresponding salt concentration of a single droplet as it dehydrates over the course of several hours prior to formation of a salt crystal. The continuous phase fluid is light mineral oil with 3 % (w/w) Span80 surfactant dissolved. The initial droplet volume is 7.28 ± 0.38 nL.

An example of a trapped aqueous droplet dehydrating in a microfluidic array is shown in Figure 2.2. In this case, the droplet initially contains 250 mM sodium chloride dissolved in deionized water, and the continuous phase fluid is light mineral oil containing 3 % (w/w) Span80 surfactant. The time sequence of images in Figure 2.2(A) demonstrates that the droplet decreases in volume as it dehydrates in this microfluidic platform. Just after formation, the projected diameter of the droplet is approximately 340 μm and its volume is 7.28 ± 0.38 nL, calculated following the procedure described in the previous section. The size of the circular droplet trap region (350 μm) determines the initial droplet volume. At an elapsed time $t = 746$ min (not shown in the figure), corresponding to a concentration of approximately 9 M NaCl, a faceted object presumed to be a crystal of sodium chloride is observed inside the droplet. By $t = 888$ min (Fig. 2.2A, top right panel) the droplet is reduced to a hydrated crystal of sodium chloride. Given the initial concentration of sodium chloride (250 mM), the initial droplet volume (7.28 nL), and the density of crystalline sodium chloride (2.17 g/ml) , we may estimate the volume that a fully dehydrated crystal would occupy as approximately 49000 μm^3. The size of the crystal visible in Figure 2.2 at $t =$ 888 min is approximately 47 x 47 μm, which would require a physically reasonable height of 22 μm in order to obtain the predicted crystal volume. The exact height cannot be determined from the 2-D projected images obtained in the experiment. The measured volume of the droplet and the corresponding salt concentration within the droplet are plotted as functions of time in Figure 2.2(B). From the time the droplet is formed until the appearance of the sodium crystal, the

concentration of salt increases by a factor of 31, with a proportional decrease in the volume. Thus, the concentration of solute in an aqueous droplet can be increased by more than an order of magnitude through passive dehydration in a PDMS microfluidic trap.
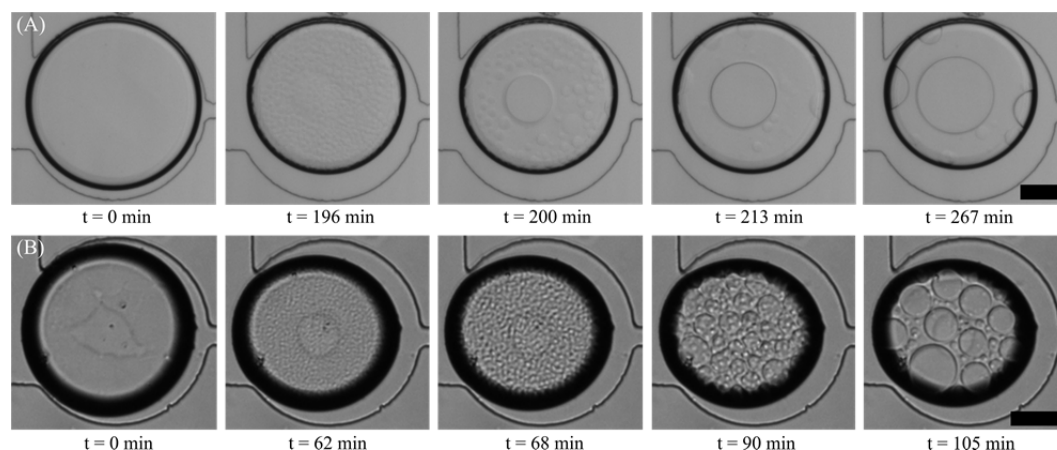
Figure 2.3. Time sequences of images of dehydrating droplets containing two different aqueous two-phase systems. **(A)** The droplet initially contains 10 % (w/w) polyethylene glycol (6,000 g/mol) and 5 % (w/w) sodium sulfate dissolved in deionized water. At $t = 0$ min the droplet contains a single phase, homogeneous liquid. At $t = 196$ min phase separation is first observed visually. By $t = 267$ min the inner phase has coalesced into a few large drops suspended within the parent droplet. **(B)** The droplet initially contains 3.5 % (w/w) polyethylene glycol (6,000 g/mol) and 3.5 % dextran (500,000 g/mol) and undergoes a similar process of phase separation and coalescence as shown in (A). At approximately $t = 62$ min phase separation is observed in the droplet, and as time elapses up to $t = 105$ min the inner polymer-rich phase coalesces into larger droplets. In both experiments, the continuous phase fluid is light mineral oil with 3 % (w/w) Span80 surfactant dissolved. The scale bar in both image sets is 100 μm.

When a mixture of two slightly incompatible polymers, or a polymer and salt, are dissolved in the aqueous droplet, the dehydration of the droplet and corresponding concentration increase can lead to phase separation. Two examples of such mixtures concentrating within trapped droplets are shown in Figures 2.3 (A) and (B). In the images, time $t = 0$ min denotes the time at which the first image is taken, which is approximately 5 to 10 min after the device is loaded with droplets. Since mixing in microfluidic devices is challenging[67], particularly in a

static array, the initial concentration of phase forming components is carefully chosen such that the solutions begin as a homogeneous single phase liquid[1,57]. This allows us to ensure good mixing by bench-top methods prior to loading the microfluidic device. Upon formation of the droplets, dehydration occurs slowly, and phase separation occurs relatively rapidly once the concentration exceeds a critical value. In the image sequence shown in Figure 2.3(A), the droplet initially contains 10% (w/w) PEG and 5 % (w/w) sodium sulfate. At $t = 0$ the droplet contains a single phase, homogenous mixture of polymer, salt, and water with a total volume of 12.78 ± 0.40 nL. At $t = 196$ min, the inside of the droplet appears non-uniform, indicating the start of decomposition of the solution into two phases. As the droplet continues to dehydrate, one of the aqueous phases coalesces to form a few large droplets encapsulated within the parent drop ($t = 267$ min). In the image sequence shown in Figure 2.3(B), the droplet initially contains 3.5 % (w/w) PEG and 3.5 % (w/w) DEX. At $t = 0$ min the droplet volume is 7.12 ± 0.37 nL. As the droplet dehydrates, a similar sequence of phase separation and coalescence of the internal droplet compartments is observed. At $t = 62$ min, the inside of the droplet first appears non-uniform, and after $t = 105$ min, one of the aqueous phases has coalesced into several large droplets encapsulated within the parent drop.
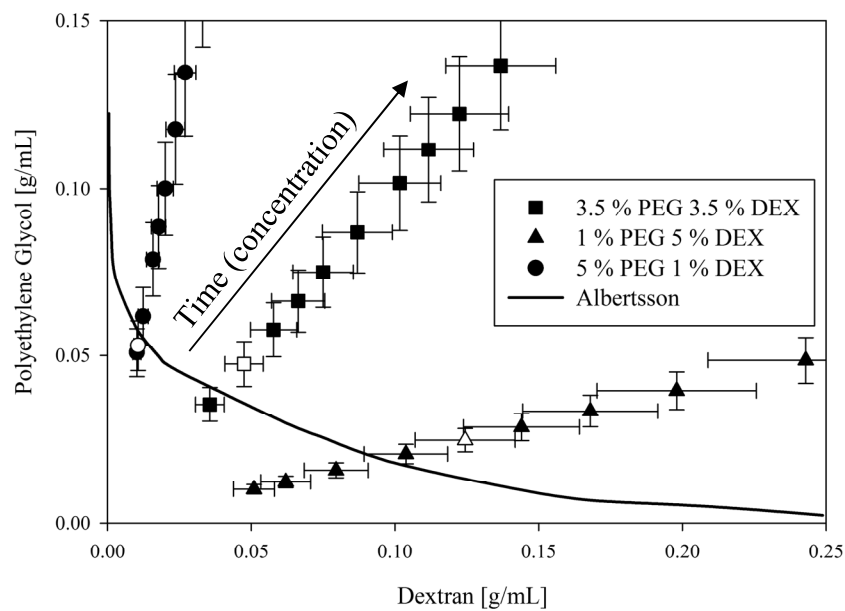
Figure 2.4. Phase diagram for aqueous mixtures of polyethylene glycol (6,000 g/mol) and dextran (500,000 g/mol). The solid line corresponds to the binodal curve for this system reported by Albertsson[1]. The three sets of closed symbols correspond to three separate droplet dehydration experiments with different relative concentrations of polyethylene glycol and dextran. Open symbols indicate the concentration at which phase separation is first observed visually. The legend indicates the starting weight fractions of polymer in each experiment. Each series of symbols is obtained by observing a single droplet evolve in time, and then using the measured volume to estimate the corresponding instantaneous polymer concentrations assuming no loss of polymer from the interior of the droplet.

The visual observations indicating phase separation within the droplets can be compared with the known phase diagram of the aqueous two-phase system. Figure 2.4 is a plot of the phase diagram for the PEG-DEX aqueous two-phase system investigated in this study. The vertical axis is the concentration of polyethylene glycol; the horizontal axis is the concentration of dextran. The solid line corresponds to the binodal curve for this system as reported by Albertsson[1]. The three sets of closed symbols correspond to three separate microfluidic experiments where the relative concentration of polyethylene glycol and dextran is varied by changing the composition of the solutions that are loaded into the

23

device. In each experiment the droplet begins at a polymer composition located in the single-phase region of the phase diagram. As the experiment proceeds, the droplet dehydrates and the overall polymer concentration increases, while the relative concentrations of the two polymers remains fixed, since we assume that only water is leaving the droplet. Each set of symbols corresponds to a single droplet dehydrating with a fixed ratio of polymer concentrations. Time increases for each data set from lower left to upper right on the plot. The square symbols correspond to a droplet with a starting composition of 3.5 % (w/w) PEG and 3.5 % (w/w) DEX. The circle symbols correspond to a droplet with an initial composition of 5 % (w/w) PEG and 1 % (w/w) DEX. The triangle symbols correspond to an initial composition of 1 % (w/w) PEG and 5 % (w/w) DEX. The open symbol in each data set indicates the composition at which phase separation is first observed visually in the droplet.

The observed onset of phase separation agrees reasonably well with the binodal curve reported previously[1]. The polymer ratio of 5:1 PEG:DEX exhibits nearly the same critical composition for the onset of phase separation as previously reported, while the other two polymer ratios exhibit slightly larger critical PEG concentrations for the same DEX concentration. Some deviation from the reported binodal curve is expected as a result of lot-to-lot variations in polymer molecular weight and polydispersity[1]. Additionally, optical resolution and image contrast limit the ability to observe the very early stages of phase separation. Given these factors, the relatively good agreement with the reported binodal curve for this PEG-DEX aqueous two-phase system suggests that the

phenomenon observed in Figure 2.3 is indeed a result of concentration-induced phase separation and that visual observations of phase separation and the estimates of droplet composition are sufficiently accurate to estimate the concentration at which phase separation occurs. This approach is readily applied to other aqueous two-phase systems for which the phase diagram is not known and can be used to rapidly construct the stability curve. This is particularly valuable when screening how additives to the two phase system affect phase separation.

2.3.2. Dewetting and Droplet Morphology
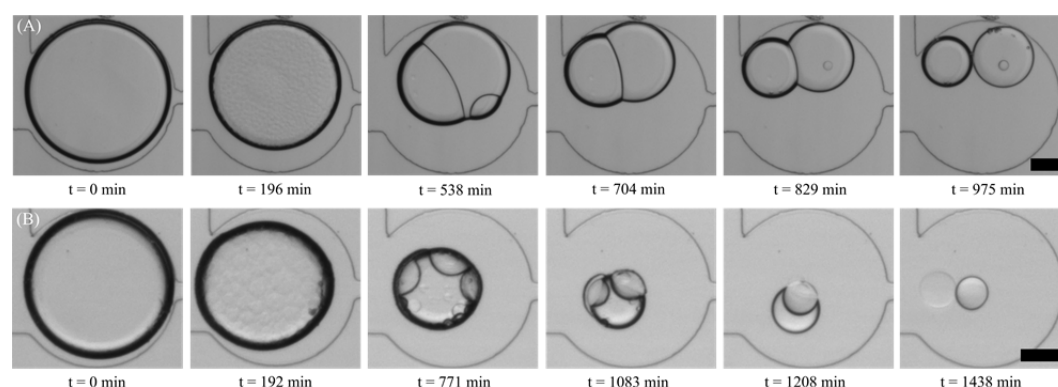
Figure 2.5. Time sequences of images of two different droplets containing the same aqueous two-phase systems as shown in Fig. 2.3, but after dehydrating over a much longer period of time. **(A)** A droplet with an initial composition of 10 % (w/w) polyethylene glycol (6,000 g/mol) and 5 % (w/w) sodium sulfate. After phase separation (t = 196 min) the contact line shared by the two phases is reduced (t = 829 min) and finally eliminated (t = 975 min), resulting in two physically separate droplets completely wet by the continuous oil phase. **(B)** A droplet with an initial composition of 3.5 % (w/w) polyethylene glycol (6,000 g/mol) and 3.5 % (w/w) dextran (500,000 g/mol). After phase separation (t = 196 min) the PEG-rich and DEX-rich phases coalesce, eventually forming two partially wetting polymer-rich compartments (t = 1208 min). Eventually the phases physically separate into two distinct droplets (t = 1438 min). In both (A) and (B) the continuous fluid phase fluid is light mineral oil with 3 % (w/w) Span80 surfactant dissolved. The scale bars in both image sets are 100 μm.

Figures 2.3 and 2.4 capture the early stages of phase separation. As dehydration continues beyond the onset of phase separation and initial

coalescence of the two phases, dramatic changes in droplet morphology are observed. Figure 2.5 contains two image sequences from a separate set of experiments using the same two phase systems as shown in Figure 2.3, but with images that capture a much longer period of observation of the dehydration process. Figure 2.5(A) shows a droplet with an initial composition of 10 % (w/w) PEG and 5 % (w/w) sodium sulfate. The onset of phase separation is observed at an elapsed time of $t = 196$ min. After 538 min the second phase has nearly fully coalesced, and the droplet attains a configuration in which the two aqueous phases form distinct compartments where each compartment shares an interface both with the other aqueous compartment as well as the oil continuous phase. Between 538 min and 975 min the interface shared by the two aqueous phases is reduced and finally eliminated, resulting in two physically separate droplets that are each fully wet by the continuous oil phase fluid. Figure 2.5 (B) shows a droplet with an initial composition of 3.5 % (w/w) PEG and 3.5 % (w/w) DEX. Similar to the process depicted in Figure 2.5(A), the onset of phase separation is observed at an elapsed time prior to $t = 192$ min. Between 771 min and 1438 min the two aqueous phases coalesce to form distinct compartments within the aqueous compound droplet. By 1438 min, the interface shared between the two aqueous polymer phases has been reduced and eventually eliminated, resulting in two concentrated, polymer-rich drops each fully wet by the continuous oil phase.

Figure 2.5 demonstrates that dramatic changes in droplet morphology occur when a large fraction of the water is removed from an aqueous droplet containing polymer-polymer or polymer-salt mixtures that tend to phase separate.

26

These configurational changes occur when the droplet is suspended in a third immiscible continuous phase fluid, in this case light mineral oil with span 80 surfactant dissolved. Comparing the two systems examined in this study, the polymer-salt system experiences complete dewetting earlier in the dehydration process than the polymer-polymer system. The total concentration of polymer in the PEG-DEX droplet exhibiting the partially wetting configuration at $t = 1083$ min is approximately 0.53 g/ml, while the total concentration of phase forming components in the PEG-sodium sulfate droplet at the partially engulfed state ($t = 583$ min) is only approximately 0.35 g/mL. Likewise, at the point of complete dewetting, the PEG-sodium sulfate droplet has a total concentration of approximately 0.62 g/mL, while the PEG-DEX system has a total polymer concentration of approximately 0.99 g/mL. At this concentration, the PEG-rich and DEX-rich compartments are almost fully dehydrated.
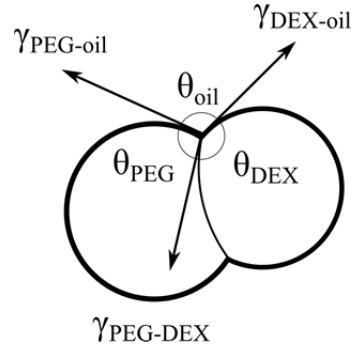
Figure 2.6. Schematic diagram of a compound drop, such as is observed in Figure 2.5, providing definitions for the notation used in the rest of the text. In the case of the polymer-salt system, the DEX notation is substituted with Na_2SO_4.

The structural changes in the compound droplets observed in Figure 2.5 are typical of configurations seen between three immiscible fluid phases when the interfacial tensions are related to one another in a specific way. In the absence of

other external forces we presume that the changes in droplet morphology observed in Figure 2.5 arise from changes in the relative values of the interfacial tensions as the droplet dehydrates and concentrates. Torza and Mason[68] provide a set of criteria relating the interfacial tension between two liquid droplets suspended in a third phase to the physical morphology of the compound droplet formed when they contact. The criteria for the transitions between fully engulfed (Figure 2.5B t = 193 min), partially engulfed (Figure 2.5B t = 1208 min, and non-engulfed (Figure 2.5B t = 1438 min) compound droplets are presented in in terms of spreading coefficients, which are derived from minimization of the change in Gibbs surface free energy. Following the notation provided in Figure 2.6, spreading coefficients may be defined for any 3-phase liquid system, given generically by

$$S_i = \gamma_{jk} - \gamma_{ij} - \gamma_{ik} .$$
(2.2)

Where S is the spreading coefficient, γ is the interfacial tension, and the subscripts i, j, and k denote the three immiscible phases. For example, in the case of the PEG and DEX two phase system (Figure 2.6) i, j, and k refer to the PEG-rich, DEX-rich, and continuous oil phases. If we assume that one of the aqueous phases always has a lower interfacial tension against the continuous oil phase than the other, $i.e.$ $\gamma_{DEX-oil} > \gamma_{PEG-oil}$, then three potential wetting configurations are possible, each defined by three spreading coefficients[68]. This validity of this assumption is confirmed by the fact that we always observe, initially, that the DEX-rich phase is fully wet by the PEG-rich phase. This is consistent with the

fact that the DEX-rich phase is slightly more hydrophilic than the PEG-rich phase[1,69,70], and is observed experimentally for similar microfluidic systems using PEG DEX or PEG-salt droplets a continuous oil phase[71]. To attain the fully engulfed configuration, where the PEG-rich solution completely engulfs the DEX-rich solution, the first two spreading coefficients must be negative while the third is positive, $S_1 < 0$, $S_2 < 0$, and $S_3 > 0$. To attain the partially engulfing configuration, all three spreading coefficients must be negative, $S_1 < 0$, $S_2 < 0$, and $S_3 < 0$. Finally, to attain the non-engulfing state, the first and third spreading coefficients must be negative while the second is positive, $S_1 < 0$, $S_2 > 0$, and $S_3 < 0$. Therefore, in order to transition from a fully engulfed configuration to a partially engulfing configuration, the third spreading coefficient S_3 must change sign from positive to negative, which requires the DEX-oil interfacial tension to change from greater than the sum of the other two interfacial tensions to less than this sum,

$$\gamma_{\text{DEX-oil}} > \gamma_{\text{PEG-DEX}} + \gamma_{\text{PEG-oil}} \tag{2.3}$$

to

$$\gamma_{\text{DEX-oil}} < \gamma_{\text{PEG-DEX}} + \gamma_{\text{PEG-oil}}. \tag{2.4}$$

This requirement implies that either $\gamma_{\text{DEX-oil}}$ must decrease significantly, or one or both of the two remaining interfacial tensions, $\gamma_{\text{PEG-DEX}}$ or $\gamma_{\text{PEG-oil}}$, must increase significantly. It is well known[3,4] that $\gamma_{\text{PEG-DEX}}$ increases by several orders of magnitude as the total polymer concentration increases. Previous studies report a

value of approximately $\gamma_{\text{PEG-DEX}} = 0.8$ mN/m at a total polymer concentration of approximately 0.4 g/mL[4]. If $\gamma_{\text{PEG-oil}}$ is similar in magnitude to $\gamma_{\text{DEX-oil}}$, then the increase in $\gamma_{\text{PEG-DEX}}$ may be sufficient to satisfy the criterion given in Equation 8, leading to the partially engulfing configuration we observe in our experiments (Figure 2.5B $t = 771$ to 1208 min).

For a transition from the partially engulfing to non-engulfing configuration, which is observed for both two phase systems at very long dehydration times, the second spreading coefficient, S_2, must change sign from negative to positive, implying that the interfacial tension between the aqueous polymer phases must increase from less than the sum of the two aqueous-oil interfacial tensions to greater than this sum,

$$\gamma_{\text{PEG-DEX}} < \gamma_{\text{DEX-oil}} + \gamma_{\text{PEG-oil}} \qquad (2.5)$$

to

$$\gamma_{\text{PEG-DEX}} > \gamma_{\text{DEX-oil}} + \gamma_{\text{PEG-oil}}. \qquad (2.6)$$

This implied change requires that the value of $\gamma_{\text{PEG-DEX}}$ increase significantly during dehydration of a droplet, while $\gamma_{\text{DEX-oil}}$ and $\gamma_{\text{PEG-oil}}$ decrease in magnitude, remain the same, or at least increase more slowly as a function of total polymer concentration. The expected increase in $\gamma_{\text{PEG-DEX}}$ over serval orders of magnitude as the two polymer-rich phases become more concentrated is consistent with this criterion. An analogous argument can be made for the system composed of PEG and sodium sulfate.

In this analysis it is important to note that we assume that the time scale for the change in droplet concentration (several hours) due to dehydration is much longer than the characteristic time scales for the reorientation of the contact line due to concentration dependent changes in interfacial tension. Additionally, we assume that the equilibrium morphology of the droplets is not affected by their confinement in the microchannel, but rather is exclusively determined by the surface energies. This assumption may not be valid for droplets being advected downstream due to the motion of a continuous phase fluid[72–74], however in a quiescent fluid, such as in our experiments, the wetting configuration will be exclusively determined by the interfacial tensions between each of the three phases[68,75,76].

0.1 % w/w	0.5 % w/w	1 % w/w	3 % w/w
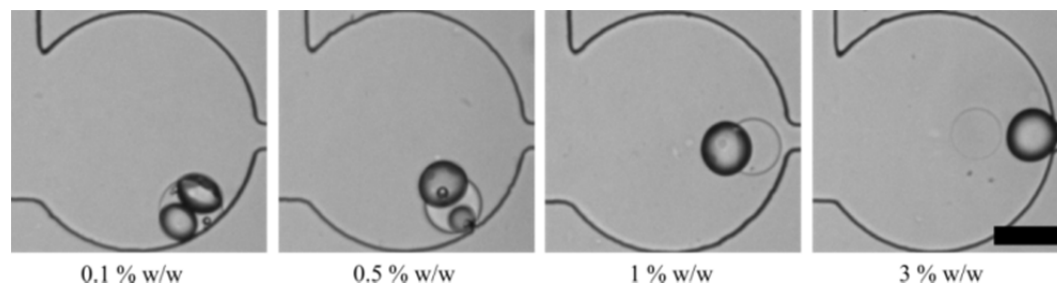
Figure 2.7. Representative images from four different dehydration experiments in which only the concentration of surfactant dissolved in the outer phase fluid varies. The weight fractions listed below each image indicate the weight fraction of Span80 surfactant added to the light mineral oil continuous phase fluid. The images were taken at the same elapsed time, once the compound droplets had achieved their final state. Each droplet initially contains 3.5 % (w/w) polyethylene glycol (6,000 g/mol) and 3.5 % (w/w) dextran (500,000 g/mol) dissolved in deionized water. The scale bar is 100 μm.

The relative magnitudes of the interfacial tensions, and therefore the spreading coefficients and wetting configurations, can also be tuned by varying the interfacial tension of the aqueous-oil interface. Figure 2.7 shows representative images from four different experiments in which droplets are dehydrated for approximately 1080 min (18 hr). All four droplets initially contain 3.5 % (w/w) PEG and 3.5 % (w/w) DEX. The mass fraction of Span80 surfactant dissolved in the light mineral oil continuous phase fluid is the only parameter varied between the four experiments, from 0.1 to 3 % (w/w). The images shown in Figure 2.7 show that the droplets immersed in the three lower surfactant concentration mixtures, 0.1 %, 0.5 %, and 1 % (w/w), attain a partially engulfed morphology in which both of the polymer-rich phases are partially wet by one another as well as the continuous phase fluid. As the concentration of Span80 surfactant increases, the two aqueous compartments are increasingly wet by the continuous phase oil, with a corresponding reduction in the interfacial area shared between them. In the presence of 3 % (w/w) Span80, the two aqueous compartments are observed to completely dewet from one another, resulting in

32

two physically separate polymer-rich droplets fully wet by the oil continuous phase. The observation that the concentration of surfactant dissolved in the continuous phase fluid influences the final wetting configuration of the aqueous compound droplet supports our assumption that changes in droplet morphology are a result of changes in the relative interfacial tensions as the droplet contents become more concentrated. The inability of the PEG-DEX droplet to obtain a non-engulfing configuration in the presence of less surfactant dissolved in the continuous oil phase can be explained in terms of our spreading coefficient argument presented earlier. The transition from partially engulfing to non-engulfing requires that the second spreading coefficient change sign from negative to positive, which requires that the value of $\gamma_{\text{PEG-DEX}}$ exceed the sum of $\gamma_{\text{DEX-oil}}$ and $\gamma_{\text{PEG-oil}}$ as given in Equations (2.5) and (2.6). If these two interfacial tension values have not been sufficiently reduced by the presence of a surfactant, the sum of $\gamma_{\text{DEX-oil}}$ and $\gamma_{\text{PEG-oil}}$ remains large compared to $\gamma_{\text{PEG-DEX}}$, despite any increases associated with the increase in total polymer concentration.

2.3.3. Contact Angles and Interfacial Tension
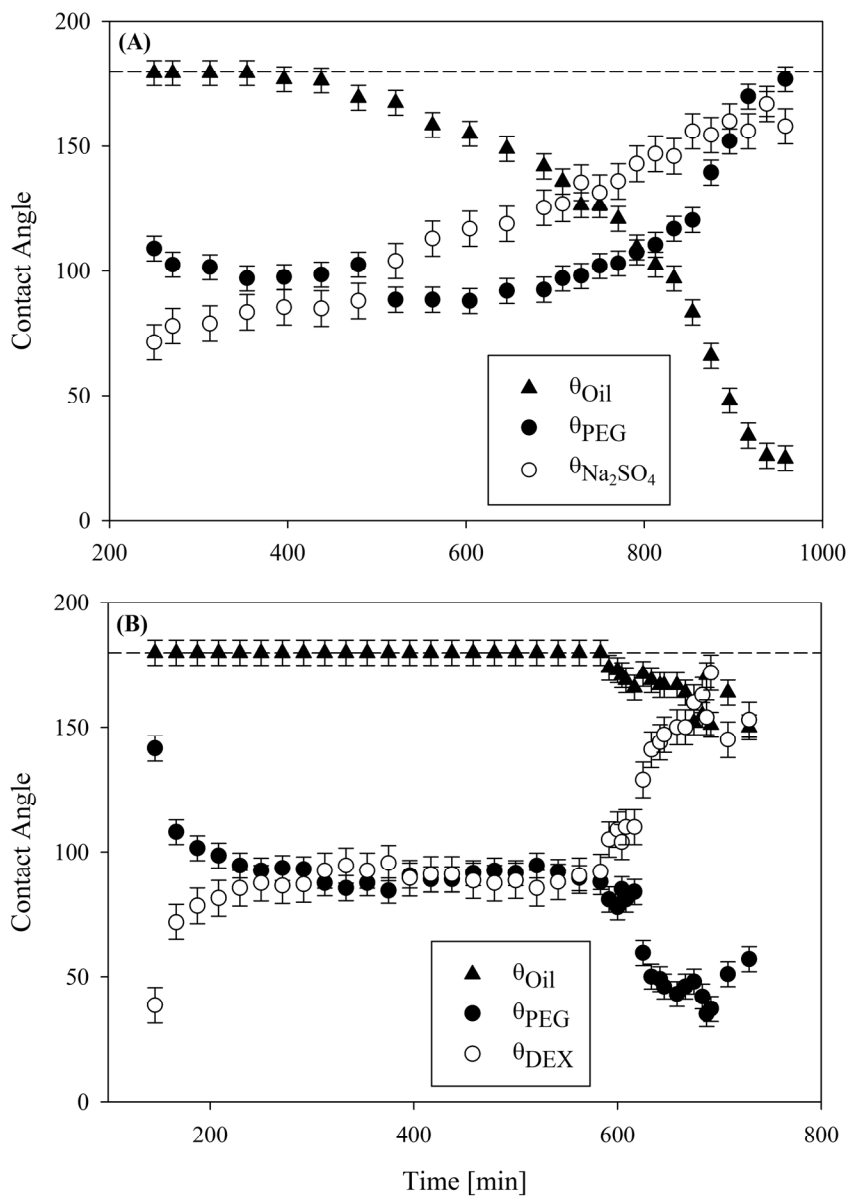
Figure 2.8. Contact angles associated with the three-phase contact line as a function of dehydration time for compound drops of phase separated aqueous two phase mixtures of **(A)** polyethylene glycol (6,000 g/mol) – sodium sulfate and **(B)** polyethylene glycol (6,000 g/mol) – dextran (500,000 g/mol). The continuous phase fluid is light mineral oil containing 3 % (w/w) dissolved Span80 surfactant. Refer to Figure 2.6 for a graphical description on the contact angles.

Although an analysis of spreading coefficients provides insight into relative magnitudes of interfacial tension required for each wetting transition, we

34

may gain additional understanding of the dewetting process by measuring the contact angles of the aqueous compound droplet as a function of the corresponding polymer and salt concentrations as they evolve in time. Figure 2.8 plots the time evolution of the contact angles associated with the three-phase contact line at the interface between the partially wetting aqueous phases of the compound droplet and the surrounding oil continuous phase fluid, for both aqueous two-phase systems investigated. Measurement of the contact angles begins once a three-phase contact line becomes visible, which occurs once the droplet has dehydrated past the initial onset of phase separation, but may be made before the components within the droplet have fully coalesced. In Figure 2.8(A) the droplet initially contains 10 % (w/w) PEG and 5 % (w/w) sodium sulfate. As depicted schematically in Figure 2.6, the angle θ_{Oil} refers to the contact angle within the external oil phase; i.e., between the PEG-rich/oil interface and the sodium sulfate-rich/oil interface. The angle θ_{PEG} refers to the contact angle within the PEG-rich phase; i.e. between the PEG-rich/oil phase interface and the interface between the two aqueous compartments. Both angles are measured from a sequence of micrographs similar to those shown in Figure 2.5(A). The angle $\theta_{\text{Na}_2\text{SO}_4}$ is calculated from the other two angles, applying the physical constraint that the sum of the angles at the three-phase contact line must be equal to 360°. In Figure 2.8(A), the exterior angle between the two aqueous phases, θ_{Oil}, is initially 180°. As dehydration proceeds, the contact angle decreases monotonically to a minimum of 25°, at which point it becomes difficult to measure optically as the droplet compartments completely dewet. The interior angle of the sodium sulfate-

rich phase increases from an initial value of 72° to a maximum at dewetting of 158°. The interior angle of the PEG-rich phase is initially 109°, decreases to 88°, and then increases to a maximum of 177° just before dewetting.

In Figure 2.8(B) the droplet initially contains 3.5 % (w/w) PEG and 3.5 % (w/w) DEX. In this case, the exterior angle between the two aqueous polymer phases, θ_{Oil}, remains fixed at 180° for approximately 600 min, then decreases slightly to a final value of approximately 150° just prior to dewetting. The interior angle of the polyethylene glycol-rich phase, θ_{PEG}, decreases rapidly from 142° at t = 145 min to approximately 90° after 200 min. As a result, the interior angle of the dextran-rich phase increases rapidly from an initial value of 38° to approximately 90° after 200 min. At t = 600 min, the droplet transitions from the circular morphology, as seen in Figure 2.5 (B) at t = 771 min, to a partially engulfed configuration as seen in Figure 2.5 (B) at t = 1083 min. The droplet continues to dehydrate and dewet after 730 min, although we note that the index of refraction of the polyethylene glycol-rich compartment approaches that of the continuous phase fluid, limiting the ability to optically measure the contact angles.

Figure 2.8 quantifies the morphological transitions observed in the dehydrating two-phase compound droplet. In the absence of external forces, the wetting configuration of two immiscible droplets suspended in a third immiscible continuous phase fluid can be determined exclusively by the interfacial tensions between each of the three phases[68], as we described earlier by way of spreading

coefficients. However, the spreading coefficient analysis is limited in that if we do not know all three interfacial tensions *a priori* we cannot calculate the values of the spreading coefficients. Instead, we can apply the relationships given by Neumann's Triangle[16]. In the partially-engulfing configuration, a force balance at the three-phase contact line yields a relationship between the interior contact angles of the two droplet compartments and the three interfacial tensions,

$$\gamma_{ij} \cos\theta_j + \gamma_j + \gamma_i \cos(\theta_i + \theta_j) = 0, \tag{2.7}$$

where i and j refer to each of the two aqueous phases as depicted in Figure 2.6. Following the analysis of Guzowski *et al.* this expression can be rearranged to reveal a ratio of two interfacial tensions that is a function only of the contact angles[76],

$$\frac{\gamma_i}{\gamma_{ij}} = \frac{\sin\theta_j}{\sin(\theta_i + \theta_j)}. \tag{2.8}$$

A set of ratios can be calculated for each of the two-phase systems under examination, providing information about the relative change in the interfacial tensions.
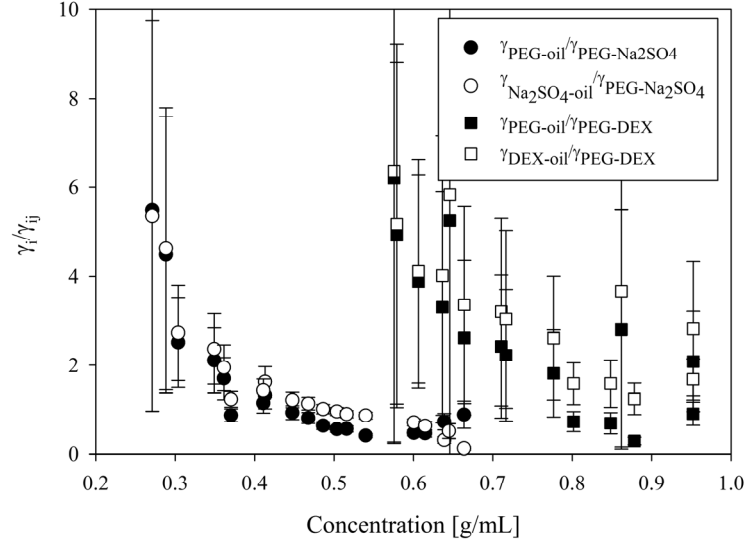
Figure 2.9. Interfacial tension between the aqueous droplet and the light mineral oil continuous phase, divided by the interfacial tension between the two phase-separated aqueous compartments for the PEG-sodium sulfate (round symbols) and the PEG-DEX (square symbols) mixtures.

Substituting the measurements shown in Figure 2.8 into Equation (2.8) and plotting the result as a function of the total concentration of phase forming components within the dehydrating droplet leads to the plot shown in Figure 2.9. Figure 2.9 is a plot of the ratios of each of the interfacial tension values between an aqueous compartment and the continuous oil phase ($\gamma_{PEG-oil}$ or $\gamma_{Na_2SO_4-oil}$), divided by the interfacial tension between the two aqueous compartments ($\gamma_{PEG-Na_2SO_4}$ or $\gamma_{PEG-DEX}$). The horizontal axis indicates the total polymer concentration for the PEG-DEX system or the total concentration of polymer and salt for the PEG-sodium sulfate system at the corresponding instant in time. Both of the aqueous two-phase systems exhibit similar behavior of the interfacial tension ratios. For each system considered, the interfacial tension ratios are similar in magnitude and decrease monotonically as the concentration of phase forming components increases. The PEG-salt system experiences these changes at

much lower total concentration values. This is expected, since polymer-salt aqueous two-phase systems are known to have characteristically higher interfacial tension than polymer-polymer aqueous two-phase systems, and therefore the ability to measure the corresponding contact angles should occur earlier in the dehydration process.

Importantly, Figure 2.9 provides insight into the relationships between the three interfacial tensions and how they evolve with concentration, without requiring knowledge of their exact magnitudes. Since the ratio of interfacial tensions between each of the aqueous compartments and the external oil phase are similar as can be seen in Figure 2.9,

$$\frac{\gamma_{\text{PEG}}}{\gamma_{\text{PEG-Na}_2\text{SO}_4}} \approx \frac{\gamma_{\text{Na}_2\text{SO}_4}}{\gamma_{\text{PEG-Na}_2\text{SO}_4}} , \qquad (9)$$

this implies that the interfacial tension of each aqueous component with oil is also similar. Thus, the interfacial tension between the two aqueous compartments can be estimated if the aqueous-oil interfacial tension is known as a function of droplet composition. Although the concentrations of polymer and salt in the aqueous droplets increases with time, we assume that the aqueous-oil interfacial tension is dominated by the large amount of Span 80 (much greater than the critical micelle concentration) dissolved in the mineral oil phase. In this case, the interfacial tension for pure water adjacent to oil with dissolved Span 80 above the critical micelle concentration (0.43 mM[77]) provides a reasonable approximation. For purposes of the present study, we use a previously reported value of the

water-oil interfacial tension at the critical micelle concentration of Span 80 of

$\gamma_{\text{water-mineral oil}} = 3.0 \text{ mN/m}^{77}$.

Figure 2.10 is a plot of the apparent interfacial tension between the aqueous components of the compound droplets estimated by dividing the aqueous-oil interfacial tension by the average of the two individual interfacial tension ratios presented in Figure 2.9 at each instant in time,

$$\gamma_{\text{PEG-Na}_2\text{SO}_4} = \frac{\gamma_{\text{water-mineral oil}}}{\frac{1}{2}\left(\frac{\gamma_{\text{PEG}}}{\gamma_{\text{PEG-Na}_2\text{SO}_4}} + \frac{\gamma_{\text{Na}_2\text{SO}_4}}{\gamma_{\text{PEG-Na}_2\text{SO}_4}}\right)}. \tag{2.10}$$

The horizontal axis is the corresponding total concentration of phase forming components in the droplet. This analysis assumes that the aqueous-oil interfacial tension does not change significantly during an experiment. Deviations from this assumption may occur at the extremely large polymer and salt concentrations accessible in the dehydration experiment.
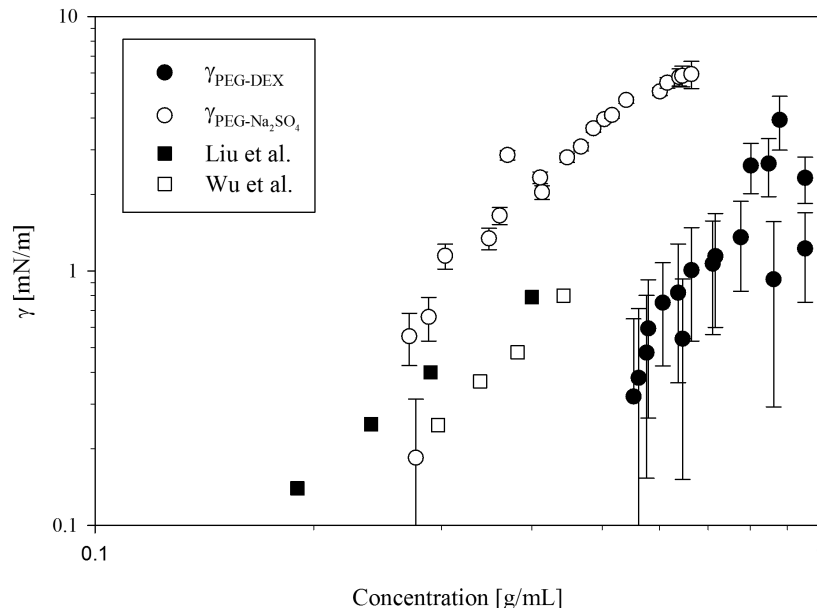
Figure 2.10. Effective interfacial tension between the phase-separated aqueous compartments of a compound droplet as a function of the total concentration of the phase forming components. Circle symbols correspond to the values estimated in the present work; square symbols correspond to previously published interfacial tension values for PEG-DEX (Liu et al.) and PEG-sodium sulfate (Wu et al.) two phase systems[4,78]

In Figure 2.10, the interfacial tension between the polyethylene glycol-rich and sodium sulfate-rich phases (open circles) increases by more than one order of magnitude, from approximately 0.18 mN/m to 5.39 mN/m as the concentration approximately doubles. Similarly, the interfacial tension between the polymer-rich phases of the polyethylene glycol/dextran two-phase system (filled circles) increases by slightly less than one order of magnitude, from 0.32 mN/m to approximately 2.32 mN/m as the concentration of phase forming components approximately doubles. The open and filled squares correspond to interfacial tension values reported previously using the spinning drop technique for similar, but not identical, aqueous two-phase systems. The open square symbols correspond to tabulated data reported by Wu *et al.*[78] for a system composed of ca

41

4000 g/mol molecular weight PEG and sodium sulfate, whereas the present study examines *ca* 6000 g/mol molecular weight PEG. The open circles correspond to data reported by Liu *et al.*[4] for *ca* 8000 g/mol molecular weight PEG and the same molecular weight dextran used in the present study. In both previous reports, the total concentrations of phase forming components investigated are significantly lower than those accessed in the present study, due to the ability of the microfluidic platform to easily generate highly concentrated systems from initially well mixed, semi dilute and low viscosity, homogeneous solutions. For example, Liu et al. report interfacial tension up to a total polymer concentration of 0.4 g/ml, while our experiments access polymer concentrations a factor of two greater, without any increase in the difficulty of mixing or executing the experiment. Literature reports providing interfacial tension data are extremely limited for aqueous two-phase systems in general, and data is not available for the exact polymer molecular weights considered in the present study. The interfacial tension of the aqueous components is expected to be a function of polymer molecular weight[78] and specifically has been found to vary strongly with the molecular weight of PEG[5], so the data sets shown in Figure 2.10 cannot be directly compared. Nevertheless, the previous reports indicate the expected range of magnitudes of interfacial tension values, and our analysis demonstrates the ability to measure interfacial tension values in this range over a much wider range of concentrations than has previously been feasible.

Our analysis, which relies on the application of Neumann's triangle, assumes the two polymer-rich phases are always liquids. In the event one liquid is

replaced by a solid surface, Young's equation[16] becomes appropriate. As can be seen in Figures 2.8, 2.9, and 2.10, contact angles and interfacial tension are reported at total polymer concentrations in the droplet up to 0.95 g/mL. At high polymer concentrations we expect deviations in the interfacial tension values as the liquid phases become more viscous and eventually solidify. In experiments, we observe that at very long times, several hours after complete dewetting, that the polyethylene glycol-rich phase is birefringent, indicating that it has become partially crystalline. This occurs long after the aqueous phases have completely dewet from one another, so no contact angle or interfacial tension data is reported at these conditions, however this suggests that at some point during experiments the droplet compartments become solid-like.

2.4.   Conclusions

Aqueous nanoliter droplets containing initially well mixed, dilute polymer solutions can be generated, held fixed, and dehydrated at a controlled rate in a microfluidic trap, driving the polymer concentration within the droplets to extremely high values that are not readily accessible at the macroscopic scale. In this process, slightly incompatible polymer mixtures undergo phase separation at semi-dilute concentrations that agree with those reported for macroscale systems. Upon phase separation, the two polymer-rich phases coalesce to form adjacent aqueous compartments inside of the compound droplet. A three-phase contact line is established between the immiscible continuous phase fluid and the two aqueous compartments, with contact angles determined by the interfacial tensions of the three phases. When the continuous phase fluid has an appropriately low interfacial tension, the aqueous compound droplet will undergo a series of wetting transitions from fully- to partially- to non-engulfing as the concentration of phase forming components increases. In the mineral-oil/aqueous systems considered here, the wetting transitions only occur in the presence of excess surfactant dissolved in the continuous phase fluid. Measurements of the contact angles associated with the three-phase contact line allow the ratios of interfacial tensions between the phases to be calculated as a function of concentration. Provided one of the three interfacial tensions is known, the other two can be determined. Using estimates of the oil-aqueous interfacial tension, we have estimated the internal interfacial tension for two common aqueous two-phase polymer systems. For mixtures of sodium sulfate and polyethylene glycol, the interfacial tension is estimated to

increase by more than an order of magnitude from 0.18 mN/m up to 5.34 mN/m over a narrow range of total polymer/salt concentration from 0.28 g/mL to 0.66 g/mL. For mixtures of polyethylene glycol and dextran, the interfacial tension is estimated to increase by nearly an order of magnitude from 0.32 mN/m to 2.32 mN/m over a total polymer concentration range from 0.55 g/mL to 0.95 g/mL. The methodology and analysis presented here provides a tool for readily accessing mixture compositions that are not easily achieved in bulk solutions, and also for estimating extremely low interfacial tensions between two liquid phases in a compound droplet, such as those formed by aqueous two-phase systems. Further, this platform provides a tool to simultaneously map the phase diagram of these systems. Since the presence and concentration of various additives can have a strong effect on both the interfacial tension and the binodal curve, this work will have a significant impact on the ability to quickly and easily characterize these systems.

2.5.   References

1.   Albertsson, P. Å. *Partition of Cell Particles and Macromolecules*. (John Wiley & Sons, 1986).

2.   Zaslavsky, B. Y. *Aqueous Two-Phase Partitioning*. (Marcel Dekker, 1994).

3.   Ryden, J. & Albertsson, P. Interfacial tension of dextran—polyethylene glycol—water two—phase systems. *J. Colloid Interface Sci.* **37,** 219–222 (1971).

4.   Liu, Y., Lipowsky, R. & Dimova, R. Concentration dependence of the interfacial tension for aqueous two-phase polymer solutions of dextran and polyethylene glycol. *Langmuir* **28,** 3831–9 (2012).

5.   Forciniti, D., Hall, C. K. & Kula, M. R. Interfacial tension of polyethyleneglycol-dextran-water systems: influence of temperature and polymer molecular weight. *J. Biotechnol.* **16,** 279–296 (1990).

6.   *Food Colloids and Polymers: Stability and Mechanical Properties*. (1993).

7.   Rosen, M. J., Wang, H., Shen, P. & Zhu, Y. Ultralow Interfacial Tension for Enhanced Oil Recovery at Very Low Surfactant Concentrations. *Langmuir* **21,** 3749–3756 (2005).

8.   Salager, J.-L., Forgiarini, A. M., Marquez, L., Manchego, L. & Bullon, J. How to Attain Ultralow Interfacial Tension and Three-Phase Behavior with Surfactant Formulation for Enhanced Oil Recovery : A Review . Part 1 . Optimum Formulation for Simple Surfactant – Oil – Water Ternary Systems. *J. Surfactants Deterg.* **16,** 449–472 (2013).

9.   Diamond, A. D. & Hsu, J. T. Aqueous Two-Phase Systems for Biomolecule Separation. *Adv. Biochem. Eng. Biotechnol.* **47,** 89–135 (1992).

10.   Diamond, A. D. & Hsu, J. T. Fundamental studies of biomolecule partitioning in aqueous two-phase systems. *Biotechnol. Bioeng.* **34,** 1000–1014 (1989).

11.   Przybycien, T. M., Pujar, N. S. & Steele, L. M. Alternative bioseparation operations: life beyond packed-bed chromatography. *Curr. Opin. Biotechnol.* **15,** 469–78 (2004).

12.   Zhang, M. *et al.* Single-Step Total Fractionation of Single-Wall Carbon Nanotubes by Countercurrent Chromatography. *Anal. Chem.* **86,** 3980–3984 (2014).

13.   Fagan, J. a *et al.* Isolation of Specific Small-Diameter Single-Wall Carbon Nanotube Species via Aqueous Two-Phase Extraction. *Adv. Mater.* **26,** 2800–2804 (2014).

14.   Subbaiyan, N. K. *et al.* Role of Surfactants and Salt in Aqueous Two-Phase

Separation of Carbon Nanotubes toward Simple Chirality Isolation. *ACS Nano* **8,** 1619–1628 (2014).

15.   Zaslavsky, B. Y. *et al.* Structure of water as a key factor of phase separation in aqueous mixtures of two nonionic polymers. *Polymer (Guildf).* **30,** 2104–2111 (1989).

16.   Berg, J. C. *Interfaces & Colloids*. (World Scientific, 2010).

17.   Hoorfar, M. & W. Neumann, A. Recent progress in Axisymmetric Drop Shape Analysis (ADSA). *Adv. Colloid Interface Sci.* **121,** 25–49 (2006).

18.   Alvarez, N. J., Walker, L. M. & Anna, S. L. A non-gradient based algorithm for the determination of surface tension from a pendant drop: Application to low Bond number drop shapes. *J. Colloid Interface Sci.* **333,** 557–562 (2009).

19.   Saad, S. M. I., Policova, Z., Acosta, E. J. & Neumann, a. W. Range of Validity of Drop Shape Techniques for Surface Tension Measurement. *Langmuir* **26,** 14004–14013 (2010).

20.   Boyce, J. F., Schürch, S., Rotenberg, Y. & Neumann, A. W. The measurement of surface and interfacial tension by the axisymmetric drop technique. *Colloids and Surfaces* **9,** 307–317 (1984).

21.   Holgado-Terriza, J. a., Gómez-Lopera, J. F., Luque-Escamilla, P. L., Atae-Allah, C. & Cabrerizo-Vílchez, M. a. Measurement of ultralow interfacial tension with ADSA using an entropic edge-detector. *Colloids Surfaces A Physicochem. Eng. Asp.* **156,** 579–586 (1999).

22.   Atefi, E., Mann, J. A. & Tavana, H. Ultralow Interfacial Tensions of Aqueous Two-Phase Systems Measured Using Drop Shape. *Langmuir* **30,** 9691–9699 (2014).

23.   Sottmann, T. & Strey, R. Ultralow interfacial tensions in water–n-alkane–surfactant systems. *J. Chem. Phys.* **106,** 8606 (1997).

24.   Bamberger, S., Seaman, G. V. ., Sharp, K. . & Brooks, D. E. The effects of salts on the interfacial tension of aqueous dextran poly(ethylene glycol) phase systems. *J. Colloid Interface Sci.* **99,** 194–200 (1984).

25.   Seeto, Y. & Scriven, L. E. Precision spinning drop interfacial tensiometer. *Rev. Sci. Instrum.* **53,** 1757 (1982).

26.   Princen, H. ., Zia, I. Y. . & Mason, S. . Measurement of interfacial tension from the shape of a rotating drop. *J. Colloid Interface Sci.* **23,** 99–107 (1967).

27.   Vonnegut, B. Rotating bubble method for the determination of surface and interfacial tensions. *Rev. Sci. Instrum.* **13,** 6–9 (1942).

28.   Manning, C. D. & Scriven, L. E. On interfacial tension measurement with a spinning drop in gyrostatic equilibrium. *Rev. Sci. Instrum.* **48,** 1699 (1977).

29. Jones, M. N. The interaction of sodium dodecyl sulfate with polyethylene oxide. *J. Colloid Interface Sci.* **23,** 36–42 (1967).

30. Glyk, A., Scheper, T. & Beutel, S. Influence of Different Phase-Forming Parameters on the Phase Diagram of Several PEG–Salt Aqueous Two-Phase Systems. *J. Chem. Eng. Data* **59,** 850–859 (2014).

31. Brosseau, Q., Vrignon, J. & Baret, J.-C. Microfluidic Dynamic Interfacial Tensiometry (μDIT). *Soft Matter* **10,** 3066 (2014).

32. Hudson, S. D., Cabral, J. T., Goodrum, W. J., Beers, K. L. & Amis, E. J. Microfluidic interfacial tensiometry. *Appl. Phys. Lett.* **87,** 081905 (2005).

33. Xu, J. H., Li, S. W., Lan, W. J. & Luo, G. S. Microfluidic Approach for Rapid Interfacial Tension Measurement. *Langmuir* **24,** 11287–11292 (2008).

34. Gu, H., Duits, M. H. G. & Mugele, F. Interfacial tension measurements with microfluidic tapered channels. *Colloids Surfaces A Physicochem. Eng. Asp.* **389,** 38–42 (2011).

35. Alvarez, N. J., Walker, L. M. & Anna, S. L. A Microtensiometer To Probe the Effect of Radius of Curvature on Surfactant Transport to a Spherical Interface. *Langmuir* **26,** 13310–13319 (2010).

36. Hardt, S. & Hahn, T. Microfluidics with aqueous two-phase systems. *Lab Chip* **12,** 434–442 (2012).

37. Yamada, M., Kasim, V., Nakashima, M., Edahiro, J. & Seki, M. Continuous cell partitioning using an aqueous two-phase flow system in microfluidic devices. *Biotechnol. Bioeng.* **88,** 489–94 (2004).

38. Nam, K.-H. *et al.* Continuous-Flow Fractionation of Animal Cells in Microfluidic Device Using Aqueous Two-Phase Extraction. *Biomed. Microdevices* **7,** 189–195 (2005).

39. Frampton, J. P., Lai, D., Sriram, H. & Takayama, S. Precisely targeted delivery of cells and biomolecules within microchannels using aqueous two-phase systems. *Biomed. Microdevices* **13,** 1043–51 (2011).

40. Soohoo, J. R. & Walker, G. M. Microfluidic aqueous two phase system for leukocyte concentration from whole blood. *Biomed. Microdevices* **11,** 323–9 (2009).

41. Meagher, R. J., Light, Y. K. & Singh, A. K. Rapid, continuous purification of proteins in a microfluidic device using genetically-engineered partition tags. *Lab Chip* **8,** 527–32 (2008).

42. Hartounian, H., Kaler, E. W. & Sandler, S. I. Aqueous Two-Phase Systems. 2. Protein Partitioning. *Ind. Eng. Chem. Res.* **33,** 2294–2300 (1994).

43. Hu, R. *et al.* Rapid, highly efficient extraction and purification of

membrane proteins using a microfluidic continuous-flow based aqueous two-phase system. *J. Chromatogr. A* **1218,** 171–177 (2011).

44. Ziemecka, I., van Steijn, V., Koper, G. J. M., Kreutzer, M. T. & van Esch, J. H. All-aqueous core-shell droplets produced in a microfluidic device. *Soft Matter* **7,** 9878 (2011).

45. Ziemecka, I. *et al.* Monodisperse hydrogel microspheres by forced droplet formation in aqueous two-phase systems. *Lab Chip* **11,** 620–624 (2011).

46. Moon, B.-U., Jones, S. G., Hwang, D. K. & Tsai, S. S. H. Microfluidic generation of aqueous two-phase system (ATPS) droplets by controlled pulsating inlet pressures. *Lab Chip* **15,** 2437–2444 (2015).

47. Lai, D., Frampton, J. P., Sriram, H. & Takayama, S. Rounded multi-level microchannels with orifices made in one exposure enable aqueous two-phase system droplet microfluidics. *Lab Chip* **11,** 3551–4 (2011).

48. Song, Y. & Shum, H. C. Monodisperse w/w/w Double Emulsion Induced by Phase Separation. *Langmuir* **28,** 12054–9 (2012).

49. Wijethunga, P. A. L. & Moon, H. On-chip aqueous two-phase system (ATPS) formation, consequential self-mixing, and their influence on drop-to-drop aqueous two-phase extraction kinetics. *J. Micromechanics Microengineering* **25,** 094002 (2015).

50. Tavana, H. *et al.* Nanolitre liquid patterning in aqueous environments for spatially defined reagent delivery to mammalian cells. *Nat. Mater.* **8,** 736–741 (2009).

51. Atefi, E., Joshi, R., Mann, J. A. & Tavana, H. Interfacial Tension Effect on Cell Partition in Aqueous Two-Phase Systems. *ACS Appl. Mater. Interfaces* **7,** 21305–21314 (2015).

52. Silva, D. F. C. *et al.* Determination of aqueous two phase system binodal curves using a microfluidic device. *J. Chromatogr. A* **1370,** 115–120 (2014).

53. Shim, J.-U. *et al.* Control and measurement of the phase behavior of aqueous solutions using microfluidics. *J. Am. Chem. Soc.* **129,** 8825–35 (2007).

54. Boreyko, J. B., Mruetusatorn, P., Retterer, S. T. & Collier, C. P. Aqueous two-phase microdroplets with reversible phase transitions. *Lab Chip* **13,** 1295–301 (2013).

55. Moreau, P., Dehmoune, J., Salmon, J.-B. & Leng, J. Microevaporators with accumulators for the screening of phase diagrams of aqueous solutions. *Appl. Phys. Lett.* **95,** 033108 (2009).

56. Kojima, T. & Takayama, S. Microscale determination of aqueous two phase system binodals by droplet dehydration in oil. *Anal. Chem.* **85,** 5213–8 (2013).

57.   Hammer, S., Pfennig, A. & Stumpf, M. Liquid-liquid and vapor-liquid equilibria in water + poly(ethylene glycol) + sodium sulfate. *J. Chem. Eng. Data* **39,** 409–413 (1994).

58.   Whitesides, G. & Stroock, A. Flexible methods for microfluidics. *Phys. Today* **54,** 42–48 (2001).

59.   Boukellal, H., Selimović, S., Jia, Y., Cristobal, G. & Fraden, S. Simple, robust storage of drops and fluids in a microfluidic device. *Lab Chip* **9,** 331–8 (2009).

60.   Bithi, S. S. & Vanapalli, S. A. Behavior of a train of droplets in a fluidic network with hydrodynamic traps. *Biomicrofluidics* **4,** 044110 (2010).

61.   Sun, M., Bithi, S. S. & Vanapalli, S. A. Microfluidic static droplet arrays with tuneable gradients in material composition. *Lab Chip* **11,** 3949–52 (2011).

62.   Vuong, S. M. A Microfluidic Platform for the Control and Analysis of Phase Transitions in Concentrating Droplets. PhD Thesis, CMU (2014).

63.   Vuong, S. M. & Anna, S. L. Tuning bubbly structures in microchannels. *Biomicrofluidics* **6,** 022004 (2012).

64.   Christopher, G. F. B. Manipulation of Droplets in Microfluidic Channels using T-Junction Geometry. (2008).

65.   Figliola, R. S. & Beasley, D. E. *Theory and Design for Mechanical Measurements*. (John Wiley & Sons, 2006).

66.   Shim, J. *et al.* Controlling the contents of microdroplets by exploiting the permeability of PDMS. *Lab Chip* **11,** 1132 (2011).

67.   Ottino, J. M. & Wiggins, S. Introduction: mixing in microfluidics. *Philos. Trans. A. Math. Phys. Eng. Sci.* **362,** 923–935 (2004).

68.   Torza, S. & Mason, S. G. Three-phase interactions in shear and electrical fields. *J. Colloid Interface Sci.* **33,** 67–83 (1970).

69.   Zaslavsky, B. Y., Mestechkina, N. M., Miheeva, L. M. & Rogozhin, S. V. Measurement of relative hydrophobicity of amino acid side-chains by partition in an aqueous two-phase polymeric system: Hydrophobicity scale for non-polar and ionogenic side-chains. *J. Chromatogr. A* **240,** 21–28 (1982).

70.   Gulyaeva, N., Zaslavsky, A., Lechner, P., Chait, A. & Zaslavsky, B. Relative hydrophobicity of organic compounds measured by partitioning in aqueous two-phase systems. *J. Chromatogr. B Biomed. Sci. Appl.* **743,** 187–194 (2000).

71.   Vijayakumar, K., Gulati, S., deMello, A. J. & Edel, J. B. Rapid cell extraction in aqueous two-phase microdroplet systems. *Chem. Sci.* **1,** 447 (2010).

72. Deng, N.-N. *et al.* Wetting-induced formation of controllable monodisperse multiple emulsions in microfluidics. *Lab Chip* **13,** 4047–4052 (2013).

73. Guzowski, J. & Garstecki, P. Comment on 'Wetting-induced formation of controllable monodisperse multiple emulsions in microfluidics' by N.-N. Deng, W. Wang, X.-J. Ju, R. Xie, D. A. Weitz and L.-Y. Chu, Lab Chip, 2013, 13 , 4047. *Lab Chip* **14,** 1477–1478 (2014).

74. Deng, N.-N. *et al.* Reply to the 'Comment on "Wetting-induced formation of controllable monodisperse multiple emulsions in microfluidics"' by J. Guzowski and P. Garstecki, Lab Chip, 2014, 14, DOI: 10.1039/C3LC51229K. *Lab Chip* **14,** 1479 (2014).

75. Pannacci, N. *et al.* Equilibrium and nonequilibrium states in microfluidic double emulsions. *Phys. Rev. Lett.* **101,** 1–4 (2008).

76. Guzowski, J., Korczyk, P. M., Jakiela, S. & Garstecki, P. The structure and stability of multiple micro-droplets. *Soft Matter* **8,** 7269 (2012).

77. Santini, E., Liggieri, L., Sacca, L., Clausse, D. & Ravera, F. Interfacial rheology of Span 80 adsorbed layers at paraffin oil–water interface and correlation with the corresponding emulsion properties. *Colloids Surfaces A Physicochem. Eng. Asp.* **309,** 270–279 (2007).

78. Wu, Y.-T., Zhu, Z.-Q. & Mei, L.-H. Interfacial Tension of Poly(ethylene glycol) + Salt + Water Systems. *J. Chem. Eng. Data* **41,** 1032–1035 (1996).

Chapter 3. Design, Construction, and the Operation of a Millimeter-scale Droplet Generating Platform with Integrated Absorbance Spectroscopy

3.1. Introduction

In Chapter 2 a microfluidic device was used to study the phase separation and dewetting of an aqueous two-phase system. The characteristic dimension of the channels containing the droplets was approximately 150 - 350 μm and the device was fabricated using standard soft lithography techniques. Operating at a length scale of tens to hundreds of microns has many benefits. For example, in Chapter 2 the high surface-to-volume ratio of the nanoliter-sized droplets was exploited to enable dehydration, and thus phase separation. Other benefits of traditional microfluidic devices arise from the fact that interfacial forces typically dominate inertia, viscous forces, and gravitational effects[1]. The benefits afforded by operating in these regimes are well documented and are described in detail in Chapter 2 and elsewhere[2,3].

In other cases, however, operating devices with micrometer length scales introduces significant challenges. One example is mixing[4–6]. The dominance of viscous forces over inertia leads to laminar, reversible fluid flow. Turbulence is eliminated and mixing is limited to that which occurs by diffusion. If mixing is desirable, special care must be taken in the design and operation of the microfluidic device to ensure satisfactory mixing through mechanisms such as chaotic advection[4,7–9]. Another important area where reduced length scales present special challenges is in the application of spectroscopic detection methods. Determining the presence and concentration of an analyte inside a microfluidic

droplet is of considerable interest. Spectroscopic detection methods are rapid, non-invasive, non-destructive techniques found in most laboratories and are applicable to a wide range of analyte types. However, integrating these techniques into a PDMS micro-device is nontrivial[10]. In absorption spectroscopy, the absorbance at a specific wavelength is linearly proportional to the path length of the light through the solution, given by Beer-Lambert's law[11],

$$A = \varepsilon C l \tag{3.1}$$

where A is the absorbance, C is the concentration of analyte, ε is the molar absorption coefficient, and l is the path length. The absorption coefficient is a property of the analyte and is a function of the wavelength of the transmitted light. Traditional microfluidic devices have small optical path lengths, typically $10 < l < 100$ μm. This may be beneficial for imaging extremely turbid or highly absorbing samples, such as carbon black, which would typically be too opaque at macroscopic scales to support transmitted light based imaging techniques. However in less turbid samples or in the case of optical absorbance measurements, a small optical path length is undesirable. The upper and lower bounds of the path length are fundamentally limited by the thickness of PDMS device molds, which are generated by spin coating thin films of photosensitive polymer onto silicon wafers. Similar limitations apply to fabrication techniques for glass devices.

The small path length and the need to monitor the device with a large and expensive inverted microscope to reliably capture only a portion of each nanoliter

sized drop results in poor sensitivity and noise[12]. Additionally, while the large surface-to-volume ratio inherent to microfluidic fluid volumes can be desirable, the existence of large amounts of fluid-fluid interface complicates spectroscopic measurements. The curvature of the interfaces and the refractive index differences between the fluids scatter light due to lensing effects near the interface. This manifests as dark bands around the droplets when viewed with bright field illumination. Finally, the device material and the continuous phase fluid may interfere with optical absorbance measurements due to unwanted absorption, especially for wavelengths outside of the visible spectrum. Other notable drawbacks of traditional microfluidic devices include their need for complex fabrication techniques and/or access to clean room facilities, high initial cost, and limited materials selection and compatibility.

In an effort to address these drawbacks while preserving the droplet-based fluid handling techniques associated with microfluidic methodologies, the idea of millimeter-scale fluidic devices or 'millifluidics' has been introduced to the field of microfluidics. This advance is enabled by increasing the characteristic dimensions of the channels from tens of microns to several millimeters. Millifluidic devices and techniques have been reported previously in the literature both as a novel experimental technique[13–16], where their benefits compared to microfluidics are emphasized, and in applications[17–42] ranging from biology[30,38,41] to heterogeneous catalysis[34]. Scaling up allows the use of commercial tubing and chromatography-type fittings with circular cross sections, although some groups have constructed millimeter scale channels with rectangular cross sections in

planar devices[17,19,35]. Millifluidic devices have been utilized to study droplet traffic in fluid networks[18,37], investigate crystallization[31,39,40], as well as polymerization and particle fabrication[13,14,19,20,23,25–27,29].

In this chapter we describe the design, construction, and operation of a droplet-based fluid handling platform which addresses the limitations inherent to optical absorbance measurements in microfluidic devices. We accomplish this by adopting millifluidic techniques; increasing the characteristic dimensions of the fluid handling device from $10 - 100$ μm to $1.0 - 1.5$ mm. The change in length scale provides several benefits while maintaining the droplet generating and fluid handling techniques associated with microfluidic flows. First, complex clean room fabrication techniques, such as photolithography, are replaced by the assembly of off-the-shelf commercial fittings, tubing, and micro-bore capillaries. Second, the use of commercial tubing and fittings dramatically expands the selection of wetted materials available, eliminating the need for complicated surface treatments or excessive quantities of surfactants in order to obtain ideal wetting conditions. Third, the increased diameter of the fluid channels allows for larger optical path lengths, which assure accurate and repeatable measurements of concentration via absorbance spectroscopy. Finally, the increased length scale allows for greater control over the relative impact of interfacial forces, inertia, and gravity. Careful selection of the continuous phase fluid, the presence of surfactants, and the imposed fluid velocity enable the platform to operate over a range of Reynolds, capillary, and Bond numbers, including regimes where these dimensionless groups are of the order 0.01 to 10.

3.2.   Materials and Construction

A millifluidic co-flow type droplet generator is constructed using off-the-shelf tubing (Cole Parmer, IDEX Scientific, VitroCom) and commercial chromatography fittings (IDEX Scientific and VICI Valco). The three principle components of the device are the droplet generator, the storage section, and an optical flow cell for in-situ absorbance measurements.
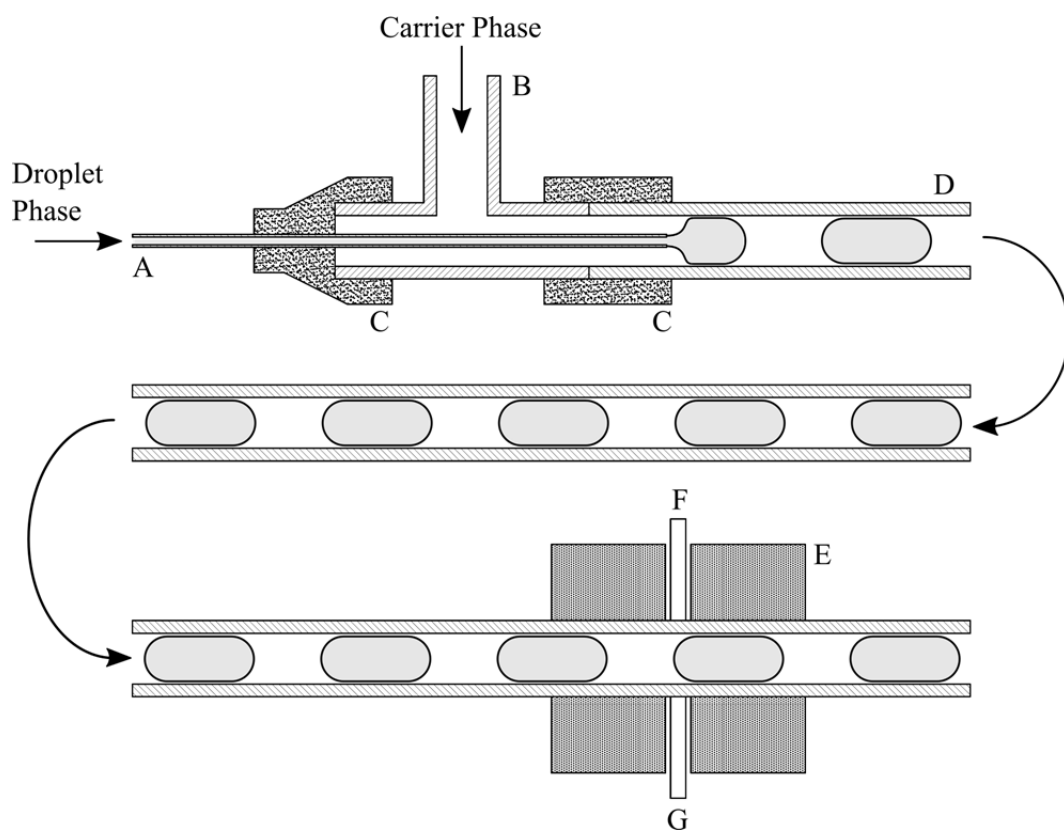
Figure 3.1. Schematic diagram of the principle components comprising the millifluidic apparatus. (A) Nozzle for the droplet phase fluid to enter the coflowing droplet generator. (B) A T-fitting which provides the structure for assembling the droplet generator and allows the continuous or 'carrier' phase fluid to enter the device. (C) Slip-fit connections between the various device components form water proof seals and aid in aligning the inner capillary. (D) A length of tubing to hold, store, and deliver the droplets downstream.(E) An optical flow cell to rigidly align the tubing and the optical fibers. (F) Optical fiber from light source. (G) Optical fiber to spectrophotometer. Droplets are shown schematically in grey. The inner diameter of the tubing may vary in order to suit the application, and ranges from about 0.8 to 2 mm.

Figure 3.1 provides a generic schematic diagram of a typical millimeter scale platform for generating droplets of arbitrary composition and then delivering them to an optical flow cell for spectroscopic determination of concentration. The droplet generator is constructed by assembling a coflow type junction with an inner capillary (A), T-fitting (B), and water tight connections (C). The connections are made by slipping one piece of tubing over the joint, forming a friction-fit connection. Alternatively, a marine grade epoxy may be used to seal the joints. Droplets travel down some length of 'storage' tubing (D), which may be thermostated, exposed to UV light, or subject to some other condition. The length of the storage tubing determines the residence time of the droplets, which is important for processes that have specific time scales.

Multiple syringe pumps, not shown, deliver fluids into the nozzle and the T-fitting. The relative flow rates of the droplet phase fluid and the carrier phase fluid control the size, spacing, velocity, and composition of the droplets. Multiple components can be combined to form the droplet phase fluid prior to droplet generation by using manifolds or Y-junctions upstream of the nozzle. After generation the droplets flow through the storage tubing and onward to a UV/Vis/NIR absorption flow cell. Because the spectrophotometer is integrated in line with the fluidic components via optical fibers, absorbance measurements may be obtained from moving droplets *in situ*. The optical fibers may be aligned with the storage tubing using a custom machined acrylic flow cell, or any cross-fitting which will fit the tubing and fibers and rigidly align them.

The exact type of components and their dimensions are not critical to the droplet formation process, and vary depending on the application. However, selection of correct wetted material for the continuous phase fluid in use is critical. The continuous phase fluid must preferentially wet the nozzle, T-junction, storage tubing, and all of the downstream components. Unwanted wetting of the droplet-phase fluid to the device material leads to erratic droplet formation and random droplet collision and merging, which impacts the concentration of the droplets. For example, in Chapter 4, aqueous droplets containing an organic emulsion are formed in a perfluorocarbon carrier fluid. As a result, PTFE fittings and tubing are chosen for the materials. For other experiments, mineral oil continuous phase fluids would require the use of polyethylene tubing, or another polymer which was preferentially wet by alkanes. If water is the continuous phase fluid, glass would be a suitable material.

	Component	Example and Manufacturer
A	Nozzle	Glass capillaries (WPI Sci.), PEEK tubing (IDEX Sci.), High Gauge PTFE tubing (Cole Parmer)
B	T-fitting	Barbed T-fittings (Cole Parmer), CTFE fittings (VICI Valco), PEEK fittings (IDEX Sci.)
C	Seals	Silicone tubing (Cole Parmer), Tygon tubing (Cole Parmer), Epoxy resin (Various), Threaded fittings (IDEX Sci.)
D	Storage Tubing	Low Gauge PTFE Tubing (Cole Parmer), Glass capillary (WPI Sci), Tygon tubing (Cole Parmer), FEP tubing (IDEX Sci.)

Table 3.1. An example parts list for construction of a millifluidic droplet generator. The labels A-D correspond to the notation used in Figure 3.1.

Table 3.1 provides a list of parts for construction of a millifluidic-type platform as shown in Figure 3.1. Each of the example components is commercially available with a range of dimensions, surface roughness, and chemical compatibility. Specific part numbers, dimensions, and step by step construction steps are provided in the materials and methods section of Chapter 4 for a device in which the continuous phase fluid is a perfluorocarbon.

Optical detection of the droplet compartments may be accomplished through microscopy, UV/Vis absorbance spectroscopy, or both. Images of the droplet compartments are captured at a fixed frequency as they flow through the field of view during the course of an experiment. The type of material selected for the storage tubing influences the quality of the optical detection. PTFE tubing, for example, often scatters low wavelength light, which leads to poor absorbance measurements below about 500 nm. Fluorinated ethylene propylene (FEP) is an alternative to PTFE which is optically transparent across a range of wavelengths, but is still preferentially wet by perfluorocarbon fluids. Some tubing manufacturing and finishing processes impart the tubing with significant surface roughness, which will affect the ability to pass light through. In these cases, coating the exterior of the tubing in microscope objective immersion oil can solve the problem. Finally, a quartz capillary may be used if the glass surface has been modified by a surface coating process suitable for the continuous phase fluid.

Maintaining registry amongst a library of droplets is important for assigning the data acquired from a specific droplet to the conditions inside that droplet. A train of 30-40 droplets can be generated in which the concentration of

one component in each droplet varies from droplet to droplet in a linearly increasing manner. Matching the time when the pumps were commanded to begin the concentration gradient to the first droplet in that gradient can be challenging. To aid in maintaining registry, a fluid injection circuit is designed to inject fluid spacers to aid in visual determination of the droplet registry.
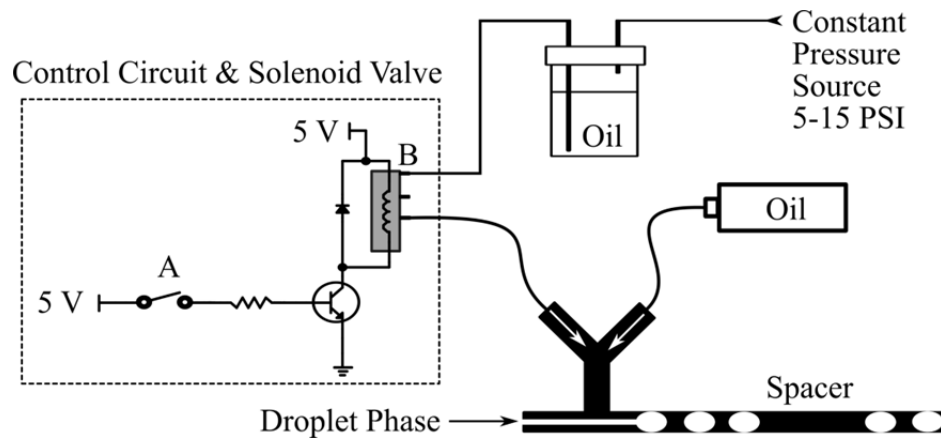
Figure 3.**2**. Schematic diagram of the system used to inject oil boluses into the millifluidic platform. At right, in the dashed box, is a circuit to control the micro solenoid valve (gray box). The solenoid valve (B) is connected to a pressure reservoir of continuous phase fluid, in this case oil. Pressure in the reservoir is maintained with compressed dry air. When the switch (A) is closed oil exits the solenoid and enters the coflowing droplet generator upstream of droplet production.

Figure 3.2 is a schematic diagram of the pressure control system used to insert continuous phase fluid 'spacers' into the train of droplets. The control circuit is constructed on a solderless breadboard and the layout and the specification of the electrical components are provided by the solenoid valve manufacturer.

During droplet generation a momentary contact switch (A) is struck, opening a micro solenoid valve (B) (LFA, LEE Valve Co), allowing high pressure oil (10 PSI) to flow into the droplet generator for a brief (< 1 s) period of time. Droplets that have already been formed are accelerated slightly downstream, and droplet

production is momentary paused due to the sudden pressure increase. The continuous phase bolus functions as a registry indicator within the linear train of droplets and can be detected by the spectrophotometer as a gap in the absorbance trace. Injection of the spacer is done manually. The timing of the spacer relative to when the gradient begins is determined by the amount of time it takes for the droplet phase fluids to travel from the manifold, which is located upstream of the end of the nozzle, to the nozzle exit in the T-junction.

3.3.   Designing Compositional Gradients

While generating populations of identical droplets is good for studying stochastic phenomena, being able to vary the composition of the droplets in a predictable manner is advantageous for many applications. Care is required when designing composition gradients to ensure droplets attain the expected composition. When multiple fluid streams are combined in order to form a droplet, the composition of that droplet is a function of both the volumetric flow rate of each fluid stream as well as its concentration. At any instant in time, the composition exiting the nozzle of the droplet generator may be calculated from conservation of mass,

$$C_i^{drop} = \frac{C_i^{syringe} Q_i}{\sum_{i=1}^{n} Q_i},$$

(3.2)

where C_i is the concentration of the ith component, Q_i is the volumetric flow rate of the syringe containing that component, and n is the total number of syringes for the droplet phase fluid. By varying the volumetric flow rate, Q_i, of at least two

pumps, the concentration of one or more components can be varied from droplet-to-droplet while keeping the volume of the droplet and concentration of every other component constant. The total number of syringe pumps required to generate a desired composition gradient will depend on the number of syringes assigned to each pump, and whether the absolute concentration of a component is being varied, or a ratio between two components is being varied.

The simplest configuration is a one-dimensional (1D) gradient. The concentration of one additive is varied while the concentration of the other components remains constant. For a simple system composed of a single water-soluble component, such as a dye, only two pumps are required for the droplet phase fluid. One pump contains a concentrated solution of dye, and the other contains pure water. Varying the volumetric flow rate ratio between the two pumps, while keeping the total flow rate constant, varies the concentration of dye in each droplet.
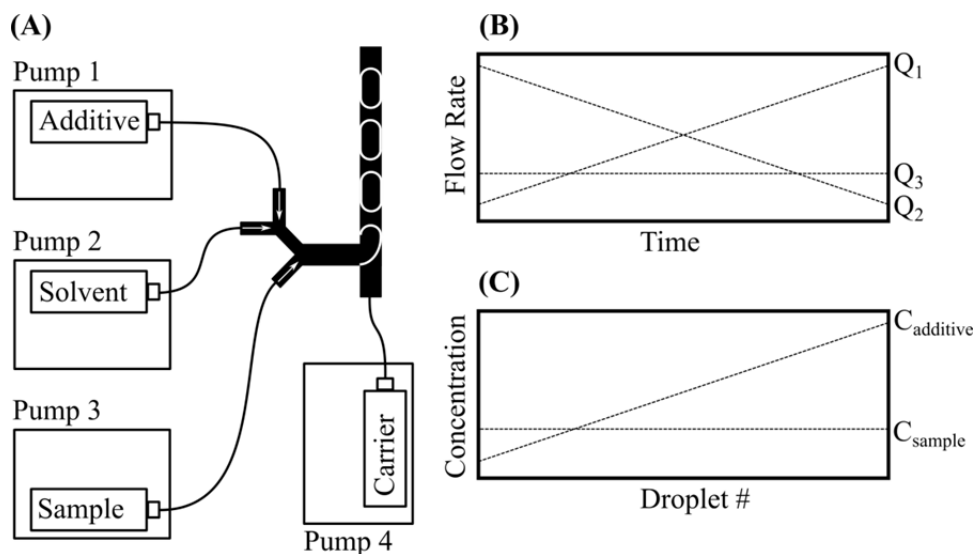
Figure 3.3. (A) The physical pump topology for generating a 1D gradient in droplet composition. The ratio of the flow rates between Pump 1 and Pump2 is adjusted to achieve the desired droplet concentration. Pump 3 contains a sample whose concentration is kept constant. (B) A plot of the volumetric flow rate of each component as a function of time. (C) A plot of the concentration of each component in the droplets as a function of droplet number.

An example pump topology for a 1D gradient is show schematically in Figure 3.3 (A). Droplets are generated containing a sample and a variable amount of some additive. The concentration of the additive is varied by dilution with an appropriate solvent, for example a concentrated salt solution and water. The total volumetric flow rate of the three droplet phase pumps is kept constant, but the ratio between Pump 1 and Pump 2 is varied. Figures 3.3 (B) and (C) are representative plots of the flow rate of each pump and the concentration of each component delivered to the droplets, respectively. In Figure 3.3 (B) the volumetric flow rate of Pump 2 decreases as the volumetric flow rate of Pump 1 increases. In Figure 3.3 (C) the concentration delivered to the droplets as a result of the change in flow rate is plotted. The concentration of sample remains constant while the additive concentration varies.

More complicated gradients in droplet composition may be generated with only three independent syringe pumps. A 2D gradient in droplet composition is possible by varying the flow rate ratio between two different additives.
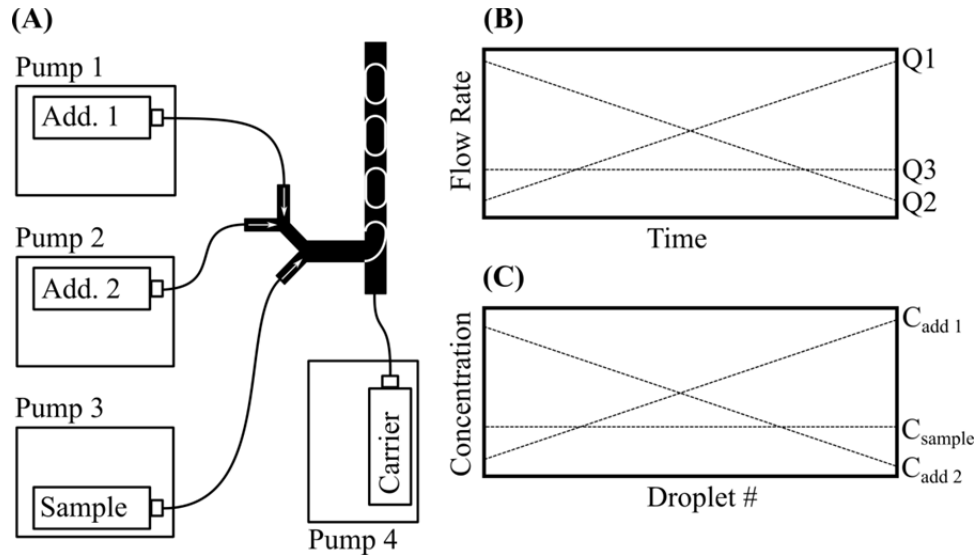
Figure 3.4. (A) The pump topology for generating a 2D gradient in droplet composition. Similar to Figure 3.3, the ratio of the flow rates between Pump 1 and Pump 2 is adjusted to achieve the desired droplet concentration, while the flow rate of Pump 3 is kept constant. (B) A plot of the volumetric flow rate of each component as a function of time. (C) A plot of the concentration of each component in the droplets as a function of droplet number. Compared with Figure 3, the composition plot now contains two additives rather than one.

In Figure 3.4 the physical pump topology and the corresponding plots for flow rate and droplet concentration for a 2D concentration gradient are shown. Pump 1 and Pump 2 now contain two separate additives. In Figure 3.4 (B) the gradient in droplet composition is generated by varying the ratio of flow rates between Pump 1 and Pump 2, as in the case of the 1D gradient. In Figure 3.4 (C) the concentration of each of the two additives varies linearly, directly proportional to the change in flow rate of each corresponding syringe. The total volumetric flow rate of the droplet phase fluids is kept constant.

64

In Figures 3.3 and 3.4 each syringe pump hosted only one syringe containing a single additive. Many syringe pumps can control more than one syringe at a time, allowing for the formation of complex gradients with only a limited number of pumps. In this way, many components can be present in every droplet, although the concentration of only a subset of those components may be varied.
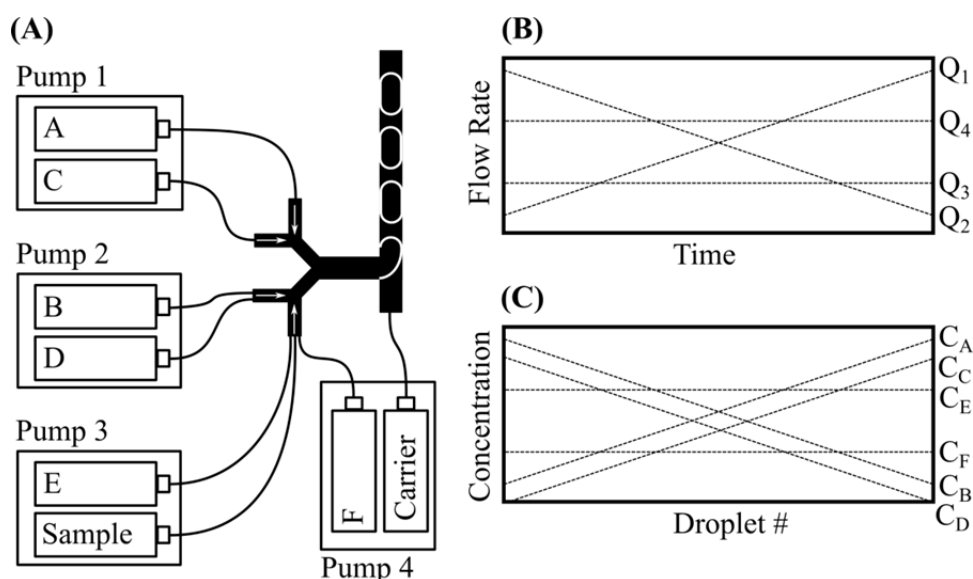
Figure 3.5. (A) The pump topology for generating a 4D gradient in droplet composition. The volumetric flow rate of Pumps 1 and 2 vary. The flow rate of Pump 3 and 4 are kept constant. (B) A plot of the volumetric flow rate of each component as a function of time. (C) A plot of the concentration of each component in the droplets as a function of droplet number.

In Figure 3.5, the ability of the syringe pumps to hold multiple fluid filled syringes is exploited to construct a 4D concentration gradient. The concentration of 4 components, A, B, C, and D, are varied droplet-to-droplet while the concentration of components E, F, and the Sample are kept constant. In Figure 3.5 (B), the flow rates for each syringe pump are sketched schematically. The flow

65

rate for Pump 4, normally assigned to only the carrier phase fluid, is included. In Figure 3.5 (C) the concentration gradients are shown for a system with six additives, labeled A – F, where four of those additives vary in concentration between the droplets.

The millifluidic droplet platform provides a powerful tool for mapping the effect of additives across composition space. However, there are several other limitations on design of the composition gradients. Some of these limitations are related to the mechanical operation of the pumps, while others are related to the physics of droplet generation, the chemistry of the fluids, and the time scales of the physical phenomena being investigated.

Syringe pumps are displacement-based pumps, and dispense a known quantity of fluid volumetrically by advancing a syringe plunger at a controlled speed. A worm gear converts the rotational motion of a stepper motor into linear motion. Syringe pumps apply the force required to maintain the desired volumetric flow rate, up to a mechanical limit. This is in contrast to pressure-based fluid dispensing mechanisms, which apply a constant pressure, but generate a flow rate that depends on the (often time varying) hydraulic resistance of the entire downstream fluidic network.

For the purpose of selecting the number of components to add to a droplet and the topology of the pump network, the most important limitation is the minimum flow rate that can be dispensed. The pulsatile motion of the stepper motor and backlash in the mechanical linkages between the drive and the screw,

as well as the compliance of the plastic syringes and tubing limit the volumetric flow rates and the steepness of the gradient in flow rate that can be generated accurately and precisely[43]. Based on preliminary experiments, we have found that any one time-varying volumetric flow rate cannot be less than approximately 10% of the total volumetric flow rate of dispersed phase fluid,

$$\frac{Q_i}{\sum_{i=1}^{n} Q_i} \geq 0.10 \tag{3.3}$$

Exceeding this limit leads to pulsatile flow, and latency between the time that a pump is commanded to dispense fluid and the time that the fluid actually begins to flow. Ultimately, this translates to increased uncertainty in the composition of the droplets. This limitation on flow rate directly impacts the range of possible droplet concentrations that can be generated in a single experiment, since the concentration is linearly related to the flow rate. Substituting Eq. (3.3) into Eq. (3.3) leads to the expression,

$$C_{i,\min}^{drop} \geq 0.1 C_i^{syringe} \tag{3.4}$$

C_{min} is the minimum concentration of component i in the droplet that can possibly be generated.

The limit provided by Eq. 3.3 also restricts the maximum concentration of any one component in a droplet. For example, in Figure 3.3, Eq. 3.3 applies to both Pump 1 and Pump 2, since both volumetric flow rates are chaning with time. The application of Eq. 3.3 to the second pump sets a maximum droplet

concentration of the additive. Assuming the total volumetric flow rate of the dispersed phase fluid is constant during the generation of the droplet train, then the maximum concentration of a component in a single droplet in is limited by the number of other syringe pumps in the network and their volumetric flow rate. For the pump network depicted in Figure 3.3,

$$C_{i,\max}^{drop} \leq 0.8 C_i^{syringe} \tag{3.5}$$

Where $C_{i,max}$ is the maximum concentration of component i that can be added to a single droplet in the gradient. The coefficient 0.8 arises due to the fact that both Pump 1 and Pump 2 must obey Eq. (3.3), and Pump 3 is set to a constant value of 10% of the total volumetric flow rate. If both Pump 2 and Pump 3 are 10% of the total flow rate, then Pump 1 can only use the remaining 80%. As the number of pumps contributing to the dispersed phase fluid flow is increased, the maximum droplet concentration is reduced, but the minimum is unaffected.

The microliter droplets are generated through a 'squeezing' type, confined breakup mechanism described in detail by Garstecki et. al[44]. To maintain consistent, steady-state droplet production, the capillary number associated with the T-junction droplet generator cannot exceed 0.01,

$$Ca = \frac{\mu_c V_c}{\gamma} \leq 0.01 \tag{3.6}$$

where the subscript c indicates the continuous phase fluid properties, V is the fluid velocity, μ is the viscosity and γ is the interfacial tension between the continuous and dispersed phase fluids.

3.4.   Results

As a proof of concept of the millifluidic platform to be used in Chapters 4 and 5, water droplets mixed with varying concentrations of potassium permanganate are generated. Potassium permanganate is a well characterized water soluble dye with strong absorbance in the visible range. By independently controlling the flow rates of a pure water stream and a concentrated aqueous potassium permanganate stream, we form droplets with a droplet-to-droplet gradient in concentration.
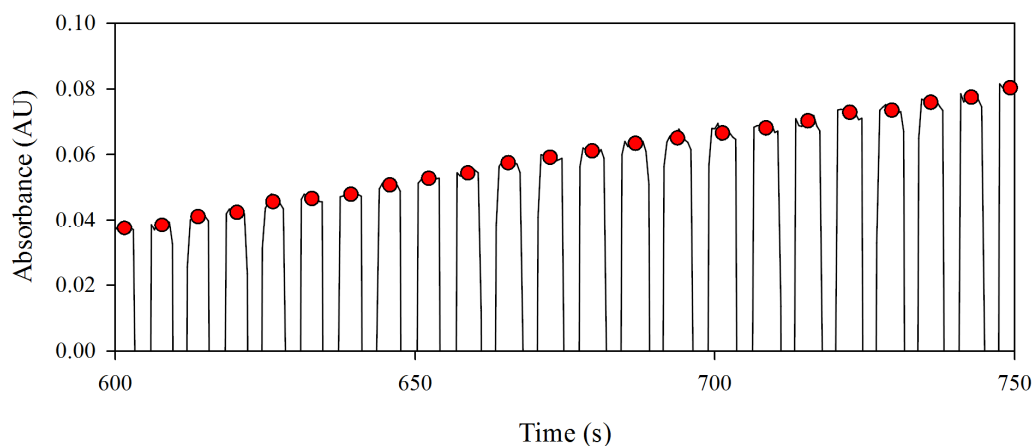
Figure 3.6. A plot of the optical absorbance of droplets containing an increasing concentration of potassium permanganate in water measured at a wavelength of 525 nm. The solid line corresponds to the instantaneous absorbance, and the filled circles correspond to the time averaged absorbance of a single droplet.

Figure 3.6 is the absorbance measured at 525 nm and plotted as a function of time for an experiment in which a series of single phase droplets containing potassium permanganate are generated. The absorbance trace exhibits a series of plateaus and troughs corresponding to the droplets and the continuous phase oil spacers, respectively. The absorbance of the plateau regions increases linearly

with increasing time, from about 0.04 to 0.08 A.U., corresponding to an increase in the concentration of dye added to each droplet by the syringe pumps. The filled circles correspond to the time averaged absorbance of each plateau. The filled circles are determined either by manually averaging the absorbance associated with each droplet, or by using a MATLAB script that detects the location of each plateau by evaluating the forward and backwards derivative at each point, looking for sharp increases and decreases in the absorbance signal that indicate the start and end of each droplet.

The filled symbols can be plotted as a function of composition by converting time to concentration based on the flow rate program assigned to the syringe pumps.
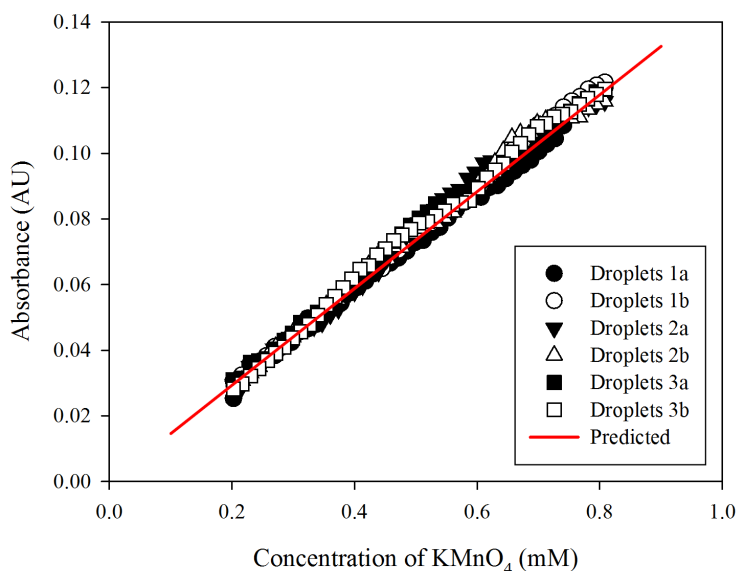
Figure 3.7. A plot of the time-averaged absorbance as a function of the corresponding composition for multiple trains of droplets whose composition is varied over the same range of potassium permanganate concentration. The absorbance of six sets of droplets (open and filled symbols) corresponding to three droplet-based experiments that each produce two replications of the concentration gradient 'up and down' in concentration space. The droplets contain only potassium permanganate and water. The solid line is the expected absorbance calculated from the volumetric flow rates of the pumps, the concentration of the stock solutions, and the extinction coefficient for potassium permanganate which was obtain through a series of calibration experiments.

70

The experiment shown in Figure 3.6 is repeated several times. Figure 3.7 shows the result of three identical experiments, each providing two internal replications, where single-compartment droplets composed of water and varying concentrations of potassium permanganate are generated and measured with the inline spectrophotometer. The open and filled symbols correspond to the time averaged absorbance of individual droplets for the three experiments. The solid line corresponds to the absorbance predicted from the Beer-Lambert law (Eq. 3.1). The extinction coefficient of potassium permanganate is determined from a calibration curve constructed from macroscale experiments and the optical path length is approximately equal to the inner diameter of the tubing. The concentration is estimated based on the volumetric flow rates of the syringe pumps. This procedure generates a prediction for the absorbance of the droplets assuming the millifluidic apparatus is able to generate the requested compositional gradient along the train of droplets.

The symbols agree well with the predicted absorbance, based on input flow rates and the measured absorbance. Figure 3.7 shows that that the millifluidic platform can generate droplets of a known composition and measure their optical absorbance.

3.5.   Conclusions

In this chapter we have outlined the motivation, construction, operation, and proof of concept for a millifluidic platform in which the composition of the droplets can be systematically varied from drop to drop. We have also presented the basis for an optimization-based approach to the problem of selecting flow rates and stock syringe compositions, based on constraints such as capillary number and mechanical limitations of the pumps. One avenue of future work involves constructing an objective function for the problem of pump programming in order to achieve a desired range of droplet composition with a desired compositional resolution. Further, we have shown that we can obtain accurate optical absorbance measurements of flowing droplets. In Chapters 4 and 5, we will use this millifluidic platform to optically interrogate droplets, including multiphase and multi-compartment droplets, in a variety of conditions.

3.6. References

1. Squires, T. M. & Quake, S. R. Microfluidics: Fluid physics at the nanoliter scale. *Rev. Mod. Phys.* **77,** 977–1026 (2005).

2. Seemann, R., Brinkmann, M., Pfohl, T. & Herminghaus, S. Droplet based microfluidics. *Rep. Prog. Phys.* **75,** 016601 (2012).

3. Bremond, N. & Bibette, J. Exploring emulsion science with microfluidics. *Soft Matter* (2012). at <http://pubs.rsc.org/en/content/articlehtml/2012/sm/c2sm25923k>

4. Tice, J. D., Song, H., Lyon, A. D. & Ismagilov, R. F. Formation of Droplets and Mixing in Multiphase Microfluidics at Low Values of the Reynolds and the Capillary Numbers. *Langmuir* **19,** 9127–9133 (2003).

5. Ottino, J. M. & Wiggins, S. Introduction: mixing in microfluidics. *Philos. Trans. A. Math. Phys. Eng. Sci.* **362,** 923–935 (2004).

6. Stone, H. A., Stroock, A. D. & Ajdari, A. ENGINEERING FLOWS IN SMALL DEVICES. *Annu. Rev. Fluid Mech.* **36,** 381–411 (2004).

7. Song, H., Bringer, M. R., Tice, J. D., Gerdts, C. J. & Ismagilov, R. F. Experimental test of scaling of mixing by chaotic advection in droplets moving through microfluidic channels. *Appl. Phys. Lett.* **83,** 4664–4666 (2003).

8. Tice, J. D., Lyon, A. D. & Ismagilov, R. F. Effects of viscosity on droplet formation and mixing in microfluidic channels. *Anal. Chim. Acta* **507,** 73–77 (2004).

9. Song, H., Chen, D. L. & Ismagilov, R. F. Reactions in droplets in microfluidic channels. *Angew. Chemie - Int. Ed.* **45,** 7336–7356 (2006).

10. Gai, H., Li, Y. & Yeung, E. S. Optical detection systems on microfluidic chips. *Top. Curr. Chem.* **304,** 171–201 (2011).

11. Kenkel, J. *Analytical Chemistry for Technicians.* (CRC Press, 1994).

12. Zhu, Y. & Fang, Q. Analytical detection techniques for droplet microfluidics—A review. *Anal. Chim. Acta* **787,** 24–35 (2013).

13. Engl, W., Tachibana, M., Panizza, P. & Backov, R. Millifluidic as a versatile reactor to tune size and aspect ratio of large polymerized objects. *Int. J. Multiph. Flow* **33,** 897–903 (2007).

14. Lorber, N., Pavageau, B. & Mignard, E. Droplet-Based Millifluidics as a New Miniaturized Tool to Investigate Polymerization Reactions. *Macromolecules* **43,** 5524–5529 (2010).

15.   Trivedi, V. *et al.* A modular approach for the generation, storage, mixing, and detection of droplet libraries for high throughput screening. *Lab Chip* **10,** 2433 (2010).

16.   Lorber, N. *et al.* Some recent advances in the design and the use of miniaturized droplet-based continuous process: applications in chemistry and high-pressure microflows. *Lab Chip* **11,** 779–87 (2011).

17.   Cygan, Z. T., Cabral, J. T., Beers, K. L. & Amis, E. J. Microfluidic platform for the generation of organic-phase microreactors. *Langmuir* **21,** 3629–3634 (2005).

18.   Engl, W., Roche, M., Colin, A., Panizza, P. & Ajdari, A. Droplet Traffic at a Simple Junction at Low Capillary Numbers. *Phys. Rev. Lett.* **95,** 208304 (2005).

19.   Barnes, S. E., Cygan, Z. T., Yates, J. K., Beers, K. L. & Amis, E. J. Raman spectroscopic monitoring of droplet polymerization in a microfluidic device. *Analyst* **131,** 1027–33 (2006).

20.   Salazar-Alvarez, G., Muhammed, M. & Zagorodni, A. A. Novel flow injection synthesis of iron oxide nanoparticles with narrow size distribution. *Chem. Eng. Sci.* **61,** 4625–4633 (2006).

21.   Bouquey, M., Serra, C., Berton, N., Prat, L. & Hadziioannou, G. Microfluidic synthesis and assembly of reactive polymer beads to form new structured polymer materials. *Chem. Eng. J.* **135,** 93–98 (2007).

22.   Serra, C., Berton, N., Bouquey, M., Prat, L. & Hadziioannou, G. A predictive approach of the influence of the operating parameters on the size of polymer particles synthesized in a simplified microfluidic system. *Langmuir* **23,** 7745–7750 (2007).

23.   Abou Hassan, A., Sandre, O., Cabuil, V. & Tabeling, P. Synthesis of iron oxide nanoparticles in a microfluidic device: preliminary results in a coaxial flow millichannel. *Chem. Commun. (Camb).* 1783–5 (2008). doi:10.1039/b719550h

24.   Engl, W., Backov, R. & Panizza, P. Controlled production of emulsions and particles by milli- and microfluidic techniques. *Curr. Opin. Colloid Interface Sci.* **13,** 206–216 (2008).

25.   Panizza, P., Engl, W., Hany, C. & Backov, R. Controlled production of hierarchically organized large emulsions and particles using assemblies on line of co-axial flow devices. *Colloids Surfaces A Physicochem. Eng. Asp.* **312,** 24–31 (2008).

26.   Tachibana, M. *et al.* Combining sol-gel chemistry and millifluidic toward engineering microporous silica ceramic final sizes and shapes: An

Integrative Chemistry approach. *Chem. Eng. Process. Process Intensif.* **47,** 1323–1328 (2008).

27.   Gokmen, M. T., Van Camp, W., Colver, P. J., Bon, S. A. F. & Du Prez, F. E. Fabrication of porous clickable polymer beads and rods through generation of high internal phase emulsion (HIPE) droplets in a simple microfluidic device. *Macromolecules* **42,** 9289–9294 (2009).

28.   Chang, Z. *et al.* Multiscale materials from microcontinuous-flow synthesis: ZnO and Au nanoparticle-filled uniform and homogeneous polymer microbeads. *Nanotechnology* **21,** 015605 (2010).

29.   Lorber, N., Pavageau, B. & Mignard, E. Investigating acrylic acid polymerization by using a droplet-based millifluidics approach. *Macromol. Symp.* **296,** 203–209 (2010).

30.   Baraban, L. *et al.* Millifluidic droplet analyser for microbiology. *Lab Chip* **11,** 4057 (2011).

31.   Ildefonso, M., Candoni, N. & Veesler, S. A Cheap, Easy Microfluidic Crystallization Device Ensuring Universal Solvent Compatibility. *Org. Process Res. Dev.* **16,** 556–560 (2012).

32.   Bannock, J. H., Phillips, T. W., Nightingale, A. M. & DeMello, J. C. Microscale separation of immiscible liquids using a porous capillary. *Anal. Methods* **5,** 4991 (2013).

33.   Krishna, K. S. *et al.* Millifluidics for Chemical Synthesis and Time-resolved Mechanistic Studies. *J. Vis. Exp.* (2013). doi:10.3791/50711

34.   Olivon, K. & Sarrazin, F. Heterogeneous reaction with solid catalyst in droplet-flow millifluidic device. *Chem. Eng. J.* **227,** 97–102 (2013).

35.   Sai Krishna, K. *et al.* Millifluidics for Time-resolved Mapping of the Growth of Gold Nanostructures. *J. Am. Chem. Soc.* **135,** 5450–5456 (2013).

36.   Romano, M., Pradere, C., Toutain, J., Hany, C. & Batsale, J. C. Quantitative thermal analysis of heat transfer in liquid–liquid biphasic millifluidic droplet flows. *Quant. Infrared Thermogr. J.* **11,** 134–160 (2014).

37.   Wang, W. S. & Vanapalli, S. A. Millifluidics as a simple tool to optimize droplet networks: Case study on drop traffic in a bifurcated loop. *Biomicrofluidics* **8,** 064111 (2014).

38.   Boitard, L., Cottinet, D., Bremond, N., Baudry, J. & Bibette, J. Growing microbes in millifluidic droplets. *Eng. Life Sci.* **15,** 318–326 (2015).

39.   Feuerborn, A., Prastowo, A., Cook, P. & Walsh, E. Merging drops in a

Teflon tube, and transferring fluid between them, illustrated by protein crystallization and drug screening. *Lab Chip* **15,** 3766–3775 (2015).

40. Martinez de Banos, M. L., Carrier, O., Bouriat, P. & Broseta, D. Droplet-based millifluidics as a new tool to investigate hydrate crystallization: Insights into the memory effect. *Chem. Eng. Sci.* **123,** 564–572 (2015).

41. Lalanne-Aulet, D. *et al.* Multiscale study of bacterial growth: Experiments and model to understand the impact of gas exchange on global growth. *Phys. Rev. E* **92,** 52706 (2015).

42. Perez, M. *et al.* Development of a new passive sampler based on diffusive milligel beads for copper analysis in water. *Anal. Chim. Acta* **890,** 117–123 (2015).

43. Li, Z., Mak, S. Y., Sauret, A. & Shum, H. C. Syringe-pump-induced fluctuation in all-aqueous microfluidic system implications for flow rate accuracy. *Lab Chip* **14,** 744 (2014).

44. Garstecki, P., Fuerstman, M. J., Stone, H. A. & Whitesides, G. M. Formation of droplets and bubbles in a microfluidic T-junction-scaling and mechanism of break-up. *Lab Chip* **6,** 437–46 (2006).

Chapter 4. Probing the effect of cationic polymers on the stability of dilute crude-oil-in-water emulsions using microliter droplet reactors

4.1. Introduction

Emulsions and foams appear in applications as diverse as cosmetics, foods, coatings, adhesives, and pharmaceuticals. The objective in many of these applications is to generate extremely stable emulsions, which preserve the shelf life of encapsulated products, maintain the texture of foods, or ensure uniform distribution of an active ingredient. However, in some contexts the ability to rapidly destabilize emulsions is equally important. For example, in latex paints a dispersion of polymer and pigment particles must remain stable for transport and storage, but during application it is desirable for the dispersed phases to coalesce, forming a uniform film. Coalescence is achieved through solvent evaporation after paint application. In other cases, emulsions are generated as an unwanted byproduct of a high shear industrial process, or form naturally as a consequence of environmental conditions. In the recovery and processing of crude oil, emulsions of oil and water appear at the point of extraction or are formed during downstream processing and transport[1–4]. Large quantities of water occur naturally in oil bearing formations[5,6], or are added during secondary or tertiary oil recovery operations, for example in polymer flooding[7] or surfactant enhanced oil recovery[8].

In these applications, the fraction of water present in the crude oil can vary over the life of the well, from well to well, from reservoir to reservoir, and with the depth of the well, often exceeding 98%[9–11]. The emulsions may be oil-in-water, water-in-oil, or multiple emulsions. Extremely dilute oil-in-water

emulsions are also produced as a byproduct of demulsifying a more concentrated crude-oil-in-water suspension. The water fraction present in crude oil creates problems for downstream processing and refining operations, including increased transportation costs and corrosion[12]. Regulatory requirements place constraints on the oil content in waste water discharged from oil and gas recovery operations[5,13]. It is environmentally and economically beneficial to remove as much water as possible from the crude oil and vice versa[14].

In this work we focus on very dilute crude-oil-in-water emulsions where the water content exceeds 98% (w/w). Many mechanical separation techniques exist to clarify dilute oil-in-water suspensions[5]. Polyelectrolyte water clarifiers are often added in combination with these methods to improve separation efficacy and speed[15]. These methods are generally effective, but the physio-chemical properties of the produced emulsion vary dramatically and unpredictably from well to well and field to field, and as a function of time[11,16]. Often, clarifiers that are initially very effective lose efficacy over time. It is currently impossible to predict the best clarifier mixtures for a given produced emulsion. Clarifier selection is accomplished empirically with bottle tests[17]. Samples of the produced emulsion are drawn from the wellhead and mixed in transparent 'prescription bottles' with different clarifiers. Performance of the clarifier is evaluated based on the visual appearance of the emulsion, including the turbidity, and the formation and the structure of the oil cream layer (rag layer). Tests are performed in the field since aging of the produced emulsion during transport may modify its properties[18,19].

The effect of water clarifiers on dilute oil-in-water emulsions is often non-monotonic with concentration; over treatment with additive can lead to resuspension of the oil. Bottle tests are time consuming and typically only test one or two concentrations of several different clarifier candidates, providing an incomplete picture of performance. The fundamental relationship between the properties of the produced emulsion and the efficacy of a given clarifier is poorly understood. There are few tools available to quickly and quantitatively evaluate clarifier performance with high compositional resolution; such capability would be extremely valuable to screen clarifiers more efficiently and to improve fundamental understanding.

Microfluidic droplet-based techniques allow for precise control and manipulation of small fluid volumes in ways that are often impossible or impractical at bulk scales[20,21]. These small-scale fluid handling techniques provide exceptional control over transport of mass, momentum, and energy[22,23]. Practically, this leads to precise control of mixing, shear stresses, chemical reactions, diffusion rates, and particle position and distribution within the fluid. Additional benefits include the potential for high throughput screening, automated fluid handling, and reduced sample consumption for testing small quantities of new, hazardous, or toxic materials. Droplet based techniques encapsulate samples in nano- and microliter scale droplets, which act as isolated vessels that are surrounded by an inert medium and can be easily manipulated[24]. The contents of the compartments can be varied from vessel to vessel reproducibly and with high precision.

Here, we apply droplet based processing strategies to examine the effects of various additives on the stability of dilute emulsions of crude oil in water. A millimeter-scale apparatus is designed and built using off-the-shelf fittings, tubing, and components[25], rather than traditional high resolution soft lithography using polydimethylsiloxane or etching of glass devices. Optical methods, including microscopy and visible light absorption spectroscopy, are used to quantify the stability of the emulsion. The larger length scale (millimeter rather than micron) provides a longer optical path length while taking advantage of the facile droplet production in laminar flows. The dilute crude-oil-in-water emulsion is first generated via bulk-scale homogenization, and then a droplet of the produced emulsion is formed in an inert perfluorocarbon continuous phase fluid by injection into a droplet generating nozzle in the so-called millifluidic device[26]. The droplet compartments contain an emulsion of crude oil droplets that are 1 to 10 μm in size. Cationic polyelectrolytes, salts, and water are added to the emulsion compartments at varying concentration.

4.2.   Materials and Methods

To obtain better experimental reproducibility, and to partially mitigate the effects of aging and transport on the produced emulsion, a fresh "synthetic" produced emulsion is prepared for each experiment. The emulsion is prepared by combining 99 g of deionized water (18.1 M-ohm, Barnstead) with 80 μL of 1 N sodium hydroxide (Fisher) in a 120 mL glass container to achieve a pH of 10.75. Next, the tip of a homogenizer (Ultra-Turrax T25, Janke & Kunkle) is immersed in the solution to a specific depth several centimeters below the surface. A syringe

(3 mL solvent compatible, Norm-Ject, HSW) is used to inject 1 mL of crude oil (Texas crude oil, rawcrudeoil.com) under the surface of the water while the homogenizer is operating at approximately 8000 rpm. The mixture is homogenized for 90 s. This procedure generates a 1 % (v/w) crude-oil-in-water emulsion.

To further characterize the dispersion, the particle size distribution and electrophoretic mobility of the synthetic produced emulsion are measured. A laser diffraction particle size analyzer (LS 13 320, Beckman Coulter) is used to collect particle size distribution data for the crude-oil-in-water emulsion. An emulsion is prepared as previously described and a disposable pipette is used to obtain several milliliters of sample from the center of the dispersion, well below the air water interface, in order to avoid collecting larger oil droplets that rapidly cream. Measurements are made multiple times from the same emulsion over the course of several hours. The electrophoretic mobility of the emulsified oil droplets in water is measured using a ZetaSizer (Nano ZS, Malvern). The material properties of the oil are assumed to be: viscosity, η_o = 100 mPa·s, refractive index, n_o = 1.4974, and dielectric constant, ε_o = 2, based on tabulated data and internal measurements by The Dow Chemical Company.

Three water clarifiers, which are cationic polymers denoted Polymer A (M_w = 330 kg/mol, M_n = 201 kg/mol), Polymer B (M_w = 599 kg/mol, M_n = 276 kg/mol) and Polymer C (M_w = 864 kg/mol, M_n = 635 kg/mol), are obtained from The Dow Chemical Company and used as received. Sodium chloride and

calcium chloride of analytical grade were obtained from Sigma Aldrich and used as received.

For the microscale experiments a millifluidic co-flow type droplet generator[27] is constructed using off-the-shelf tubing (Cole Parmer) and commercial chromatography fittings (IDEX Scientific and VICI Valco). The method of operation of the apparatus is described in more detail in the Results section. Briefly, one end of a three-way barbed fitting (30703-71, Cole-Parmer) is attached to a section of polytetrafluoroethylene (PTFE) tubing (06606-52, Cole-Parmer). A 40 mm section of polyetheretherketone (PEEK) tubing (1532, IDEX Scientific) is inserted into the opposite end of the three-way barbed fitting such that it is concentric with the first section of tubing. This configuration forms a co-flowing type droplet generator. A four way polychlorotrifluoroethene (PCTFE) cross (CXKF, VICI Valco) is joined to the PEEK tubing to allow three different droplet phase fluids, water, polymers or salts, and the synthetic produced emulsion to be combined upstream of the location of the droplet generation. Small sections of silicone tubing (96400-13, Cole-Parmer) or vinyl tubing (06407-71 and 06407-73, Cole Parmer) are used as sleeves to obtain water-tight connections between various components. Syringes (3 mL solvent compatible, Norm-Ject, HSW) are joined to PTFE tubing (06417-41, Cole-Parmer) using Luer lock adapters and compressions fittings (XP-235, IDEX Scientific). The PTFE tubing is joined to the four-way CTFE fitting using compression nuts (VICI Valco). 18 gauge PTFE tubing (06417-41, Cole-Parmer) is used to store the droplets after generation and deliver them downstream. The continuous phase carrier fluid is an

inert perfluorocarbon fluid (HR2-797, Hampton Research) that is immiscible with both the water and the crude oil. Computer controlled syringe pumps (PHD 2000, Harvard Apparatus) deliver fluids volumetrically.

Optical detection of the droplet compartments generated in the apparatus described above is accomplished through microscopy and transmitted visible light spectroscopy. A stereoscopic microscope (SMZ-10, Nikon) with magnification set to 0.66X is mounted to a base with a light source operating in dark field illumination mode. A digital camera (EOS Rebel XS, Canon) is mounted to the microscope and connected to a PC for remote triggering. Images of the droplet compartments are captured every 10 s as they flow through the field of view over the course of each experiment. A spectrophotometer (QE-65000 with Ocean View software version 1.50, Ocean Optics), shutter (Inline-TTL-S, Ocean Optics) and optical fibers (QP600-2-UV-Vis, Ocean Optics and 400/430/730 0.37 NA, RoMack Inc) are used to measure the optical extinction at a wavelength of 500 nm. The optical fibers are aligned 180 degrees to each other and centered on a section of 18 gauge PTFE tubing, located 430 mm downstream from the droplet generator, using a cross-type fitting (Cole-Parmer) to rigidly align the optical fibers and the tubing. Illumination for spectroscopy is provided by a tungsten-halogen light source (ISP-REF Integrating Sphere, Ocean Optics). The light source and the spectrophotometer are allowed to thermally equilibrate for at least 45 minutes prior to data collection.

4.3. Results

Macroscale Experiments

Before performing experiments in the millifluidic platform, macroscale experiments are conducted in order to obtain a baseline for the behavior of the synthetic produced emulsion and the performance of the clarifier candidates. Polyelectrolytes are often selected as water clarifiers[28], and it is well known that charge plays an important role in emulsion stability. Additionally, the water contained in produced emulsions, produced brine, is often of high salinity which influences the conformation of the charged polymers as well as the thickness of the electric double layer associated with the emulsion droplets. The efficacy of salts in suppressing emulsion formation and in destabilizing previously-formed emulsions suggests that charge is an important stabilizing mechanism in the synthetic produced emulsion.
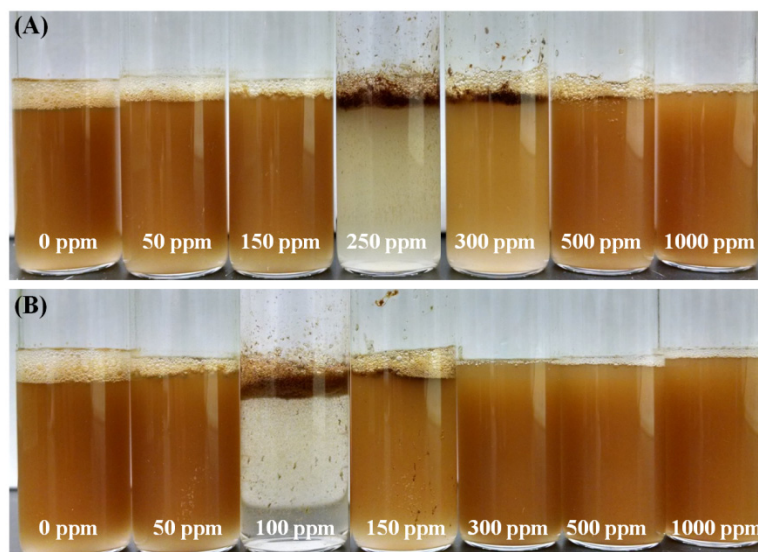
Figure 4.1. A series of images demonstrating the effect of increasing concentration of cationic polymer on the stability of an emulsion consisting of 1 % (v/w) crude oil in water. **(A)** Polymer A demonstrates effective separation of the oil-in-water emulsion at a polymer concentration of 250 ppm. **(B)** Polymer C demonstrates effective separation at 100 ppm. Both polymers are ineffective at high and low polymer concentration. The images are a composites of several separate bottle tests. The images were collected between 1 and 30 min after the addition of the clarifier.

Figure 4.1 shows the effect of cationic polymer concentration on the structure and stability of a dilute crude-oil-in-water emulsion. Each vial contains a synthetic produced emulsion of 1 % (v/w) crude oil in water to which a fixed quantity of a single cationic polymer is added. The left most vial in each set of images contains no polymer. The vials in Figure 4.1 (A) have been treated with Polymer A at concentrations from 50 to 1000 ppm. No effect on emulsion stability is observed at low treatment levels (50 and 100 ppm) or at high treatment levels (500 and 1000 ppm). At polymer concentrations of 250 and 300 ppm, the turbidity of the emulsion and the structure of the air-water interfacial layer changes. The foam is replaced by a dark, oil-rich layer at the free surface. Figure 4.1 (B) shows the effect of treatment with Polymer C at concentrations from 50 to

1000 ppm. Similar to Polymer A, Polymer C shows no effect on emulsion stability at low treatment levels (50 ppm) or high treatment levels (300, 500, and 1000 ppm); however the most effective concentration of Polymer C is lower than that of Polymer A. A pronounced reduction of emulsion turbidity and the formation of a dark, oil-dense rag layer are observed at 100 ppm and to a lesser extend at 150 ppm.

Both polymers are effective at destabilizing the emulsion at an intermediate concentration. Polymer C is effective at a concentration 150 ppm lower than the effective concentration of Polymer A. The transition between good performance and poor performance is sharp, and the compositional effects observed in Figure 4.1 illustrate the commonly observed non-monotonic effects of polyelectrolyte water clarifiers, including under-treatment at low polymer concentration, ideal treatment, and over-treatment at high polymer concentration leading to subsequent restabilization of the emulsion. The narrow window of performance shown in Figure 4.1 emphasizes the challenge in selecting the appropriate concentration of a clarifying agent, and provides a baseline for the performance of the synthetic produced emulsion investigated in this work. The results of Figure 4.1 will be used to compare with the results obtained in the millifluidic platform.
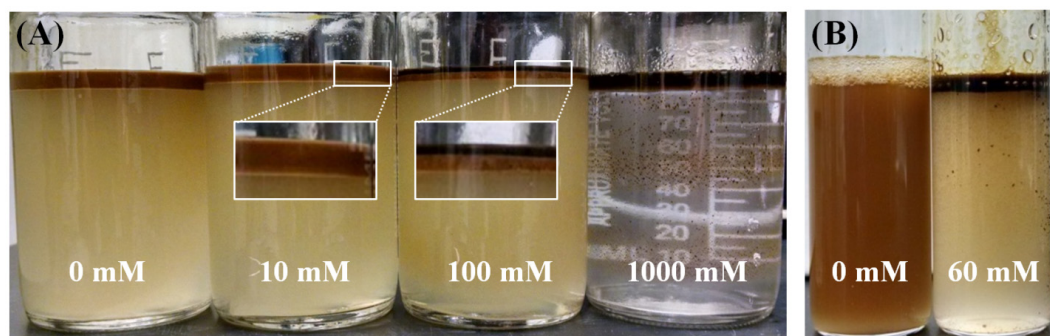
Figure 4.2. A series of images demonstrating the effect of salt concentration on the preparation and subsequent stability of a crude-oil-in-water emulsion. **(A)** Four separate emulsions were prepared with 1 % (v/w) crude oil in water with the indicated concentration of sodium chloride and allowed to settle for 30 minutes. Salt is added prior to homogenization of the oil. **(B)** The effect of calcium chloride on the emulsion stability when added after homogenization of the oil.

Produced emulsions possess varying degrees of salinity. The presence and concentration of ionic species is known to have a profound effect on emulsion formation and stability[29]. Figure 4.2 contains two image sets comparing the effect of two different salts on the formation and subsequent stability of the synthetic 'produced emulsion.' Figure 4.2 (A) depicts a series of emulsions that are generated with various concentrations of sodium chloride added prior to homogenization. The image is captured approximately 30 min after homogenization. With 10 mM added sodium chloride, there is no observable difference in the overall turbidity of the emulsion or the structure of the creaming layer as compared with the salt free case. With 100 mM added sodium chloride, the overall turbidity of the emulsion remains unchanged, but the structure of the oil-rich cream layer consists of a darker upper layer and a lighter lower layer (Figure 4.1(A) insets). With 1000 mM of added sodium chloride, the formation of an emulsion is not observed. Instead, immediately after homogenization a continuous layer of crude oil settles to the top of the aqueous phase. Figure 4.2

(B) shows that 60 mM calcium chloride added after homogenization is also effective at reducing the overall turbidity of the dilute crude-oil-in-water emulsion, and creating an oil-rich creamed layer. In a separate experiment, the electrophoretic mobility of the oil droplets is measured and found to be $\mu = -7.33$ µm/s·V/cm, suggesting that the oil droplets possess a negative zeta potential.
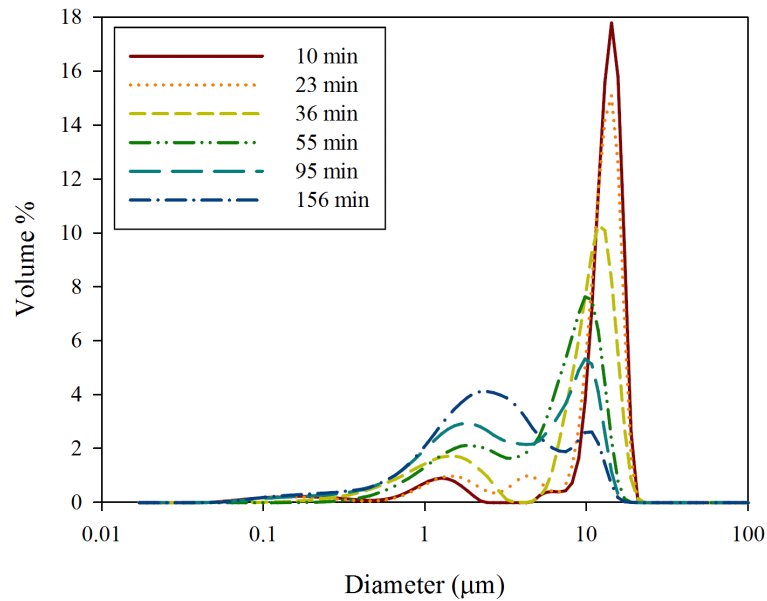
Figure 4.3. Particle size distribution as a function of settling time for an emulsion containing 1 % (v/w) crude oil in water with no added salt or clarifier. Each line corresponds to the particle size distribution of a sample of the emulsion collected from the same height within the dispersion, but at an elapsed time after homogenization as indicated in the legend.

Bulk methods of homogenization generate polydisperse emulsions containing a distribution of droplet sizes. Figure 4.3 shows the particle size distribution measured in the 1 % (v/w) crude-oil-in-water synthetic produced emulsion at various settling times and in the absence of added salt or clarifier. At each time point after homogenization, as indicated in the legend, a sample is drawn from a fixed height within the dispersion and the size distribution is

measured as described in Materials and Methods. Initially, the distribution is dominated by oil droplets with a diameter of approximately 10 - 20 μm. As time passes, the size distribution changes. The volume fraction of particles with a diameter of the order of 10 μm decreases, while the volume fraction of particles with diameter of the order of 1 μm increases, and the distribution broadens. Creaming was observed in the synthetic produced emulsion prior to the first size distribution measurement at 10 min. The largest droplets (>20 μm) were not captured by the distributions shown in Figure 4.3.

The data in Figure 4.3 shows that the synthetic produced emulsion is relatively unstable even in the absence of the polymeric clarifiers or added salts. The changes in the particle size distribution arise from the combined effects of flocculation, creaming, Ostwald ripening, and coalescence[29]. These mechanisms cannot be decoupled based solely on the data provided in Figure 4.3, but observed changes in the size distribution still provide meaningful information. First, the elapsed time between the homogenization of the crude oil and the addition of clarifier is important, since the properties of the emulsion change with time. Second, if sufficient time has elapsed, and an aliquot of the emulsion is drawn from within the bulk of the dispersion, the volume fraction of crude oil in the sample will be smaller than the fraction initially added, since some fraction of the emulsified crude oil has creamed to the top layer of the bulk dispersion.

Millifluidic Experiments

Droplet-based microfluidic techniques provide a method for rapidly generating fluid droplets or 'compartments' of defined volume and composition,

including compartments containing multiple, partially or completely immiscible phases. Here we describe the method of operation of a millifluidic platform to probe the stability of the synthetic produced emulsion with and without additives. The physical construction of the apparatus is described in Materials and Methods.
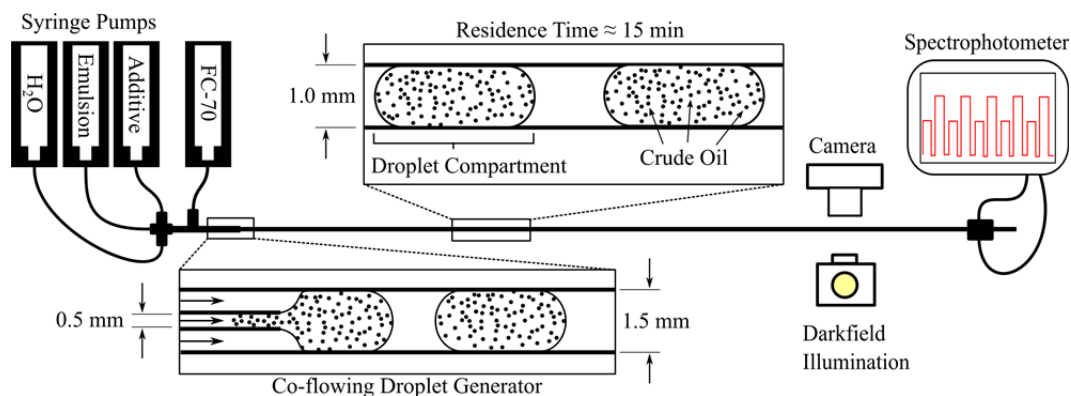
Figure 4.4. A schematic diagram of the droplet-based platform used to generate and optically interrogate the emulsion compartments. Four computer controlled syringe pumps (top left) deliver fluid to a coflowing droplet generator that produces monodisperse 6 μL droplet compartments suspended in an inert, immiscible carrier phase fluid composed of a perfluorocarbon fluid. The aqueous compartments, containing polymers, salts, and a crude-oil-in-water emulsion, travel downstream for approximately 900 s until they reach a detector. Images of the compartments and their optical transmittance at 500 nm are collected at a fixed location downstream as a function of time.

After generation of the synthetic produced emulsion *via* bulk scale homogenization, 3 mL of the resulting suspension is drawn into a disposable syringe and placed in a syringe pump. Fluidic connections are made between the syringe and the millifluidic platform *via* PTFE tubing. A schematic diagram of the millifluidic platform is provided in Figure 4.4. Three syringe pumps operating in parallel separately deliver the crude-oil-in-water emulsion, distilled water, and any additives (clarifiers or salt) to a four-way PEEK fitting where the three fluid streams merge. The outlet of the four-way fitting is connected to the coflowing

90

droplet generator with a 40 mm length of PEEK tubing. The PEEK tubing serves as the nozzle for the droplet phase fluid in the coflowing junction. The continuous phase fluid, a perfluorocarbon, is delivered by a fourth syringe pump and enters the outer capillary of the droplet generator surrounding the PEEK nozzle. Monodisperse 6 μL droplets are produced through a squeezing mechanism[30], and flow downstream into a length of approximately 430 mm of PTFE tubing (1.07 mm inner diameter). Droplets are produced continuously as a function of time, forming a train of equally spaced droplets. The flow rate of the emulsion is kept constant while the flow rates of the pure water and the additive streams are varied such that the crude oil concentration within each droplet compartment is identical, but the concentration of additives is varied monotonically from droplet to droplet by varying the speeds on the independently controlled pumps. The total volumetric flow rate of the droplet phase fluid is 30 μL/min and the volumetric flow rate of the perfluorocarbon continuous phase fluid is 15 μL/min. For droplet based experiments in the millifluidic platform the synthetic crude oil emulsion preparation procedure previously described is modified to generate a 2 % (v/w) emulsion, which is diluted by one half in the apparatus to a final effective concentration of 1 % (v/v) in the droplets, in order to most closely match the crude oil composition in the macroscale experiments.
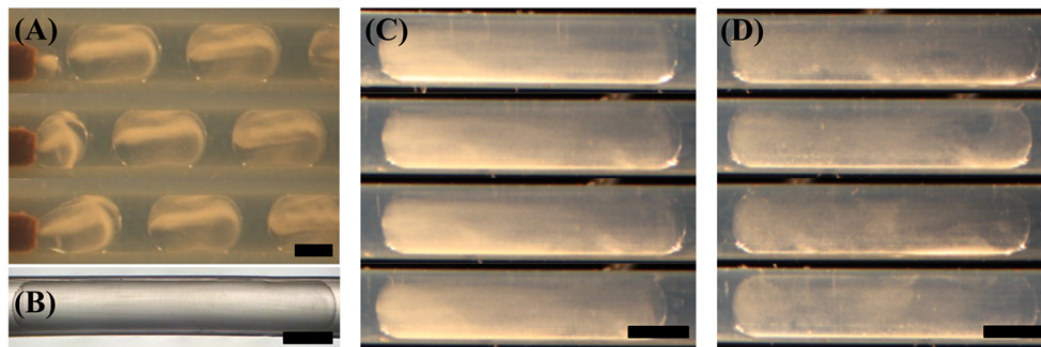
Figure 4.5. Micrographs of droplet compartments containing synthetic produced emulsion as they appear in the droplet-based fluid handling platform. The images are captured using darkfield illumination, which causes micron scale crude oil droplets contained within the parent droplet compartment to scatter light and appear bright compared with the background. **(A)** A time sequence of images of compartment production in the coflowing droplet generator. **(B)** An image of an untreated droplet compartment with brightfield illumination for comparison. **(C)** Representative images of untreated droplet compartments containing no additives. **(D)** Representative images of droplet compartments treated with approximately 200 ppm of Polymer A. The scale bars are 1 mm. In all four sets of images the droplets contain approximately 1 % (v/w) of emulsified crude oil.

Figure 4.5 shows four sets of images of the microliter droplet compartments as they appear in the PTFE tubing in the millifluidic platform. The droplet compartments in each image contain 1 % (v/w) crude oil that was emulsified off-chip and injected into the droplet generator as described previously. Figures 4.5 (A), (C), and (D) are captured with darkfield illumination, causing the regions containing tiny crude oil emulsion drops to appear white against a dark background. Figure 4.5 (A) is a time sequence of images showing droplet production. The aqueous droplet phase fluid containing the synthetic produced emulsion enters from the left and is advected to the right by the continuous phase fluid. The droplet compartment is formed from the three incoming streams delivered by the syringe pumps as depicted in Figure 4.4. The elapsed time between each image (top to bottom) is approximately 10 seconds. In

Figure 4.5 (B) the droplet is imaged with brightfield illumination. The structure of the emulsion is not visible since the transmitted light is not scattered sufficiently by the small oil droplets relative to the background light intensity. Figure 4.5 (C) shows four sequential droplets of identical composition that have traveled approximately 430 mm downstream of the droplet generator in an elapsed time of approximately 900 seconds. The droplets contain 1 % (v/w) of emulsified crude oil in water with no additives. Figure 4.5 (D) shows four sequential droplets at the same downstream position as in (C), and containing the same concentration of crude oil emulsion, but treated with approximately 180 – 200 ppm of clarifier (Polymer A) added to each droplet compartment *via* the incoming fluid streams as described in Figure 4.4.

Figure 4.5 shows that the millifluidic platform is capable of generating droplet compartments in a perfluorocarbon continuous phase fluid, in which the droplets contain an emulsion of a third immiscible phase fluid, crude oil, without unwanted wetting of the droplets to the walls of the device. The images also provide visual information about the distribution and mixing of the components inside the droplet compartments. Significant visual changes in the microstructure of the emulsion contained in each compartment can be seen in response to the presence or absence of the cationic polymer. We also observe evidence of mixing during droplet production, through "twirling" effects[31,32] that occur during pinch off of the droplet from the PEEK nozzle, and additional mixing as the droplet is forced to elongate and accelerate into the downstream tubing, which has a smaller inner diameter than the upstream capillary. Mixing is also evident in the change in

structure of the emulsion inside the compartments in the freshly generated droplets shown in Figure 4.5 (A) compared with that of the droplets in Figure 4.5 (C) that have traveled a significant distance downstream. Mixing during droplet formation has been characterized previously[24], and occurs as the droplet travels downstream primarily as a result of recirculating flows established within the droplet from viscous interactions between the droplet, the continuous phase fluid, and the walls of the tubing[33–35]. In addition to convective mixing, diffusion of the clarifier across the droplet compartment occurs during the 900 seconds that the droplets travel downstream[36].

In addition to taking micrographs of the droplet compartments, the millifluidic platform samples the optical transmittance of the compartments by measuring the change in the intensity of the light passing transversely through the droplets. The reduction in transmittance light across the droplet is due to a combination of optical absorption due to the highly absorbing crude oil, and light scattering due to the micron and submicron size of the crude oil droplets. This provides quantitative information regarding the microstructure of the crude-oil-in-water emulsion inside of each aqueous compartment. The relative contributions of the two mechanisms are not critical to our analysis so we make no attempt to deconvolute the contributions of absorption and scatter, rather we report their combined effects as extinction,

$$Extinction = \log_{10} \frac{I_o}{I}, \qquad\qquad (4.1)$$

where *I* is the intensity of the light exiting the droplet and I_o is the intensity of light entering the droplet.
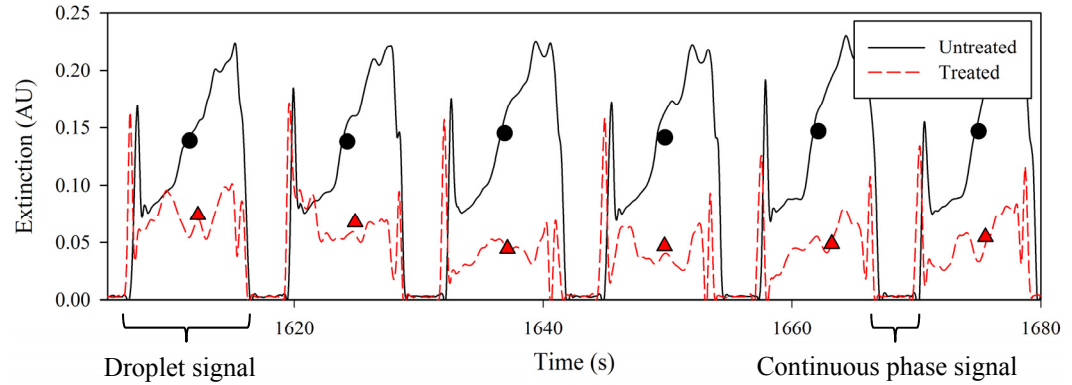
Figure 4.6. Measured Extinction at a fixed position 430 mm downstream of the droplet generator as a function of time for two sets of droplet compartments each containing 1 % (v/w) crude oil in water. The extinction traces have been shifted horizontally for easier comparison. The solid black line (untreated) corresponds to the extinction signal of droplets that contain only the oil-in-water emulsion. The dotted red line (treated) corresponds to droplets that contain approximately 180 - 200 ppm of Polymer A in addition to the crude oil emulsion. The black circles correspond to the time-averaged extinction of each untreated droplet, and the red triangles correspond to the time-averaged extinction of each treated droplet.

Figure 4.6 is a graph of the optical extinction as a function of time at a fixed wavelength of 500 nm as measured by the in-line spectrophotometer located 430 mm downstream of the droplet generator. As the droplets flow past the detector a signal is generated as a function of time corresponding to either the droplet compartments or the continuous phase fluid spacers between each droplet. The integration time of the spectrophotometer is set to 25 ms and 10 consecutive measurements are automatically averaged to obtain one reported extinction reading. A total of 30 separate extinction readings are recorded for each droplet compartment as it flows past the detector, resulting in an extinction profile resolved along the length of each compartment. The continuous phase fluid is chosen as the reference spectrum such that the extinction of the fluid spacers is set

95

equal to zero. The graph is composed of two data sets: the solid black line corresponds to the extinction signal associated with the series of untreated droplet compartments depicted in Figure 4.5 (B), and the dashed red line corresponds to a series of droplets treated with approximately 180 – 200 ppm of Polymer A, depicted in Figure 4.5 (C). For easier comparison the traces have been shifted horizontally so that the signals corresponding to the droplet compartments overlap. The black circles and red triangles correspond to the time-averaged extinction of the droplet signal for the untreated and treated droplets, respectively. For the untreated droplets, the extinction is non-uniform, increasing significantly along the length of the droplets, from approximately 0.07 to 0.23 A.U., corresponding to an average extinction of approximately 0.14 A.U. For the treated droplets, the overall extinction is lower, varying between approximately 0.02 and 0.07 A.U., corresponding to a significantly lower average extinction of between 0.05 and 0.07 A.U. Additionally, for the treated droplets the extinction is more uniform as a function of position along the length of the droplet.

The extinction traces shown in Figure 4.6 quantify the differences in turbidity and produced emulsion structure that can be seen visually in the micrographs of Figures 4.5 (B) and (C). The average extinction and the distribution of the crude-oil-in-water emulsion contained in each compartment varies dramatically for the treated and untreated droplets. This suggests that the time averaged extinction of the droplet compartments can be used as a metric to evaluate the effect of clarifiers on produced emulsions. The difference in the

shape of the extinction profile may also provide additional information about the microstructure of the emulsion.
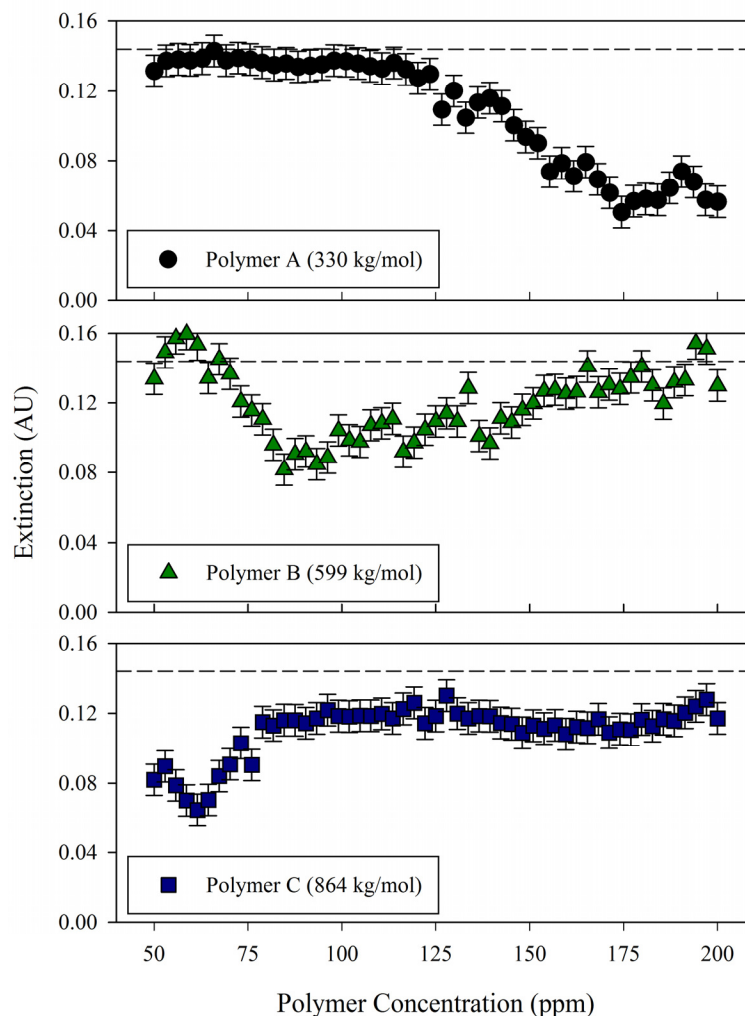
Figure 4.7. Average optical extinction plotted as a function of the corresponding polymer concentration of each droplet compartment for three separate experiments. The dashed horizontal lines correspond to the average extinction of untreated droplets. The error bars represent the standard deviation in the average extinction values for a population of untreated droplets. The data points are calculated from the average of two replications of the experiment.

To evaluate the efficacy of the average droplet compartment extinction as a metric for emulsion stability, droplet based experiments were performed with the clarifiers used in Figure 4.1. Figure 4.7 plots the time-averaged extinction as a

function of the corresponding polymer concentration for a series of microliter droplet compartments containing 1 % (v/w) emulsified crude oil in water treated with varying concentrations of three polyelectrolyte-based water clarifiers. The black filled circles correspond to droplets that have been treated with Polymer A, the green triangles to droplets treated with Polymer B, and the blue squares to droplets treated with Polymer C. In each experiment the added polymer concentration varies linearly along the train of droplet compartments from 50 to 200 ppm. The dashed horizontal line in each plot corresponds to the average of the extinction of approximately 50 untreated droplet compartments (0.14 A.U.) containing the same crude oil emulsion but without added clarifier. For Polymer A, the extinction remains approximately constant and equal to the untreated baseline for concentrations between 50 and 125 ppm. For higher concentrations the extinction decreases to a minimum near 175 – 200 ppm. Polymer B exhibits an extinction minimum at about 60 ppm, followed by a rapid increase. The extinction levels off between 80 and 200 ppm. In this range the extinction approaches but does not become equal to the untreated baseline value. Polymer C shows an extinction minimum at about 80 ppm, followed by a gradual increase in extinction, reaching the baseline value at approximately 175 ppm. For each of the three polymers, the data presented corresponds to the average of two experiments. The error bars represent the standard deviation of the average extinction of 50 identical, untreated emulsion compartments.

Figure 4.7 demonstrates the ability of the droplet-based platform to measure dosage-dependent effects on the optical properties of the synthetic

produced emulsion. The concentration of clarifier required to change the extinction of the produced emulsion for Polymer A and Polymer C agrees with the qualitative observations in macroscale tests at the same experimental conditions. However, the effect is shifted to concentrations approximately 100 ppm lower in the microliter droplet compartments compared with the macroscale tests. Figure 4.7 also shows that the concentration of cationic polymer required to achieve a minimum extinction level decreases with increasing polymer molecular weight.
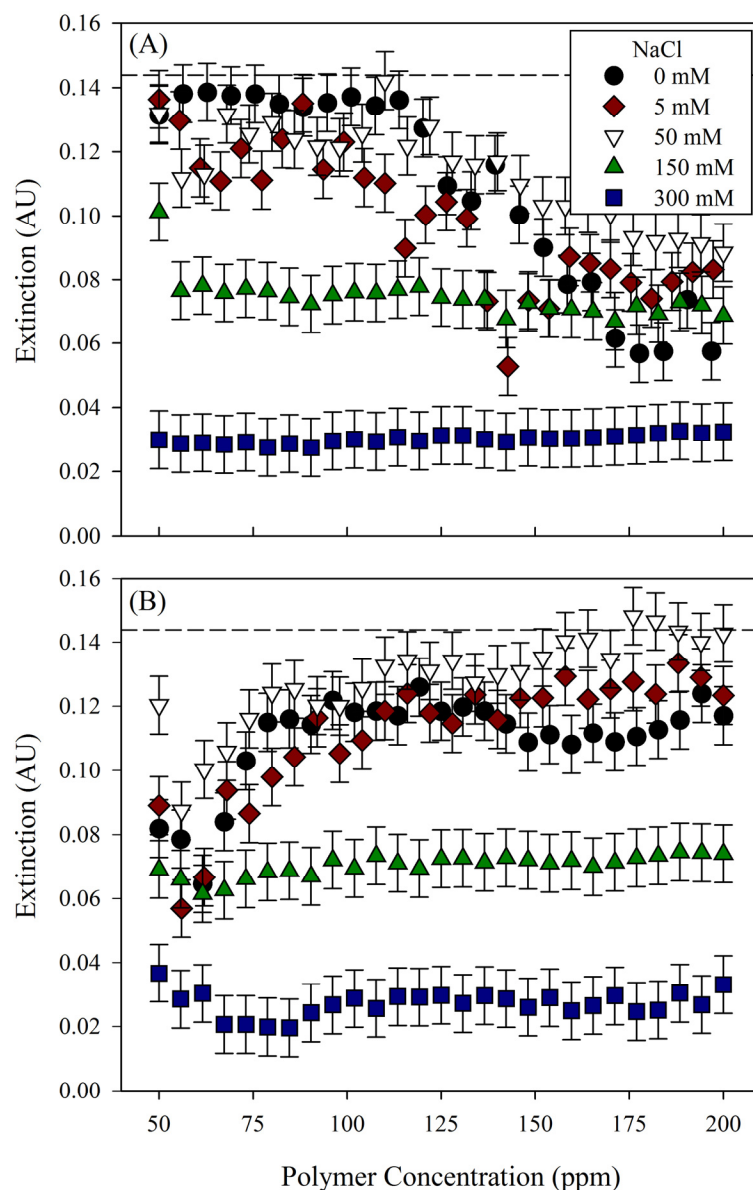
Figure 4.8. Average optical extinction as a function of the corresponding polymer concentration of each droplet compartment for 10 separate experiments corresponding to different combinations of sodium chloride with **(A)** Polymer A and **(B)** Polymer C. Each set of symbols corresponds to a separate experiment at a fixed sodium chloride concentration. The extinction is measured as a function of polymer concentration, which varies from droplet to droplet (point to point). For each experiment a fresh emulsion is prepared and salt is added during bulk homogenization. The error bars are obtained from the standard deviation on the average extinction for untreated droplets. The legend indicates the sodium chloride concentration for both plots.

Figure 4.8 compares the efficacy of Polymer A and Polymer C on the

treatment of the synthetic produced emulsion with varying levels of salinity. The

average extinction of an emulsion-containing compartment is plotted as a function of the corresponding concentration of added polymer in that droplet compartment. Each set of symbols corresponds to a different concentration of sodium chloride added to the crude oil and water mixture prior to homogenization. Figure 4.8 (A) shows the effect of salinity on the performance of Polymer A and Figure 4.8 (B) shows the effect of salinity on the performance of Polymer C. In both cases, the black filled circles correspond to the salt-free case, also plotted in Figure 4.7. The salt concentrations listed in the legend correspond to the effective concentration in the entire droplet compartment. Each compartment contains one half of the salt concentration of the original emulsion, because the emulsion is diluted by a factor of two in the millifluidic platform due to the addition of the water and additive streams.

Effective salinities of 5 mM (red diamonds) and 50 mM (open inverted triangles) show similar extinction to the salt free case at low concentrations of added polymer. Emulsions generated with either 150 or 300 mM of sodium chloride exhibit lower extinction values that are nearly independent of polymer concentration. At an effective concentration of 300 mM of added salt (600 mM in the parent emulsion), the crude oil separates almost immediately after homogenization, so the extinction of the blue squares is approximately equal to the extinction of the oil free compartments containing only polymer, water, and water soluble fractions of the raw crude oil. Figure 4.8 (B) shows the effect of emulsion salinity on the performance of Polymer C. Similar to Polymer A, 5 and 50 mM added sodium chloride have no significant effect on the extinction of the

droplet compartments as clarifier concentration varies. At 150 and 300 mM sodium chloride, the extinction is lower and nearly independent of polymer concentration, exhibiting a value equal to the oil free extinction at 300 mM sodium chloride.

The results presented in Figure 4.8 suggest that small concentrations of sodium chloride have no significant effect on clarifier performance, while high concentrations of sodium chloride suppress the formation of the produced emulsion for the crude oil system investigated here.
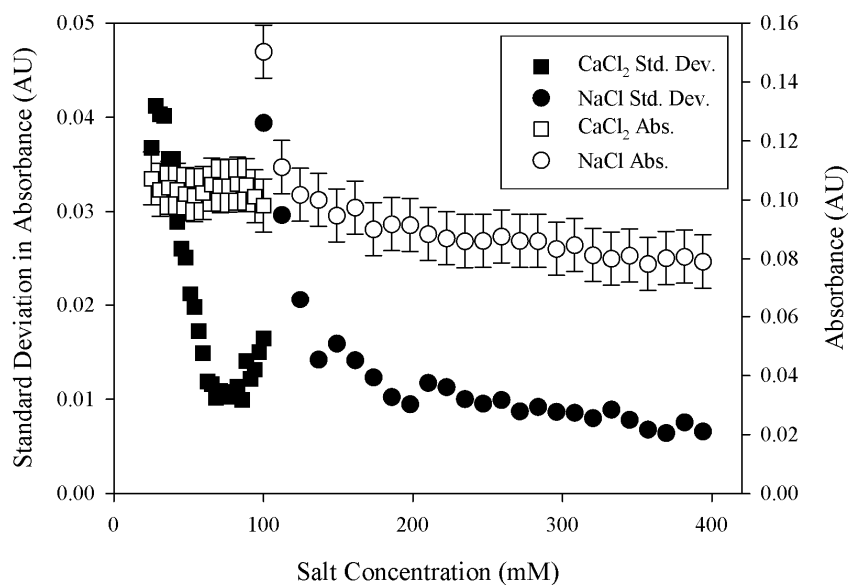
Figure 4.9. A graph of the time averaged extinction of a single droplet compartment and the standard deviation of the extinction of a single droplet compartment containing 1 % (v/w) crude oil emulsion as a function of added salt concentration for calcium chloride (squares) or sodium chloride (circles). The open symbols correspond to the average extinction plotted on the right vertical axis. The filled symbols correspond to the standard deviation in extinction plotted on the left vertical axis.

Salinity of the synthetic produced emulsion is also important to emulsion stability, even in the absence of added polymers. Figure 4.9 plots the average extinction and the standard deviation of the average extinction for two sets of

experiments, one using calcium chloride, and one using sodium chloride, both of which are added to the emulsion compartments in the millifluidic platform, rather than being added prior to homogenization of the crude oil. The filled symbols correspond to the standard deviation on the extinction measurements associated with each droplet compartment, plotted as a function of the corresponding salt concentration within each compartment. The open symbols correspond to the average extinction of the droplet compartments. For calcium chloride (squares) the average extinction is equal to approximately 0.10 A.U. and is independent of concentration between 25 to 100 mM. However, the standard deviation on the extinction decreases by a factor of four, from 0.04 to 0.01 A.U. for salt concentrations between 25 to 75 mM, and then increases to 0.016 A.U. at 100 mM. For sodium chloride (circles), the average extinction decreases rapidly between the first two droplet compartments, from 0.15 to 0.12 A.U. and then remains relatively constant to within experimental uncertainty from 110 to 400 mM. The standard deviation on the compartment extinction decreases steeply from 0.04 to 0.01 A.U. between 100 and 200 mM, and then decreases more slowly up to 400 mM.

Figures 4.9 shows that the average extinction does not change with the concentration of calcium chloride added to the droplets, but that the standard deviation changes significantly. The standard deviation is more sensitive to the optical heterogeneity observed in the raw extinction trace, while this heterogeneity is obscured when considering the mean extinction alone. The data presented in Figures 4.7 and 4.8 correspond to the time-averaged extinction of

individual droplet compartments. The time averaged extinction shows good agreement with visual observations of emulsion microstructural changes in the compartments, and good qualitative agreement with results from macroscale tests. However, this simple approach obscures the significant changes in the extinction profile along the length of the droplet that are observed in many experiments, and that are observed in Figure 4.6. In some experiments, the average extinction remains nearly unchanged while the shape of the extinction profile within the droplets changes dramatically. Figure 4.9 shows this effect for the situation in which the droplet compartments are mixed with varying concentrations of either sodium or calcium chloride, in the absence of the cationic polymers.

4.4.   Discussion

Figures 4.7, 4.8, and 4.9 show that there is good qualitative agreement between the stability of the emulsions observed in the macroscale tests and that observed in the millifluidic platform. However, there are quantitative differences between the two tests. For example, the minimum extinction of the droplet compartments for Polymer A and Polymer B shown in Figure 4.7 occurs at 175 and 60 ppm respectively, while the best performance of the polymers in the macroscale tests shown in Figure 4.1 occurs at 250 ppm for Polymer A and 100 ppm for Polymer B. Part of the differences in the effective concentrations arise from the very coarse compositional resolution of the macroscale tests, in which polymer concentration changes between any two bottles can be 50 to 500 ppm without significant experimental time invested. In the millifluidic platform, the difference in polymer concentration between any two droplet compartments is

about 2 to 3 ppm. The compositional resolution of the millifluidic platform can be tuned by generating more or fewer droplet compartments for a fixed total concentration range. Alternatively, the number of droplet compartments can be fixed and the total concentration range adjusted by varying the concentration of the stock solutions contained in the syringes.

Two other important factors contribute to differences between the macro and micro scale experiments. First, the crude oil emulsion droplet size distribution sampled in the millifluidic platform is different than the size distribution sampled in the macroscale tests. This is a result of creaming within the syringes, which leads to larger droplets fractionating to the outside of the syringe barrel while smaller droplets remain suspended and can be injected into the millifluidic tubing. Second, the type and the magnitude of mixing experienced by the droplet compartments is significantly different from that occurring in the macroscale experiment. At the millifluidic scales, flows are predominantly laminar while at the macroscale, vigorous mixing is typical.

As is shown in Figure 4.3, the synthetic produced emulsion is unstable. The instability of the dispersion has important consequences for comparisons made between the macroscale tests and the millifluidic tests, and for interpretation of the emulsion structure visible in Figure 4.5. In a macroscale experiment, several milliliters of the synthetic produced emulsion are taken from the container in which the oil and water mixture is homogenized. The sample is collected within seconds of the end of homogenization. The emulsion is initially well mixed, and contains a broad distribution of droplet sizes, from hundreds of

microns to less than 1 micron. Polymers or salt are added to this polydisperse emulsion and vigorously shaken. Within the polydisperse mixture, the largest and smallest crude oil droplets are able to interact with each other and with the additives. Droplet-droplet interactions are important to the mechanisms by which emulsions are destabilized, and the relative sizes of the droplets plays an important role in effects such as Ostwald ripening. If a sample of the emulsion is obtained after the dispersion has had the opportunity to settle, the size distribution of the oil droplets will not be representative of the original emulsion. In the millifluidic experiment a fraction of the synthetic emulsions is drawn into a syringe and the syringe is placed in a syringe pump. This process requires 2 to 5 minutes to complete. Once the syringe in loaded in the pump, the dispersion is pumped into the droplet generator for approximately 10 minutes as part of a hydrodynamic equilibration period before beginning the concentration gradient experiment. The equilibration period allows the pumps to mechanically engage the syringe and for the droplet generator to achieve steady state operation to ensure stable and uniform droplet compartment generation. During the equilibration period, creaming is visually evident in the syringe. For this reason, the size distribution of crude oil droplets and the total volume fraction of crude oil being delivered to the droplet compartments are different than those examined in the macroscale tests. The experimental procedure effectively selects a fraction of the dispersion containing smaller droplets.

We can estimate the distribution of droplet sizes that may be captured in the millifluidic droplet generator by estimating the time scales for creaming as a

function of droplet diameter. For a spherical oil droplet suspended in water, neglecting interactions with surrounding droplets or the walls of the vessel, the droplet experiences an upward buoyant force due to gravity and an opposing viscous drag force. The terminal velocity of the droplet is given by the balance of these two forces,

$$\overline{v} = \frac{F_{bouyant}}{F_{Drag}} = \frac{2R^2\Delta\rho}{9\mu}\overline{g} \; .$$

(4.2)

where R is the radius of the droplet, $\Delta\rho$ is the density difference between the oil and water, g is the acceleration due to gravity, and μ is the viscosity of the water. Multiplying Equation 4.2 by a relevant time scale gives a vertical distance or length scale over which we expect the oil droplets to travel. In the millifluidic experiment, the emulsion settles in the syringe for up to 15 minutes before the first droplet compartment to be analyzed is produced. Using the material properties of pure water and the density of light crude oil of approximately 827 kg/m^3 (West Texas intermediate crude oil), the length scales for sedimentation of a 1, 10, and 100 μm diameter droplet are 100 μm, 10 mm, and 1 m, respectively, in a 15 min time period. Combined with the size distributions of the original produced emulsion shown in Figure 4.3, we can see that the droplet compartments are likely to contain only the smallest fraction of crude oil drop sizes, corresponding to drop diameters of the order of 1 μm and smaller.

In addition to sampling a different fraction of the emulsion size distribution, the macroscale and microscale experiments subject the emulsion and

clarifier mixture to substantially different mixing conditions. Mixing is challenging in traditional microfluidic devices[31,37,38]. Fluids flow in channels with characteristic dimensions of the order of tens to hundreds of microns exhibit highly laminar flow characteristics. Viscous forces dominate inertia, capillary forces compete with viscous forces, and gravity is typically negligible compared with interfacial effects[22]. The dimensionless groups relevant for mixing in this droplet-based system and that will help us quantify the differences between the droplet compartments and macroscale bottle tests are the Reynolds number and the Peclet number,

$$\text{Re} = \frac{\rho V l}{\mu} \qquad (4.3)$$

$$Pe = \frac{lV}{D} \qquad (4.4)$$

where Re is the Reynolds number, which is a ratio of inertia to viscous forces, Pe is the Peclet number, which is a ratio of the rate of convective mass transfer to the rate of diffusion. The characteristic or average fluid velocity is given by V, ρ is the fluid density, l is a characteristic length scale, μ is the viscosity of the continuous phase fluid, and D is the diffusion coefficient of the species of interest within the aqueous medium. These dimensionless parameters arise from scaling of the governing equations for momentum and mass transfer.

In the millifluidic platform presented here the relevant length scale is approximately 0.5 mm, which is the radius of the tubing containing the droplet compartments. The viscosity of the continuous phase perfluorocarbon fluid is 24

mPa·s and the density is 1.94 g/mL. Although the presence of the crude oil emulsion, salts, and polymeric clarifiers may influence the material properties of the aqueous droplet compartments, the concentrations of these additives are low and for the purposes of the scaling analysis presented here, the properties of the dilute droplet compartments are assumed to be equal to that of pure water. Using these material properties, a Reynolds number of approximately $Re \approx 0.04$ is obtained for the continuous phase fluid and $Re \approx 0.5$ is obtained for the flow within the droplet compartments. In both cases the characteristic velocity is taken to be the average input fluid velocity using the combined applied volumetric flow rate of 45 µl/min for the droplet phase fluid and the continuous phase fluid, divided by the cross sectional area of the 18 gauge PTFE tubing (Ø = 1.07 mm). For both fluids the Reynolds number is less than one, suggesting that viscous forces dominate inertia and that the flow is laminar and reversible which is consistent with microscopy observations.

A Peclet number can be estimated for each species within the droplet compartment. Estimating the diffusion coefficient of the cationic polymers to be of the order of 2 x 10^{-11} m^2/s, the Peclet number associated with the diffusion of the polymers across the radius of the droplet is $Pe = 2$ x 10^4. The crude oil droplets will also diffuse within the droplet compartment. Assuming the average oil droplet diameter in the produced emulsion is of the order of 1 µm, a diffusion coefficient for the droplets in water can be estimated from the Stokes-Einstein relation to be $D = 4$ x 10^{-13} m^2/s. In this case, the Peclet number associated with diffusion of the oil droplets is of the order of $Pe = 1$x10^6. For both the polymers

and the oil droplets, the Peclet number is very large, suggesting that advection of the droplet compartments downstream dominates transverse diffusion of species across the compartment. Given the diffusion coefficient of each species and a time scale over which diffusion takes place we can estimate a length scale for the characteristic distance over which a species will diffuse. The length scale for diffusion of 1 μm diameter crude oil droplets in the 900 s in which the droplet compartments travel from the droplet generator to the detector is 20 μm. For the polymers, the length scale is 100 μm. The radius of the droplet is approximately 500 μm, so we would not expect significant diffusion of either species across the droplet during the time that the droplets reside in the tubing.

Based strictly on this scaling analysis, we would not expect the droplet compartments to be well mixed by the time they reach the spectrophotometer. However, the images shown in Figure 4.5 appear to visually indicate that the downstream droplets are relatively uniform. In addition, the repeatable dose-dependent effect of clarifier concentration exhibited in Figure 4.7, and the general qualitative agreement observed between the macroscale and microscale results indicate that the process undertaken in the millifluidic device is consistent. The scaling analysis does not take into account important mixing effects that are unique to confined flows of droplets. Mixing occurs during the pinch-off of the droplet compartments at the nozzle of the droplet generator, and as a result of the deformation of the droplet as it passes through the restriction between the droplet generator and the downstream tubing. Mixing also occurs due to the recirculating flows occurring within the droplets as they translate along the tubing. These three

types of mixing induce folding and reorientation of the fluid layers inside the droplet compartment, redistributing the components and reducing the average distance between regions rich in water, crude oil droplets, and additive (polymers or salt). These phenomena will help ensure that the clarifier added to the droplet compartments is evenly mixed throughout the compartment and brought into intimate contact with the emulsion.

In Figure 4.5 (A), distinct layered regions are observed inside the droplet compartments. The three droplet phase fluids enter the nozzle from the left, outside of the field of view of the image. The water enters from the top, the crude oil dispersion from the center, and the additive stream from the bottom. Since the Reynolds number is low, we do not expect mixing or reorientation of these three laminated layers as they travel along the 40 mm long entrance nozzle. In the freshly generated droplet, a transparent top layer, cloudy center layer, and transparent bottom layer are observed, corresponding to each of the three incoming streams.

Mixing occurs as the droplet phase fluid leaves the dispersed phase fluid inlet tube and fills the outer capillary of the droplet generator as can be seen in Figure 4.5. This effect is referred to as 'twirling' and has been described in detail for microfluidic droplet-based devices[31]. We observe this type of mixing in the millifluidic platform, which results in a reduction in the length scales over which the additives and oil droplets must diffuse. In Figure 4.5 the top and bottom transparent 'layers' already contain some of the produced emulsion, as indicated by their turbidity.

Mixing also occurs as the droplet transitions from the droplet generator (Figure 4.5 (A)) to the downstream tubing (Figure 4.5 (C)). The interior diameter of the droplet generating section is 1.5 mm while the diameter of the downstream tubing is 1 mm. The droplets are forced to elongate and accelerate, inducing further mixing within the compartment.

The primary mechanism by which the droplet compartments are mixed results from the recirculating flows that occur in the droplets as they are carried downstream to the detector. Viscous interactions between the continuous phase fluid, which forms a thin film separating the droplet compartments from the tubing wall[33,39], transfers momentum to the droplets across the oil/perfluorocarbon interface. The recirculating flows inside droplets in circular and rectangular capillaries have been studied theroetically[34,35,40] and experimentally[41–43]. The speed of the flow inside the droplet, U, was found to scale with the average velocity of the continuous phase fluid, V,

$$U \propto \frac{V}{(1+\varepsilon\lambda)}. \tag{4.4}$$

where ε is a small parameter related to the thickness of the lubricating thin film between the droplet and the tubing wall that scales with the capillary number to the two thirds power[33]. The term λ is the ratio of the viscosity of the droplet divided to the viscosity of the continuous phase fluid. Hodges *et al.* found that for droplets for which $\varepsilon\lambda \ll 1$, the droplet velocity is approximately equal to the average fluid velocity $V \approx U$. If the velocity of the recirculating flows inside the droplet is approximately equal to the average droplet velocity, and one full

recirculation of one hemisphere of the droplet occurs in a distance approximately twice the droplet length, then in the 900 s that the droplet travels downstream to reach the detector, we would expect the contents of the compartment to experience approximately 53 complete recirculations. Each recirculation redistributes the crude-oil-droplet rich layer contained in the center of the droplet, since the recirculation forms lobes occupying the top half and bottom half of the droplet. This redistribution reduces the lengths separating regions rich in polymers, salts, or oil droplets, allowing diffusion to achieve thorough mixing between the components. Due to this effect, the results observed in the device are relevant to the processes on the bottle test and greater industrial scale despite their significantly different length scales, and applied mixing

4.5.   Conclusions

We have developed a semi-automated droplet-based fluid handling platform capable of rapidly generating tens to hundreds of microliter-scale droplet compartments containing a dilute submicron-scale crude-oil-in-water emulsion. The compartments are spatially indexed and the concentration of additives in each droplet compartment can be precisely controlled and varied from compartment to compartment. Using this platform, the effect of three cationic polymers and two salts on the stability of a dilute crude-oil-in-water emulsion is investigated as a function of additive concentration. The compositional resolution of the droplet-based approach can be tuned as desired. In the experiments presented here, the concentration increments by 2 to 3 ppm from compartment to compartment. The optical extinction of the dilute oil-in-water emulsion compartments is found to vary with cationic polymer concentration in qualitative agreement with macroscale experiments, exhibiting a minimum extinction at an intermediate concentration that is different for each cationic polymer which is also related to the molecular weight of the polymer. Changes in the average optical extinction indicate changes in emulsion microstructure, with decreasing droplet extinction corresponding to lower emulsion stability, and thus improved clarifier performance as observed in macroscale tests. The concentration of cationic polymer required to treat the produced emulsion is lower in the millifluidic platform than in microscale experiments, and the effective concentration decreases with increasing polymer molecular weight for the three polymers considered here. Surface charge plays an important role in forming and stabilizing

the dilute crude-oil-in-water emulsions prepared under the conditions investigated in this study. The oil droplets have a high, negative electrophoretic mobility, suggesting a large, negative zeta potential. The synthetic crude oil in water emulsions are effectively separated by the addition of either sodium chloride or calcium chloride, and the effect is captured in both macroscale and microscale experiments. Cationic polymers and simple salts were shown to be effective at destabilizing these emulsions, or preventing the emulsion from being formed in the case of the latter.

4.6. References

1. Wong, S. F., Lim, J. S. & Dol, S. S. Crude oil emulsion: A review on formation, classification and stability of water-in-oil emulsions. *J. Pet. Sci. Eng.* **135,** 498–504 (2015).

2. Sjoblom, J. *et al.* Our current understanding of water-in-crude oil. Recent characterization techniques and high pressure performance. *Adv. Colloid Interface Sci.* **102,** 399–473 (2003).

3. *Petroleum Engineering Handbook*. (Society of Petroleum Engineers, 2007).

4. Maitland, G. . Oil and gas production. *Curr. Opin. Colloid Interface Sci.* **5,** 301–311 (2000).

5. Fakhru'l-Razi, A. *et al.* Review of technologies for oil and gas produced water treatment. *J. Hazard. Mater.* **170,** 530–551 (2009).

6. Amyx, J. W., Bass, D. M. & Whiting, R. L. *Petroleum reservoir engineering: physical properties*. **1,** (McGraw-Hill College, 1960).

7. Zhang, J. *et al.* Comparison of Performances of Different Types of Clarifiers for the Treatment of Oily Wastewater Produced from Polymer Flooding. *Can. J. Chem. Eng.* **93,** 1288–1294 (2015).

8. Hirasaki, G. J. *et al.* Separation of produced emulsions from surfactant enhanced oil recovery processes. *Energy and Fuels* **25,** 555–561 (2011).

9. Wiedeman, A. in *Prod. Water 2* 27–41 (Springer, 1996).

10. Khatib, Z., Verbeek, P. & others. Water to value-produced water management for sustainable field development of mature and green fields. *J. Pet. Technol.* **55,** 26–28 (2003).

11. Reynolds, R. R. Produced Water and Associated Issues. *Oklahoma Geol. Surv.* (2003).

12. Glickman, A. H. Produced water toxicity: steps you can take to ensure permit compliance. in *API Prod. Water Manag. Tech. Forum Exhib. Lafayette, LA* (1998).

13. Sirivedhin, T., McCue, J. & Dallbauman, L. Reclaiming produced water for beneficial use: salt removal by electrodialysis. *J. Memb. Sci.* **243,** 335–343 (2004).

14. Veil, J. A., Pruder, M. G., Elcock, D. & Redweik, R. J. *A White Paper Describing Produced Water from Production of Crude Oil, Natural Gas, and Coal Bed Methane*. (2004). at <http://www.netl.doe.gov/kmd/cds/disk2/white_paper-final.pdf>

15.   Yan, Y. D., Glover, S. M., Jameson, G. J. & Biggs, S. The flocculation efficiency of polydisperse polymer flocculants. *Int. J. Miner. Process.* **73,** 161–175 (2004).

16.   Breit, G., Klett, T. R., Rice, C. A., Ferderer, D. A. & Kharaka, Y. National compilation of information about water co-produced with oil and gas. in *5th Int. Pet. Environ. Conf. Albuquerque, NM, Oct* 20–23 (1998).

17.   Leopold, G. in *Emuls. Fundam. Appl. Pet. Ind.* (Schramm, L. L.) 341–383 (1992). doi:10.1021/ba-1992-0231.ch010

18.   Maia Filho, D. C., Ramalho, J. B. V. S., Lucas, G. M. S. & Lucas, E. F. Aging of water-in-crude oil emulsions: Effect on rheological parameters. *Colloids Surfaces A Physicochem. Eng. Asp.* **405,** 73–78 (2012).

19.   Maia Filho, D. C., Ramalho, J. B. V. S., Spinelli, L. S. & Lucas, E. F. Aging of water-in-crude oil emulsions: Effect on water content, droplet size distribution, dynamic viscosity and stability. *Colloids Surfaces A Physicochem. Eng. Asp.* **396,** 208–212 (2012).

20.   Theberge, A. B. *et al.* Microdroplets in microfluidics: an evolving platform for discoveries in chemistry and biology. *Angew. Chem. Int. Ed. Engl.* **49,** 5846–68 (2010).

21.   Pompano, R. R., Liu, W., Du, W. & Ismagilov, R. F. Microfluidics using spatially defined arrays of droplets in one, two, and three dimensions. *Annu. Rev. Anal. Chem. (Palo Alto. Calif).* **4,** 59–81 (2011).

22.   Squires, T. M. & Quake, S. R. Microfluidics: Fluid physics at the nanoliter scale. *Rev. Mod. Phys.* **77,** 977–1026 (2005).

23.   Whitesides, G. & Stroock, A. Flexible methods for microfluidics. *Phys. Today* **54,** 42–48 (2001).

24.   Song, H., Chen, D. L. & Ismagilov, R. F. Reactions in droplets in microfluidic channels. *Angew. Chemie - Int. Ed.* **45,** 7336–7356 (2006).

25.   Lorber, N. *et al.* Some recent advances in the design and the use of miniaturized droplet-based continuous process: applications in chemistry and high-pressure microflows. *Lab Chip* **11,** 779–87 (2011).

26.   Engl, W., Backov, R. & Panizza, P. Controlled production of emulsions and particles by milli- and microfluidic techniques. *Curr. Opin. Colloid Interface Sci.* **13,** 206–216 (2008).

27.   Christopher, G. F. & Anna, S. L. Microfluidic methods for generating continuous droplet streams. *J. Phys. D. Appl. Phys.* **40,** R319–R336 (2007).

28.   Rabiee, A., Ershad-Langroudi, A. & Zeynali, M. E. A survey on cationic polyelectrolytes and their applications: Acrylamide derivatives. *Rev. Chem.*

Eng. **31,** 239–261 (2015).

29. Berg, J. C. *Interfaces & Colloids*. (World Scientific, 2010).

30. Garstecki, P., Fuerstman, M. J., Stone, H. A. & Whitesides, G. M. Formation of droplets and bubbles in a microfluidic T-junction-scaling and mechanism of break-up. *Lab Chip* **6,** 437–46 (2006).

31. Tice, J. D., Song, H., Lyon, A. D. & Ismagilov, R. F. Formation of Droplets and Mixing in Multiphase Microfluidics at Low Values of the Reynolds and the Capillary Numbers. *Langmuir* **19,** 9127–9133 (2003).

32. Tice, J. D., Lyon, A. D. & Ismagilov, R. F. Effects of viscosity on droplet formation and mixing in microfluidic channels. *Anal. Chim. Acta* **507,** 73–77 (2004).

33. Bretherton, F. P. The motion of long bubbles in tubes. *J. Fluid Mech.* **10,** 166 (1961).

34. Hodges, S. R., Jensen, O. E. & Rallison, J. M. The motion of a viscous drop through a cylindrical tube. *J. Fluid Mech.* **501,** 279–301 (2004).

35. Ma, S. *et al.* On the flow topology inside droplets moving in rectangular microchannels. *Lab Chip* **14,** 3611–3620 (2014).

36. Ismagilov, R. F., Stroock, A. D., Kenis, P. J. A., Whitesides, G. & Stone, H. A. Experimental and theoretical scaling laws for transverse diffusive broadening in two-phase laminar flows in microchannels. *Appl. Phys. Lett.* **76,** 2376 (2000).

37. Stone, H. A., Stroock, A. D. & Ajdari, A. ENGINEERING FLOWS IN SMALL DEVICES. *Annu. Rev. Fluid Mech.* **36,** 381–411 (2004).

38. Ottino, J. M. & Wiggins, S. Introduction: mixing in microfluidics. *Philos. Trans. A. Math. Phys. Eng. Sci.* **362,** 923–935 (2004).

39. HODGES, S. R., JENSEN, O. E. & RALLISON, J. M. The motion of a viscous drop through a cylindrical tube. *J. Fluid Mech.* **501,** 279–301 (2004).

40. LAC, E. & SHERWOOD, J. D. Motion of a drop along the centreline of a capillary in a pressure-driven flow. *J. Fluid Mech.* **640,** 27 (2009).

41. Jakiela, S., Korczyk, P. M., Makulska, S., Cybulski, O. & Garstecki, P. Discontinuous Transition in a Laminar Fluid Flow: A Change of Flow Topology inside a Droplet Moving in a Micron-Size Channel. *Phys. Rev. Lett.* **108,** 1–5 (2012).

42. Kinoshita, H., Kaneda, S., Fujii, T. & Oshima, M. Three-dimensional measurement and visualization of internal flow of a moving droplet using

confocal micro-PIV. *Lab Chip* **7,** 338–46 (2007).

43.   Wang, C., Nguyen, N.-T. & Wong, T. N. Optical measurement of flow field and concentration field inside a moving nanoliter droplet. *Sensors Actuators A Phys.* **133,** 317–322 (2007).

Chapter 5. Measuring Partition Coefficients of Single Walled Carbon Nanotubes in Aqueous Two Phase Microliter Droplets

5.1   Introduction

The distribution of a dispersed species between two immiscible liquid phases, expressed as the partition coefficient, is a critical parameter for designing and evaluating the performance of laboratory and industrial-scale liquid-liquid separation processes. The lack of data relating the partition coefficient of a compound to experimental parameters continues to present a major roadblock to the large-scale optimization of aqueous two phase separations. This is particularly apparent in the purification of single wall carbon nanotubes, and has restricted their wide-spread application. State of the art methods for screening partition coefficients as a function of experimental parameters such as temperature and composition require milliliters of sample per data point, in addition to labor intensive handling and detection procedures. Here, we demonstrate a high throughput, low volume semi-automated platform for mapping the partition coefficient of carbon nanotubes as a function of matrix composition.

Single wall carbon nanotubes (SWCNTs) are cylindrical carbon allotropes whose impressive thermal, mechanical, and electrical properties have made them the focus of significant research effort since their initial discovery[1,2]. These unique, nearly one-dimensional materials exhibit a variety of interesting properties, such as ballistic transport of electrons and ultra-high thermal conductivity, with numerous potential applications[2] in advanced composite materials[3], field effect transistors[4], display technology[5], and hydrogen storage[6].

One of the key challenges preventing widespread application of these materials is a lack of scalable methods to purify and isolate nanotube species with specific properties. Synthesis methods for nanotubes generate a carbonaceous soot-like hydrophobic powder containing a minority population of SWCNTs[7]. Further complicating separation procedures, single wall carbon nanotubes exist as dozens of different isomers or 'species', each with distinct electronic, thermal, and mechanical properties[8]. These nanotube species are uniquely identified in terms of their (n,m) chiral vector, which determines the diameter, optical properties including absorption, and whether they are semi-conducting or metallic. Isolating specific carbon nanotube species so that they can be used in applications is a significant challenge[9]. Current separation methods primarily rely on high speed ultra-centrifugation in density gradient media[10–17] or chromatography based methods[9,18–22], although other techniques have been demonstrated[23]. Generally, these approaches are expensive to implement, require specialized equipment, offer low throughput, or present challenges to cost effective scale up.

Liquid-liquid extraction is a scalable, tunable technique for partitioning analytes between two immiscible fluid phases that share an interface. Often, one phase is aqueous and the other organic. For example, the distribution of compounds in an octanol-water system is used in the development of active pharmaceutical ingredients to simulate the way that compounds distribute throughout the body. In environmental science, octanol-water partitioning is used to predict how compounds will distribute in soil and ground water[24]. Liquid-liquid

extraction can also be accomplished using two aqueous phases. Combining two structurally dissimilar polymers or a polymer and salt in water above a certain concentration will result in spontaneous decomposition of the homogenous mixture into two immiscible aqueous phases[25,26]. In aqueous two-phase systems (ATPS), each phase is rich in one of the polymers/salt, while the other phase is rich in the other polymer/salt. The phases exhibit very high water content, 80-90 % (w/w), and very low interfacial tension, 1-1000 µN/m[27–29].

The preference of a component to partition to a given phase is determined by the chemical potential in each phase, which results from the net effects of hydrophobic, electrostatic, steric, conformational, van der Waals attraction, and other molecular interactions between the analyte and the components of each phase[25,30]. Collectively, these effects lead to preferential partitioning of particles into one phase while being depleted in the other. The distribution of a component between the resulting two water-rich phases provides important information about the surface properties of that compound, since these types of separations are driven by such properties[25], rather than density or hydrodynamic drag. ATPSs are particularly well suited to separating water soluble molecules based on slight differences in hydrophobicity.

Recent work has shown that polymer-polymer aqueous two phase systems[25,26] can effectively partition carbon nanotubes as a function of their diameter, length, and degree of metallicity[22,31–38]. Varying temperature, salt concentration, and surfactant concentration in these systems allows for selective partitioning of nanotubes[32–34]. It has been shown that surfactants competitively

adsorb to and assemble on the intrinsically hydrophobic nanotube surface in a chirality-specific way[34,39–41]. The hydrophobic surfactant tails adhere to the carbon lattice, while the hydrophilic head groups protrude into the aqueous solution. Changes in temperature, surfactant type, and salt concentration modify surfactant-surfactant and surfactant-nanotube interactions, for example by screening interactions between the charged surfactant head groups. For mixed surfactant systems in aqueous two phase extraction, it was found that nanotubes wrapped in sodium dodecyl sulfate are slightly less hydrophilic than those wrapped in sodium deoxycholate[34]. The result was that the sodium dodecyl sulfate wrapped SWCNTs partitioned into the slightly less hydrophilic polyethylene glycol-rich phase, while the sodium deoxycholate wrapped nanotubes partitioned into the slightly more hydrophilic dextran-rich phase.

Aqueous two phase extraction is an extremely scalable technique amenable to both continuous flow and batch processing, but currently very little data exists regarding how the distribution of carbon nanotube species in an ATPS is affected by matrix composition. Rational design of large scale separations requires information on how changes in the composition of the ATPS affect the partition coefficient for particular SWCNT species. Macroscale, benchtop techniques for measuring the distribution of analytes in an ATPS are poorly suited to exploring the huge operating space controlling partitioning, primarily due to the low speed of testing and the high cost and scarcity of materials needed to perform these experiments.

In this chapter we measure the partition coefficients of three different samples of single-wall carbon nanotubes in an aqueous two phase system using a high throughput droplet-based millifluidic platform coupled with in-situ per-droplet absorption spectroscopy. Implementing microfluidic methods to generate, isolate, and transport samples in millimeter-scale copmpartments facilitates the identification and optimization of the critical parameters for aqueous two phase extraction of carbon nanotubes, while reducing sample consumption by up to two orders of magnitude compared to current procedures. In each experiment we vary the concentration of one surfactant, while fixing the concentration of a second surfactant in the matrix mixture.

5.2   Materials and Methods

To study partitioning of SWCNTs as a function of surfactant concentration, polymer-polymer aqueous two phase systems are generated by combining appropriate amounts of polyethylene glycol (PEG, 6000 g/mol, Alfa Aesar), dextran (DEX, 64,000 − 76,000 g/mol, Sigma Aldrich) and deionized water (Barnstead Ultrapure II, Thermo Scientific) by weight in order to achieve the stock cocentrations listed in Table 5.2. The polymer type and molecular weight are chosen in order to mirror the systems reported previously in the literature for successful SWCNT separations[22,31–38].

Experimental System	Nanotube Species	Phase Forming Polymers (w/w)	Sodium Dodecyl Sulfate (w/w)	Sodium Deoxycholate (w/w)
System A	EG150X Semi-sorted			0.05 %
System B	EG150X Metal-sorted	6 % PEG 8 % DEX	0.27 –1.60 %	
System C	Raymor Metal-sorted			0.07 %

Table 5.1. Compositions of the systems investigated in this work. The concentrations listed are the overall concentration of the aqueous two-phase systems.

Table 5.1 provides the compositions of the three nanotube systems investigated in this study. The compositions listed in the table are the overall or total compositions of the final two phase systems as generated either *via* droplets or macroscale methods.

The three carbon nanotube samples are graciously provided by the National Institute of Standards and Technology dispersed in 1 % (w/w) sodium deoxycholate (DOC) and are used as received. The samples consist of mixtures of several single wall carbon nanotube species that have been sorted by their degree of metallicity. The nanotube samples are prepared by a multi-step separation and purification process to isolate a subset of SWCNT species. Briefly, aqueous dispersions of single-wall carbon nanotube soots EG150X (Southwest Nanotechnologies, Norman OK) and RN220 (plasma torch synthesis, Raymor Nanotechnologies lot #RNB-020) in 20 g/L sodium deoxycholate (DOC) solutions are generated via tip sonication (6 mm tip, 45-60 min, 0.9 W/mL, sample in an ice bath) followed by centrifugation (Beckman Coulter JA2-21 centrifuge, JA-20 rotor at 18 kRPM, 2 h), collecting the supernatant. These

dispersions are then processed by a rate-zonal ultracentrifugation separation[35], to isolate only the fully individualized SWCNT population. Each dispersion is then separated into metallic and semiconducting SWCNT rich fractions using benchtop aqueous two phase extraction[31,37]. Extracted populations are subsequently dialyzed to remove the two-phase separation polymers and to set the surfactant concentration to 10 g/L DOC solutions using forced ultrafiltration stirred cells (Millipore).

Absorbance spectra of the stock samples were collected on a CARY-5000 UV-visible-near infrared (UV-vis-NIR) spectrophotometer in 1 nm increments over the range from 1880 to 200 nm through a 1 mm pathlength quartz cuvette. Absorbance of a reference solution containing only 10 g/L DOC was acquired separately and subtracted from the sample spectra during data processing. The absorbance data was used to identify the wavelength of prominent absorption features of each of the nanotube samples. The precise concentration of nanotubes in the stock solution is unknown. Sodium dodecyl sulfate (SDS) is obtained from Fisher Scientific and used as received.

The millifluidic apparatus[42,43] used in the droplet-based experiments is constructed from off-the-shelf tubing (Cole Parmer, IDEX Scientific) and chromatography fittings (IDEX Scientific). The design and operation of the platform is described in more detail in the results section and in Chapter 3. Briefly, a six port manifold (P-152, IDEX) is connected to syringes (Gastight, Hamilton Co.) using fluorinated ethylene propylene (FEP) tubing (IDEX) and compression fittings (XP-235X, IDEX). The syringes are mounted in syringe

pumps (PHD2000, Harvard Apparatus). One outlet of the six port manifold is connected to a short section of polyether ether ketone (PEEK) tubing (1532, IDEX) which forms the nozzle of the millifluidic droplet generator. The nozzle fits inside a 1.5 mm ID section of polytetrafluoroethylene (PTFE) tubing (06605-52, Cole Parmer), connected by a T-fitting to an approximately 3 m long section of 18 gauge PTFE tubing (06417-41, Cole Parmer). The continuous phase fluid, a perfluorocarbon fluid (FC-70, 3M), is delivered by a separate syringe and pump to the T fitting. This configuration forms a coflow type droplet generator. The first 2 m of tubing are coiled and oriented horizontally. The last meter is mounted vertically as shown in Figure 5.1. Just prior to the optical flow cell and the camera, the PTFE tubing is replaced with a short section of 1 mm ID FEP (1673L, IDEX) tubing, which is more optically transparent than PTFE.

Syringe	Mixture (w/w)	Syringe	Mixture (w/w)
1	FC-70 Perfluorocarbon Oil	4	24 % PEG 6000 g/mol
2	Deionized Water	5	32 % DEX 64k – 76k g/mol
3	4 - 6 % Sodium Dodecyl Sulfate	6	SWCNTs in DOC & H_2O

Table 5.2. A list of the components placed in each syringe in the droplet-based SWCNT partitioning experiments.

Table 5.2 provides a list of each of the compositions of the 'stock' solutions present in each syringe used to generate droplets in the millifluidic platform. The concentrations in each syringe and the volumetric flow rates of each syringe are chosen such that the final system composition is equal to what is indicated in Table 5.1. The PEG, DEX, and SDS solutions are prepared by weight in 60 mL acid washed glass jars with PTFE lined lids and placed on magnetic stir plates to mix overnight to ensure the components are completely dissolved. The nanotube and DOC stock solutions are prepared by volume by adding 0.33 mL of 1 % (w/w) DOC and SWCNT dispersion to 0.66 mL of deionized water in a 2 mL micro centrifuge tube. The resulting solution is hand mixed and then used immediately in the partitioning experiments. A fresh nanotube solution was prepared for every experiment, since the diluted SWCNT stock solutions were observed to form a light-colored sediment layer several days after preparation.

In the millifluidic platform, a different spectrophotometer set up is used to obtain the optical absorption of the flowing droplet compartments. The optical absorbance of the droplets is measured at a fixed location approximately 3 m downstream of droplet production using a set of optical fibers (#1853, SI Photonics) connected to a benchtop spectrophotometer (Model 440, SI Photonics). The spectrophotometer is programmed to record the absorbance at up to ten specified wavelengths every 4 seconds for the duration of the experiment.

Images of the droplets are obtained every 10 seconds using a CCD camera (Prosilica GC, Allied Vision). The images are analyzed manually (ImageJ, NIH) to obtain the length of the droplet compartments. The volume of the droplet

compartments is calculated based on the length and by assuming the end caps of the droplets are perfect hemispherical.

The error bars which appear in the plots of absorbance are calculated from the standard deviation in the absorbance of high SWCNT concentration DEX-rich compartments at constant SDS concentration and without temperature control. The fluctuations in the compartment absorbance obtained under these conditions encompass multiple sources of error, including instrument error, pump dispensing error, experimental variations, and temperature variations. This error represents a conservative worst-case uncertainty. For much of the data, the error bars are not visible because they are smaller than the symbol size. For the partition coefficients, the error bars are calculated based on error propagation from the standard deviation described above. In all cases this uncertainty was smaller than the symbol size and is not visible on the semi-log scales in which the data is presented.

For the droplet volume, the uncertainty is obtained by propagation of the uncertainty in both measures of the droplet length, and the pixel-to-micron conversion factor. The uncertainty for the length and the conversion factor is obtained by repeatedly making measurements of the size of one droplet and taking the standard deviation in the values obtained. In every case, the error bars are much smaller than the symbol size for the plots shown. This is due primarily to the high resolution of the camera. Any variation in droplet size is then due to true differences, not instrument error.

5.3   Results and Discussion

To address the time consuming and labor intensive aspects of partition coefficient screening we develop a high throughput droplet based platform appropriate for multi-compartment droplets.
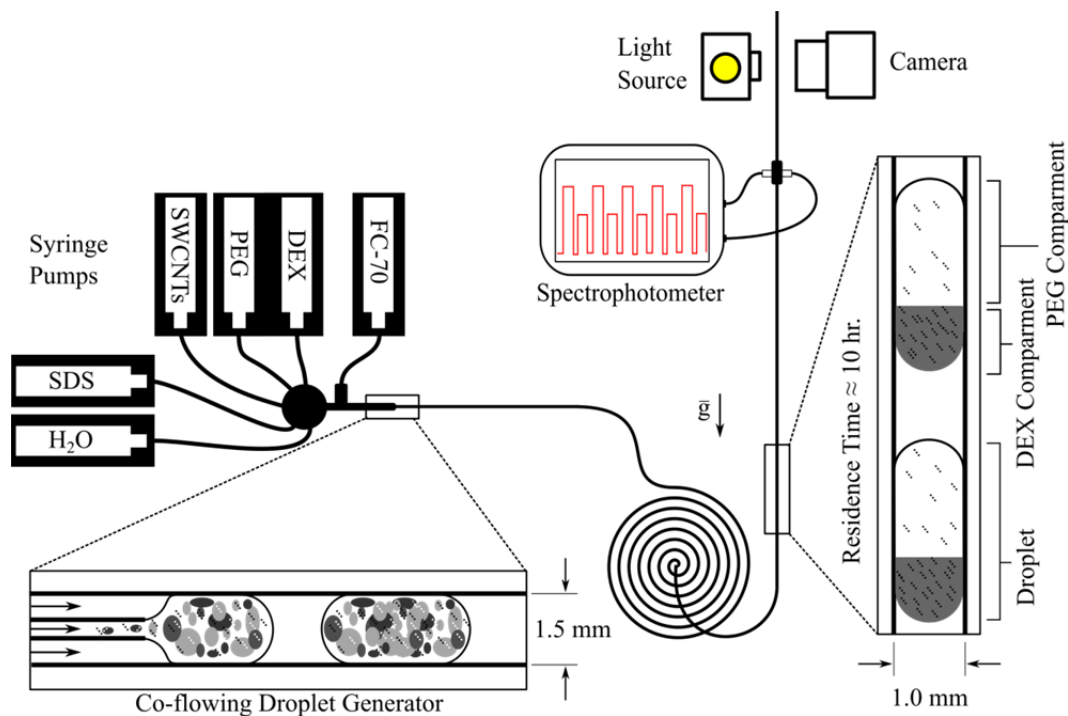
Figure 5.1. Schematic diagram of the droplet-based platform used to generate multi-compartment droplets. Five syringe pumps deliver the five droplet phase fluids, including the phase separating polymers on a single pump, and the carrier phase fluid, into a coflowing droplet generator. The generator produces approximately 8 μL droplets at a rate of about 8 droplets per minute. The drops flow through a 2 m long storage loop and then into a 1 m long vertical section of FEP tubing before reaching a spectrophotometer and camera which collect images and optical absorbance as a function of time.

Figure 5.1 is a schematic diagram of the millifluidic apparatus used to generate multi-compartment droplets. A set of five syringe pumps, three controlled by computer and two programmed manually, deliver a total of six separate fluid streams, listed in Table 5.2, to a millimeter scale coflowing droplet

generator. The PEG and DEX solutions occupy a single pump. The volumetric flow rates of the water and SDS pumps change as functions of time to generate a train of droplets with the desired gradient in composition. Two of the droplet phase fluids are concentrated solutions of PEG and DEX, and upon contact the polymers undergo a process of thermodynamic phase separation leading to the generation of two immiscible polymer-rich phases, or compartments, inside of each 7 – 10 microliter droplet. One of the compartments is rich in one of the polymers (PEG), and the other is rich in the other polymer (DEX). The interfacial tension between the compartments is extremely low, of the order of 0.1 to 1 mN/m[28], which causes the internal structure of the droplet to be highly sensitive to the velocity of the droplet. The interfacial tension between the polymer compartments, between the continuous phase fluid and each aqueous compartment, and the confinement provided by the tubing result in a droplet morphology in which each compartment is partially wet by continuous phase fluid, and the two compartments share a mutual interface within the droplet.

The platform operates in two stages: droplet generation and droplet detection. During droplet generation, the volumetric flow rate of the continuous phase fluid is set to 30 μL/min and the total volumetric flow rate of the droplet-phase fluids is set to 60 μL/min. After a hydrodynamic equilibration time of 5 min, two identical sets of approximately 30 - 40 sequential droplets are produced with a gradient in composition. The equilibration period allows the pumps to mechanically engage the syringes and for the droplet generator to achieve steady state operation. The volume of each droplet is between 7 and 10 μL and the drops

are generated at a rate of approximately 8 per min. During the generation stage, the droplets travel through a storage loop with an average velocity of 1.7 mm/min. The high volumetric flow rate and thus the high velocity of the droplets results in enhanced mixing of the components within the drops by increasing the magnitude of the recirculating flows inside of the droplets[44–47]. In the case of multi-compartment droplets, the recirculating flows lead to emulsification of the two immiscible polymer compartments[48], increasing the surface area of the contacting incompatible phases and enhancing the drive thermodynamic equilibrium.

After the desired number of droplets have been generated and their contents well mixed, the detection stage begins. The volumetric flow rate of the continuous phase fluid is set to 2 µL/min and the pumps delivering the droplet phase fluids are shut off. At a total volumetric flow rate of 2 µL/min, the velocity of the previously produced droplets is 0.04 mm/min. The length of the storage loop is chosen such that at the start of the detection stage, the first droplets produced in the previous stage have just reached the base of the 1 m vertical section of tubing. The reduced flow rate and the vertical mounting allow the two polymer compartments to demix, establish a stable interface, and obtain a configuration in which the PEG-rich phase and DEX-rich phases are driven to the top and bottom of the droplet due to density differences. The droplets spend approximately 10 hours from the time they are first generated until they reach the spectrophotometer at the end of the apparatus.

Emulsifying the compartments during the generation stage is critical for ensuring good mixing of the components inside of each droplet. However, during

optical detection, maintaining the stability of the interface between the two polymer compartments is critical to making accurate concentration measurements within each droplet compartment. These competing objectives lead to special considerations for the design and operation of the millifluidic platform. As the droplets translate through the tubing a spectrophotometer located at a fixed position downstream measures the absorbance across the entire diameter of the tubing every 4 seconds. To ensure that only the absorbance of either the PEG-rich or the DEX-rich compartment is collected, the compartments must be demulsified and occupy physically distinct regions within the droplet. It is also important that the position of the two compartments with in the droplet is the same in every droplet, since the absorbance in each compartment must be assigned to either the PEG-rich or the DEX-rich phase. This ideal configuration is depicted schematically in Figure 5.1, at the far right side, as the grey and white regions of the two vertically oriented droplets. This configuration is obtained when two conditions are met. First, the interfacial forces between the polymer compartments must be greater than the viscous forces acting on them due to their motion with in the tubing. If this condition is not met, the compartments will emulsify through viscous breakup of droplets, analogous to droplet break up in unconfined Stokes' flow[49]. Second, the flow direction of the droplets must be aligned with gravity. This geometric orientation leads to repeatable and predictable density driven segregation of the two polymer-rich phases.

These conditions can be quantified in terms of two dimensionless parameters. A dimensionless ratio of viscous stresses and interfacial stresses,

called the capillary number, arises from scaling the stress balance at the fluid-fluid interface[50]. The capillary number parameter estimates the relative importance of viscous and interfacial stresses, and is given by

$$Ca = \frac{\mu V}{\gamma},$$

(5.1)

where μ is the viscosity, V is the characteristic velocity, and γ is the interfacial tension between the fluids. Lee *et al*[48]. found that for a droplet composed of 5 % (w/w) PEG (8000 g/mol) and 4.5 % (w/w) DEX (500,000 g/mol) translating along a rectangular 300 micron diameter channel (130 μm height), the critical capillary number for the transition from a stable two compartment configuration to an emulsion of one phase inside the other was Ca ≈ 0.15. The analysis used the viscosity of the PEG-rich phase since the droplet assumed a spherical core-shell morphology in which the PEG-rich phase completely encapsulated the DEX-rich phase. In the millifluidic apparatus, we can estimate a capillary number for both the generation and the detection stages. In the generation stage the droplet velocity is $V = 1.7$ mm/min. The viscosity of the PEG-rich phase is $\mu = 7.7$ mPa·s and the viscosity of the DEX-rich phase is $\mu = 50$ mPa·s[51]. The interfacial tension between the PEG-rich and DEX-rich compartments is approximately 0.04 mN/min, which we estimate based on a power law relationship between interfacial tension and polymer concentration[28]. The presence of surfactants and nanotubes modifies this value but we neglect these contributions for the purposes of the scaling analysis. For the generation stage, these material properties yield $Ca_{PEG} = 0.4$ and $Ca_{DEX} = 2.5$, both of which are significantly larger than the

critical capillary number. For the detection stage, V = 0.04 mm/min and the corresponding capillary numbers are Ca_{PEG} = 0.01 and Ca_{DEX} = 0.06, both of which are significantly smaller than the critical value. Thus, the flow conditions in each of the two stages are suited for the objective in each stage.

The reduction in the characteristic capillary number in the detection stage prevents emulsification of the two polymer-rich compartments. Further organization of the compartments with in the droplet is accomplished by gravitational effects. For this to occur, gravity must overcome interfacial forces, which we have just shown are more important than viscous forces during the detection stage. The Bond number is a dimensionless parameter that estimates the competition of gravity and interfacial forces, and is given by

$$Bo = \frac{\Delta \rho g l^2}{\gamma},$$
(5.2)

where $\Delta \rho$ is the density difference between the two polymer compartments, g is the acceleration due to gravity, l is a length scale, and γ is the interfacial tension. Using an estimate for the density difference between the PEG-rich and DEX-rich phases of approximately $\Delta \rho$ = 56 kg/m^3 and taking the diameter of the tubing as the relevant length scale, the Bond number is Bo = 3.5, indicating that gravitational forces dominate interfacial forces at the polymer-polymer interface. The result is that the higher density, DEX-rich phase sinks to the 'bottom' of the droplet and the PEG-rich phase rises to the 'top', consistent with observations in macroscale phase separation[25]. Due to the confinement of the droplet in the

continuous phase perfluorocarbon fluid and the tubing, the droplet attains a capsule shape with two halves containing each of the two polymer-rich phases.
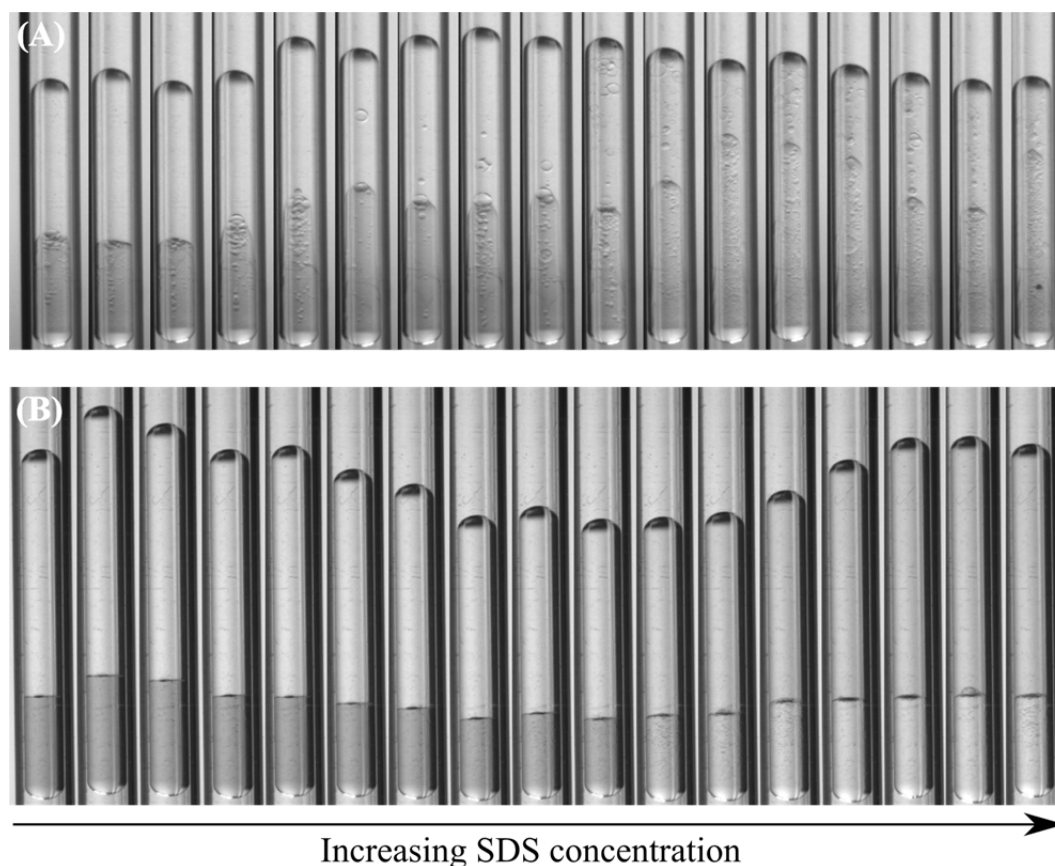
Figure 5.2. Two time sequences of images of droplets composed of SWCNT System A as they appear in the millifluidic apparatus at two different flow conditions. (A) Droplets moving at an average velocity of 0.2 mm/min, and (B) droplets with identical composition moving with an average velocity of 0.04 mm/min. The top portion of each droplet contains the PEG-rich compartment, and the bottom portion of each droplet contains the DEX-rich compartment. The overall concentration of SDS in each drop increases linearly from left to right, over the range of approximately 0.3 to 1.0 % (w/w). For compactness only every other droplet is shown. The inner diameter of the tubing is 1 mm and the average droplet volume is 7 – 10 μL.

Figure 5.2 contains two sets of images of multi-compartment droplets as they appear in the vertical section of the millifluidic platform and illustrates the effect of droplet velocity on the stability of the polymer compartments. The image sets show approximately every other droplet generated during the experiments. As

described in Materials and Methods, the droplets contain a mixture of polymers, surfactants, and a sample of carbon nanotubes (System A), all of which are dispersed in water. In Figure 5.2 (A) the total volumetric flow rate is set to 10 μL/min, corresponding to an average droplet velocity of 0.2 mm/min. In the first three droplets on the left, at low SDS concentration, a stable horizontal interface is visible between the upper PEG-rich compartment and the lower DEX-rich compartment. Moving to the right, as the concentration of SDS increases, the interface between the two phases becomes less clear, and dispersed droplets much smaller than the tubing diameter are visible in both of the compartments. At even higher SDS concentrations, the distinction between the PEG-rich and DEX-rich compartments is completely lost and the droplets appear as emulsions of the two polymer rich phases. In Figure 5.2 (B) the total flow rate is 2 μL/min and the droplets are moving at a corresponding velocity of 0.04 mm/s. For every droplet, the interface between the PEG-rich and DEX-rich phases is sharp, and no droplets appear dispersed in either compartment. From left to right, the optical brightness of the bottom, DEX-rich compartments increases with increasing SDS concentration, while the intensity of the top, PEG-rich compartments decreases with increasing SDS, although the change in the intensity of the PEG-rich compartments is less dramatic.

Figure 5.2 (A) shows the droplet morphology that occurs when the average velocity is too high during the detection stage, and conversely, in Figure 5.2 (B), when the velocity is appropriately low, the gross optical changes that occur in the droplet compartments due to the presence of SWCNTs. Following the

procedure for estimating the capillary number discussed for Figure 5.1, the capillary number associated with the DEX-rich compartment in Figure 5.2 (A) is $Ca_{DEX} = 0.30$ while the capillary number for the droplets in Figure 5.2 (B) is $Ca_{DEX} = 0.06$. Since these numbers lie above and below the critical capillary number, $Ca_{crit} \approx 0.15$, we would expect to see a transition from a stable two-compartment droplet to an emulsified droplet compartment. This is exactly what is observed in the experiments. For all of the remaining experiments described the detection velovity is 0.04 mm/s, corresponding to a capillary number below the critical value. From the images in Figure 5.2 it is also apparent that the droplets are polydisperse. Next, we quantify the volumes of the droplet compartments based on the images captured in the apparatus.
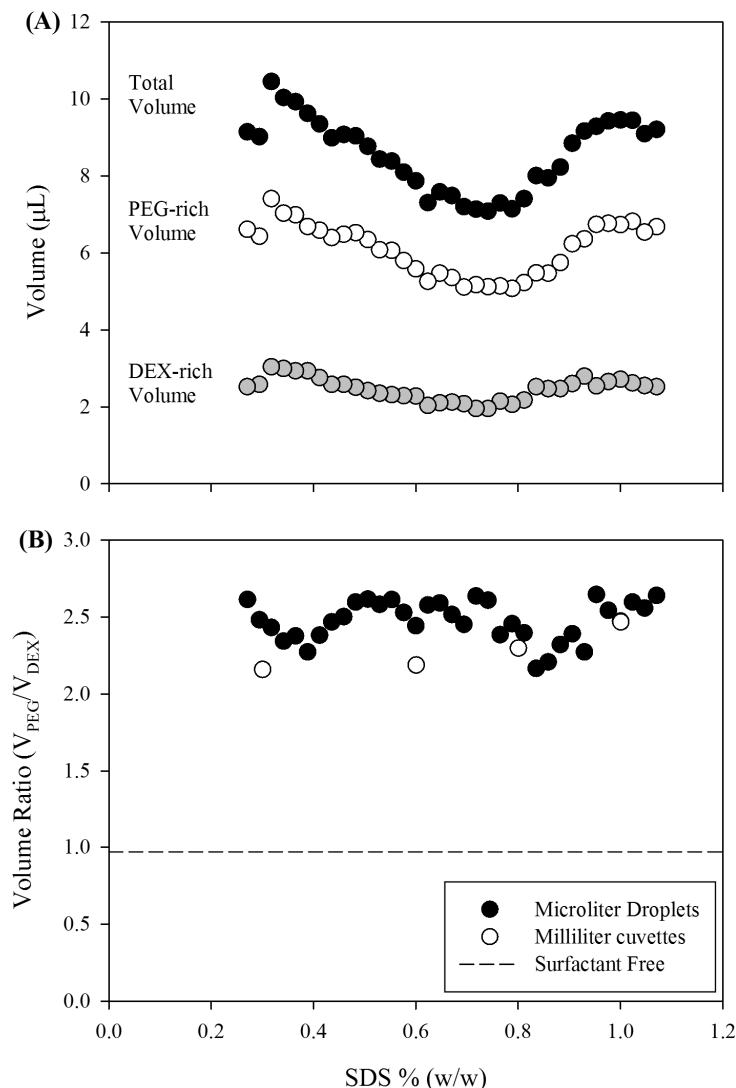
Figure 5.3. The total volume, the volume of each compartment, and the ratio of the compartment volume plotted as functions of the corresponding total concentration of SDS in each droplet for System A. **(A)** The volume of the PEG-rich phase (open circles), DEX-rich phase (grey circles), and the total volume (filled circles). **(B)** The ratio of the PEG-rich phase volume divided by the DEX-rich phase volume. The filled circles correspond to the data shown in part (A) for the droplet-based experiments. The open circles correspond to measurements made in 5 mL disposable cuvettes with the same composition of PEG, DEX, and SDS. The dashed line is the estimated equilibrium volume ratio obtained from a phase diagram for a two phase system composed of similar molecular weight PEG and DEX, but in the absence of surfactants.

Figure 5.3 (A) is a plot of the volumes of the droplet compartments as functions of the corresponding total SDS concentration for each droplet in the experiment shown in Figure 5.2 (B). The total drop volume varies non-

monotonically with surfactant concentration from a maximum of 10.5 μL at approximately 0.30 % (w/w) SDS to a minimum of 7 μL at about 0.70 % (w/w) SDS, and then increases again to approximately 9 μL at 1.0 % (w/w) SDS. The volume of the PEG-rich and DEX-rich compartments follow a similar trend as a function of droplet composition, suggesting that the droplet volume variations are a result of changes in droplet generation dynamics rather than in composition. Figure 5.3 (B) is a plot of the ratio of the volume of the PEG-rich phase divided by the volume of the DEX-rich phase as a function of SDS concentration. The filled circles correspond to data obtained from the microliter droplets, as shown in Figure 5.3 (A) and depicted in the images of Figure 5.2. The volume ratio varies from about 2.2 to 2.7 with an average value of 2.48 ± 0.13over the range of SDS concentration investigated. The open circles correspond to volume ratios obtained in macroscale experiments carried out with an identical composition of polymers and surfactants, but in the absence of carbon nanotubes. In the macroscale experiments, the average volume ratio is 2.28 ± 0.14 and the ratio increases slightly from 2.16 to 2.47 with increasing SDS concentration. The dashed horizontal line indicates the volume ratio obtained from a ratio of tie line lengths for the PEG-rich and DEX-rich phases taken from a published phase diagram[25] for a system composed of DEX T70 and PEG 6000 at the same concentration of PEG and DEX as in the millifluidic experiments, but in the absence of any other additives such as SDS.

These results demonstrate that the millifluidic droplets undergo phase separation consistent with macroscale samples, and that the presence of

surfactants significantly alters the thermodynamics of phase separation, leading to different volume ratios of the compartments compared with the surfactant free case. Further, although the total volume of the droplet compartments varies commensurate over the course of the experiment, the volume ratio of the compartments exhibits much smaller fluctuations, and does not change proportionally with the changes in total droplet volume. Since the volume ratio is sensitive to the overall composition of the droplet, these results suggest that the overall composition is uniform drop to drop, but that the dynamics of droplet breakup, and thus the total volume, are being altered by the addition of significant quantities of SDS. A decrease in the interfacial tension between the droplets and the carrier phase fluid due SDS absorption at the interface leads to an increase in the capillary number, and the physical mechanisms governing droplet breakup are known to change with capillary number[52,53]. Based on this we assume that the variation in volume does not impact the partitioning results as long as the composition of the phase separating compartments is consistent.

As indicated in Figure 5.2, gross qualitative changes in the optical intensity of the PEG-rich and DEX-rich compartments are observed in response to changes in the average concentration of added SDS. To quantify these changes and estimate a partition coefficient, we measure the optical absorption of each droplet compartment.
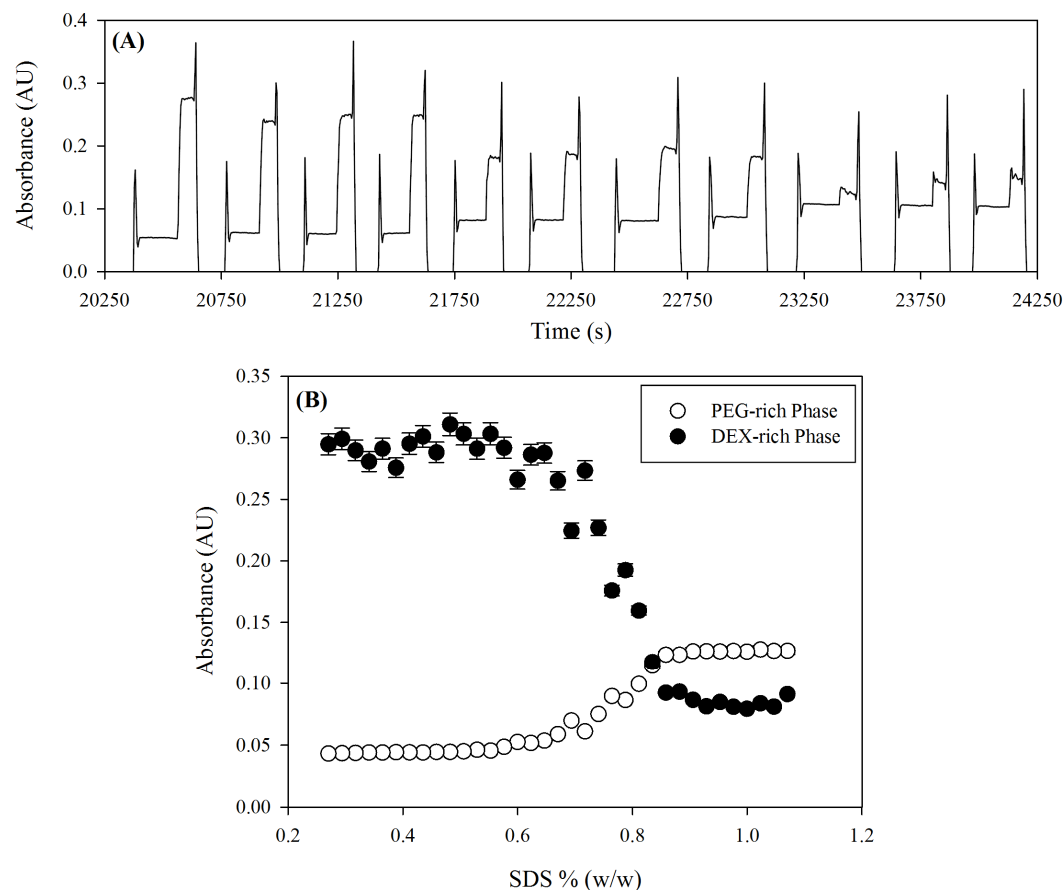
Figure 5.4. Optical absorbance for the train of multi-compartment droplets depicted in Figures 5.2 and 5.3. The absorbance measurements are made approximately 3 m downstream of the location of droplet production at a wavelength of 653 nm. **(A)** An optical absorbance trace for a set of multi-compartment droplets (System A). The total concentration of SDS increases for each droplet (as a function of time), while the concentration of all other components is kept constant. **(B)** The time averaged absorbance from part (A) calculated for the individual PEG-rich and DEX-rich compartments as functions of the corresponding concentration of SDS in each droplet. The filled circles correspond to the DEX-rich phase, the open circles correspond to the PEG-rich phase.

Figure 5.4 shows the 'unprocessed' and the 'processed' output of the inline spectrometer coupled to the millifluidic platform. The droplets contain SWCNT System A. The cross-sectional averaged optical absorbance across the FEP tubing is measured every 4 seconds at a wavelength of 653 nm. Figure 5.4 (A) shows the raw absorbance trace plotted as a function of time for a subset of 11 consecutive droplets. The trace is composed of a series of troughs, peaks, and

plateaus. Starting at the left of the plot, at 20250 s, the trough regions correspond to the absorbance signal from the perfluorocarbon continuous phase fluid between each droplet. The continuous phase fluid is chosen as the reference spectrum such that the absorbance of the fluid spacers is set to zero. Next, the absorbance sharply increases and then falls to a value of about 0.5 A.U. The spike corresponds to the curved cap region at the front of the droplet. The curvature and the contrast in refractive index of the droplet phase and the continuous phase fluids lead to refraction of light at the curved end caps of the droplet, which manifests as a sharp increase in the absorbance. Each droplet exhibits two absorbance plateaus, the first associated with the PEG-rich compartment and the second with the DEX-rich compartment. These appear as the two plateau regions between each trough in the absorbance trace. The height of each plateau changes from droplet to droplet. In the experiment shown in Figure 5.4, moving from earlier times to later times, the absorbance of the PEG-rich compartment at the beginning of each droplet increases, while the absorbance of the DEX-rich compartment decreases.

Comparing the absorbance trace to the droplet images in Figure 5.2 (B), it is clear that the spectrophotometer is able to discriminate the signal associated with the droplet and its internal compartments from one another and from the background.

The absorption measurements generate a significant amount of data for each droplet; between about 5 and 20 data points per polymer compartment within each droplet, plus additional points associated with endcap scattering. To extract useful information from this signal and more accurately compare the changes in

the PEG-rich and DEX-rich compartment absorbance, a time averaged absorbance for each compartment is calculated. This is accomplished by a custom MATLAB script that processes the absorbance trace in Figure 5.4 (A) and determines the position and width of each plateau inside each droplet compartment. All of the data points associated with a single plateau or trough are averaged to generate a single pair of absorbance and time data corresponding to either the DEX-rich phase, the PEG-rich phase, or the oil spacer. The end cap scatter is neglected. Next, the time axis is converted to surfactant concentration based on the total number of droplets generated and the surfactant flow-rate program assigned to the pumps, leading to an expected drop-by-drop concentration profile.

Figure 5.4 (B) is a plot of the time-averaged absorbance of each of the plateau regions shown in Figure 5.4 (A), plotted as a function of the corresponding overall SDS concentration in each droplet. The figure contains data for all 35 droplets generated in the gradient experiment. The open circles correspond to the absorbance of the DEX rich compartment, and the filled circles to the absorbance of the PEG-rich compartment. The absorbance of both compartments is flat between about 0.3 to 0.6 % (w/w) SDS. At approximately 0.6 % (w/w) SDS, the absorbance of both compartments begins to change; the absorbance of the DEX-rich compartment decreases by a factor of 3 to a value of 0.10 A.U. and the absorbance of the PEG-rich compartment increases from 0.05 to 0.12 A.U. At higher surfactant concentrations the absorbance of the compartments remains nearly constant.

Figure 5.4 shows that the average absorbance of each phase of the ATPS encapsulated within the droplets can be measured *via* inline spectrophotometry. The effect of increasing surfactant concentration on the partitioning of SWCNT System A is also clear. The semiconducting SWCNT species partition more strongly to the DEX-rich phase at low SDS concentration, and they partition more strongly to the PEG-rich phase at high SDS concentration.

Figures 5.1 and 5.2 show that the velocity of the droplets is a critical experimental parameter enabling a stable interface and accurate measurements. SWCNT partitioning in ATPSs is also known to be highly sensitive to temperature[33].
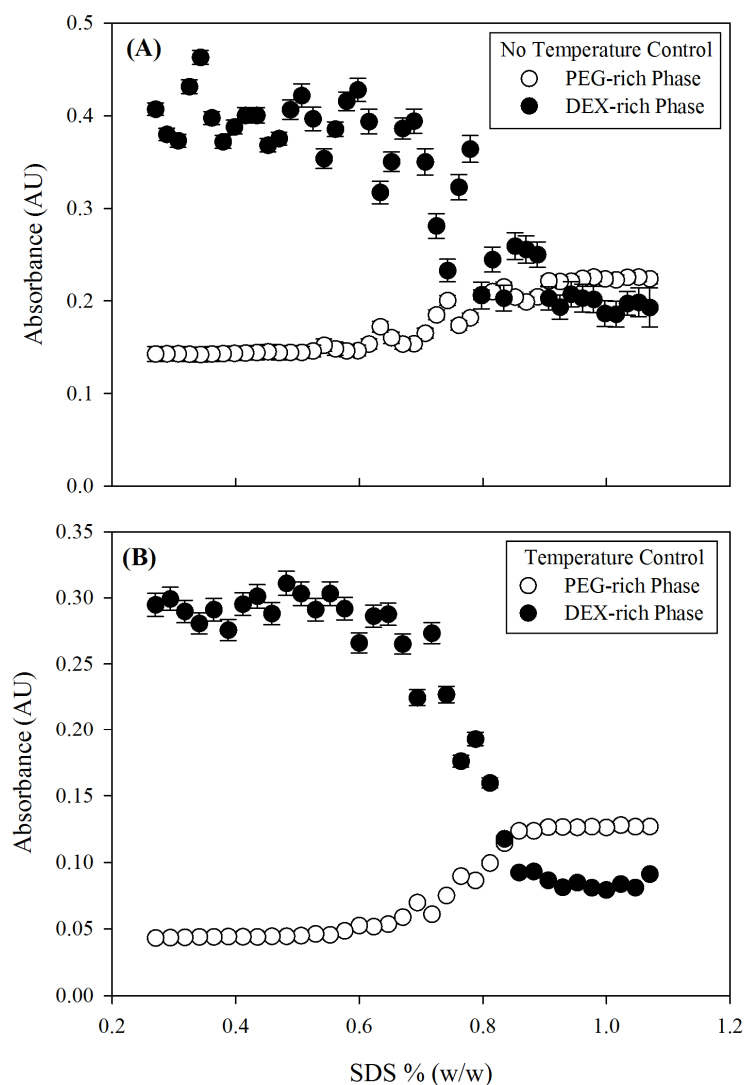
Figure 5.5. The effect of temperature on the absorbance of droplet compartments as a function of the corresponding concentration of SDS for two different partition experiments with EG150X semi-sorted SWCNTs. **(A)** Data for an experiment in which the temperature of the apparatus is not controlled (T ≈ 20 °C). **(B)** A partitioning experiment otherwise identical to (A), but in which the droplet generator and storage loop section is submerged in a temperature controlled bath set to approximately 20 ± 0.5° C.

Figure 5.5 shows the effect of temperature control on the absorbance of the PEG-rich and DEX-rich droplet compartments for a partitioning experiment with EG150X semi-sorted carbon nanotubes (System A). In Figure 5.5 (A) the partitioning experiment is conducted such that the ambient temperature at the start

of the experiment is approximately T ≈ 20 °C, but no special precautions are taken to control temperature fluctuations of the millifluidic apparatus that may occur over the next 10 hours of generation, storage, and measurement. At low SDS concentration, the absorbance of the DEX-rich compartments is noisy, with fluctuations of about ±0.1 A.U. Additionally, the PEG-rich compartment exhibits sinusoidal fluctuations in absorbance between about 0.6 and 0.8 % (w/w) SDS. In Figure 5.5 (B), data is plotted for a partitioning experiment with identical composition to that in (A), but in this case the droplet generator and the 2 m long tubing storage loop is submerged in a recirculating water bath in which the temperature is set to 20 ±0.5 °C. This is the same data that appears in Figure 5.4 (B), repeated here for comparison. Both the PEG-rich and DEX-rich compartment absorbance exhibit significantly smaller fluctuations over the same range of SDS concentration.

Figure 5.5 suggests that small fluctuations in temperature associated with, for example, cycling of the building heating and ventilation systems, has a significant, quantitative impact on the partitioning of SWCNTs at these experimental conditions. Sensitivity to temperature has been reported previously, and has been exploited to tune the separation of SWCNT species[33]. In both Figures 5.5 (A) and (B) the 1 m long vertical tubing detection section, including the optical flow cell, was not temperature controlled. Because phase separation and partitioning occur in the storage loop, Figure 5.5 suggests that once the nanotubes have partitioned and the phases have separated, the sensitivity to temperature is much less profound.

Figures 5.1 through 5.5 have described the operation of the millifluidic apparatus, the experimental parameters required for operation, and the method of collecting and analyzing data. The acquired data allow for estimation of partition coefficients for the mixtures of SWCNT species in each system considered. The partition coefficient for an aqueous two phase system is defined as the ratio of the concentration of a particular species in each of the two phases,

$$K = \frac{C_t}{C_b} \qquad (5.3)$$

where C is the concentration of a given partitioning species and the subscripts t and b refer to the 'top' and 'bottom' phases of an ATPS. Since the two phases settle due to density differences, the top phase corresponds to the PEG-rich phase while the bottom phase corresponds to the DEX-rich phase. This same density-driven configuration occurs in the millifluidic experiments due to the relative importance of gravitational forces compared with interfacial forces. The concentration is determined from the optical absorbance by applying the Beer-Lambert law,

$$A = \varepsilon C l \qquad (5.4)$$

where A is the absorbance, ε is the extinction coefficient, C is the concentration and l is the path length. A linear relationship between concentration and absorbance occurs at sufficiently dilute component concentrations. Since the exact concentration of the SWCNT samples is unknown, benchtop partitioning calibration experiments were conducted. It was found for the SWCNT

concentrations explored in this work the absorbance is linearly proportional to concentration. A linear relationship implies that the path length and the extinction coefficient of the SWCNT species are not needed to determine the partition coefficient, if we assume that the extinction coefficients are equal in both of the polymer-rich phases. Substituting equation 5.4 into 5.3 for each compartment yields an expression for K in terms of only the optical absorbance in each phase, $K = A_t/A_b$. This ratio is denoted the effective partition coefficient. The experimental analysis procedure described here has been used to determine the portioning coefficient for each of the three SWCNT systems listed in Table 5.1 as a function of SDS concentration.
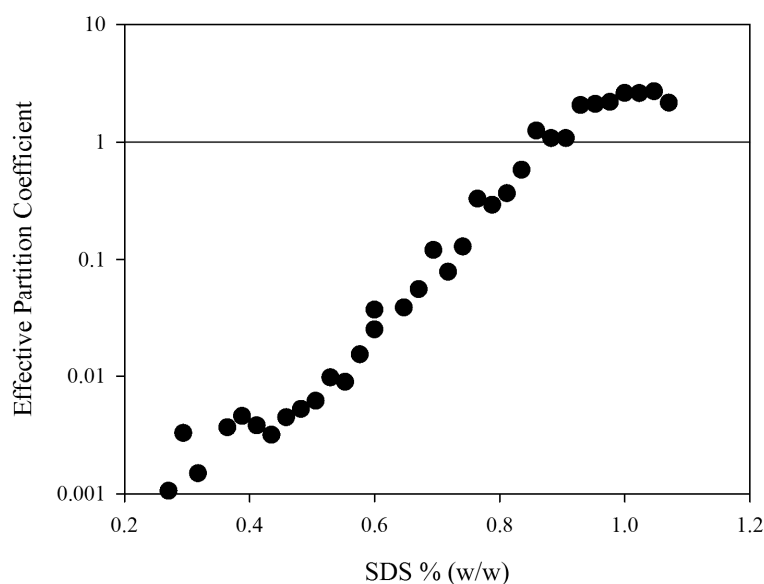
Figure 5.6. The effective partition coefficient for EG150X semi-sorted SWCNTs in an aqueous two phase system as a function of added SDS concentration. The data is obtained by subtracting the compartment absorbance from Figure 5.4 (B) from a baseline absorbance and then taking the ratio of the PEG-rich absorbance divided by the DEX-rich absorbance. The horizontal line at $K = 1$ is added to guide the eye, and indicates the effective partition coefficient at which the concentration of nanotubes is equal in each phase.

Figure 5.6 is a plot of the effective partition coefficient as a function of the corresponding overall SDS concentration for the EG150X semi-sorted SWCNT mixture, System A. For SDS concentrations from 0.3 to 1.07 % (w/w), the effective partition coefficient increases by almost 4 orders of magnitude, from about 0.001 to 3. Between about 0.85 and 1.07 % (w/w) SDS the magnitude of the partition coefficient is nearly independent of SDS concentration. The effective partition coefficient is calculated through a two-step procedure. First, the baseline absorbance of PEG-rich and DEX-rich compartments containing no SWCNTs is subtracted from the raw compartment absorbance data as shown in Figure 5.5 (B) to yield the absorbance, *A,* due solely to the presence of SWCNTs. The baseline absorbance acts as the reference spectrum and is associated with the optical absorbance of the polymers, surfactants, and water in each droplet compartment. It is obtained from separate experiments conducted in the millifluidic platform at the same flow conditions as the partitioning experiments. Next, the corrected PEG-rich absorbance is divided by the DEX-rich absorbance for each droplet to obtain the effective partition coefficient.

The millifluidic platform and experimental procedure capture the salient features of SWCNT partitioning in aqueous two phase systems. A small change in surfactant concentration results in a dramatic change, over nearly four orders of magnitude, in the effective partition coefficient associated with the species in System A that contribute to the optical absorbance signal at a wavelength of 653 nm. Because all three of the SWCNT Systems are mixtures of several different nanotube species, and the species contribute to the absorbance signal at multiple

wavelengths, the effective partition coefficients represent the net effect of more than one SWCNT type. However, this result still highlights the sensitivity and tunability of ATPS-based separations.

The range of surfactant concentration explored in the partitioning experiment can be adjusted by changing the volumetric flow rate of the syringes, or by changing the stock concentration of surfactant in the syringes.
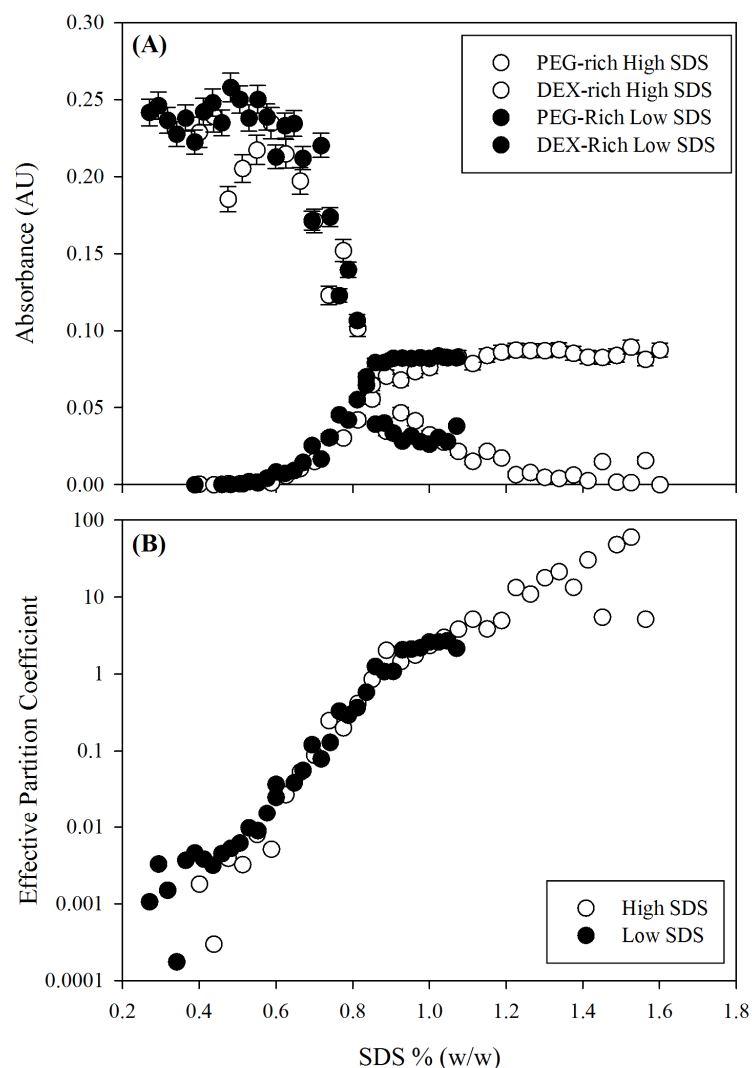
Figure 5.7. The average absorbance of the PEG-rich and DEX-rich compartments for two separate experiments with SWCNT System A spanning two different overlapping ranges of SDS concentration. In each plot, the 'Low SDS' data corresponds to concentrations from 0.27 to 1.07 % (w/w) SDS, the 'High SDS' data corresponds to concentrations from 0.4 to 1.6 % (w/w) SDS. **(A)** The average absorbance of the PEG-rich and DEX-rich compartments of each droplet. **(B)** The effective partition coefficient of the EG150X semi-sorted nanotubes (System A).

The two graphs in Figure 5.7 show the results of two separate partitioning experiments conducted in the millifluidic platform with EG150X semi-sorted SWCNTs (System A). Figure 5.7 (A) shows the raw average absorbance of the PEG-rich (squares) and DEX-rich (circles) compartments as a function of SDS concentration. The filled symbols correspond to the experiment shown in Figures

5.4 and 5.5 (B). The unfilled symbols are for an experiment in which the concentration range of added SDS was increased. Both sets of data overlap significantly, indicating excellent reproducibility of the measurement. At high SDS concentrations the absorbance of the PEG-rich phase is nearly constant while the absorbance of the DEX-rich phase continues to decrease to almost zero. The final absorbance of the PEG-rich compartments is approximately 0.09 A. U.

In the concentration range in which the two experiments overlap, the measured partition coefficients agree well. By accessing a greater range of SDS concentration, we find that the effective partition coefficient continues to increase with increasing SDS concentration, up to a maximum of approximately 100 at 1.60 % (w/w). This result demonstrates the reproducibility of the experimental procedure and the capability to obtain a wide range of partition coefficient values over a wide concentration range.

All of the partitioning results presented so far have been for the same sample containing a mixture of EG150X semi-sorted SWCNT (System A in Table 5.1). Figures 5.8 and 5.9 show the partitioning results for SWCNT Systems B and C.
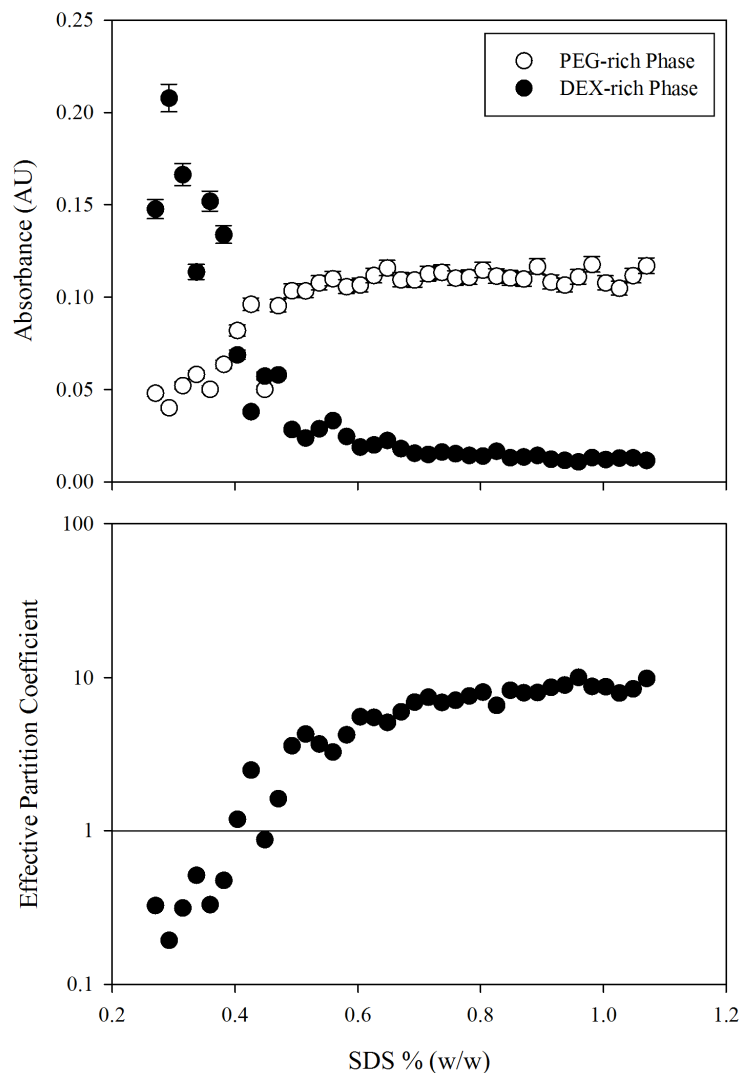
Figure 5.8. A plot of the effective partition coefficient as a function of the corresponding concentration of SDS for a series of multicomponent droplets containing EG150X metal-sorted SWCNTs. **(A)** The time-averaged absorbance of a series of PEG-rich and DEX-rich compartments with increasing amounts of added SDS. **(B)** The effective partition coefficients for the EG150X metal-sorted SWCNTs based on the data in part (A). The data was collected at conditions in which the temperature was not controlled (Similarly to Figure 5.5 (A)).

Figure 5.8 is a set of graphs of the averaged raw compartment absorbance and the estimated effective partition coefficient as functions of SDS concentration for a partitioning experiment with EG150X metal-sorted SWCNTs. In Figure 5.8 (A) the absorbance of the PEG-rich compartments increases by a factor of approximately 3, while the absorbance of the DEX-rich compartments decreases

by an order of magnitude over the same range of SDS composition. The crossover of the absorbance profiles occurs at approximately 0.4 % (w/w) SDS. In Figure 5.8 (B) the effective partition coefficient estimated from the data in part (A) is plotted as a function of SDS composition. The partition coefficient increases by approximately 2 orders of magnitude from about $K = 0.1$ at 0.27 % (w/w) SDS to $K = 10$ at 0.6 % (w/w) SDS. From 0.6 to 1.07 % (w/w) SDS the partition coefficient is approximately constant at $K = 10$.
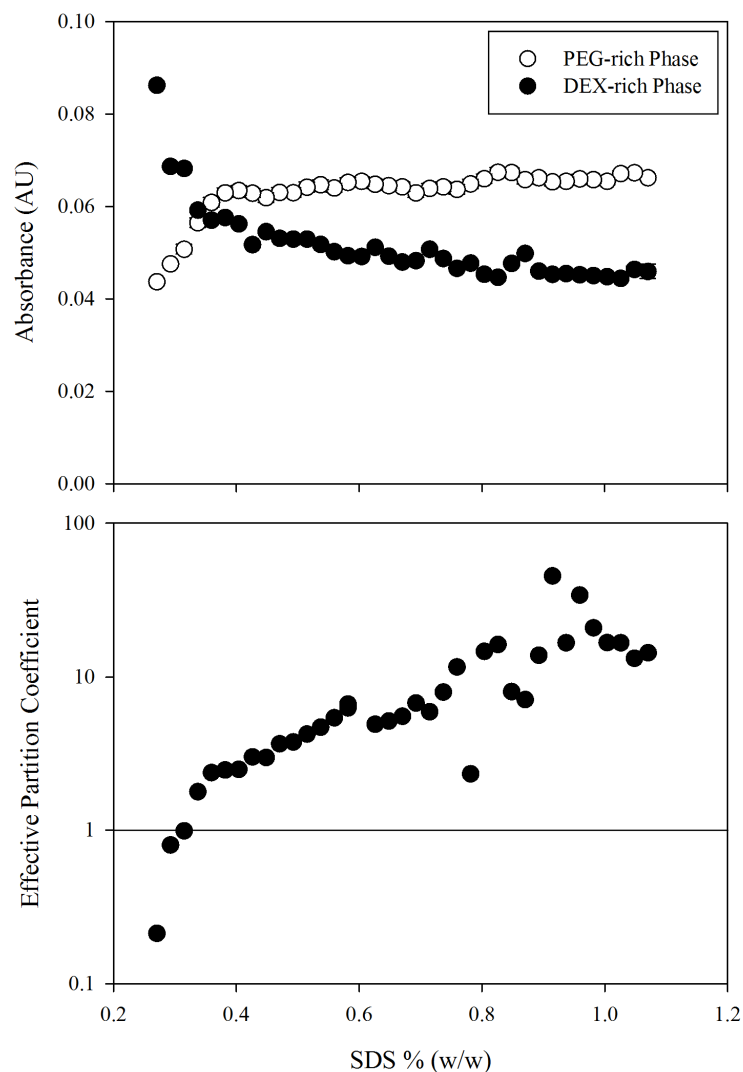
Figure 5.9. A plot of the effective absorbance and partition coefficient as a function of the corresponding concentration of SDS for a series of multicomponent droplets containing the Raymor metal-sorted SWCNT sample. The overall concentration of DOC in each droplet is fixed at 0.07 % (w/w). **(A)** The time-averaged absorbance of a series of PEG-rich and DEX-rich compartments with increasing amounts of added SDS. **(B)** The effective partition coefficients for the Raymor metal-sorted SWCNTs based on the data shown in part (A). The data was collected at conditions in which the temperature was not controlled.

Figure 5.9 is a set of graphs of the raw compartment absorbance and the resulting effective partition coefficient for a system containing Raymor metal-sorted SWCNTs. In Figure 5.9 (A) the absorbance of the DEX-rich and PEG-rich phases is qualitatively similar to the other nanotube samples. The DEX-rich phase

exhibits its maximum absorbance at 0.27 % (w/w) SDS, decreases with increasing SDS concentration, and then levels off. The PEG-rich phase shows the opposite behavior, with the absorbance of the compartment increasing with increasing SDS concentration up to about 0.06 A.U. at 0.4 % (w/w) SDS, at which point the value becomes constant. The crossover in the absorbance values occurs at about 0.035 % (w/w) SDS. In Figure 5.9 (B), the effective partition coefficient as a function of the corresponding SDS concentration is plotted for the data shown in part (A). The data is noisy, but the effective partition coefficient appears to increase by nearly 3 orders of magnitude from about $K = 0.01$ to approximately $K = 90$ with a threefold increase in SDS concentration from 0.27 to 1.07 % (w/w).

The concentration crossover point for the absorbance of both the EG150X metal-sorted and the Raymor metal-sorted SWCNT samples is a factor of two lower in SDS concentration than the EG150X semi-sorted samples. The overall increase in partition coefficient for both samples is smaller, varying by approximately two orders of magnitude as compared to the four decades observed for the EG150X sample. These results agree with previous reports suggesting that metallic carbon nanotubes partition at lower SDS concentrations for a fixed concentration of DOC compared with semiconducting nanotubes[31,33].

5.4   Conclusions

We have successfully developed a platform and methodology to generate ultra-low interfacial tension multi-compartment droplets composed of phase separating polymer solutions. The compartments of the droplets are initially well mixed and then allowed to phase separate and spatially segregate within a parent droplet. Careful control of the droplet velocity and physical orientation with respect to gravity maintains the stability of the interface between the two phases. Using the apparatus and the inline UV/Vis spectrophotometer we accurately and reproducibility measure the absorbance of species that partition between the two phases encapsulated inside a microliter-scale droplet. From this data we estimate an effective partition coefficient as a function of composition more quickly, more autonomously, and with greater compositional resolution than typical macroscale techniques. Specifically, we find that metal sorted SWCNTs partition more strongly into the PEG-rich phase at much lower SDS concentrations than the Semi-sorted SWCNT species, in agreement with previously reported partitioning results obtained from macroscale separation experiments.

5.5   References

1.   Monthioux, M. & Kuznetsov, V. L. Who should be given the credit for the discovery of carbon nanotubes? *Carbon N. Y.* **44,** 1621–1623 (2006).

2.   Baughman, R. H., Zakhidov, A. a & de Heer, W. a. Carbon nanotubes--the route toward applications. *Science* **297,** 787–92 (2002).

3.   Harris, P. J. F. Carbon nanotube composites. *Int. Mater. Rev.* **49,** 31–43 (2004).

4.   Franklin, A. D. *et al.* Sub-10 nm carbon nanotube transistor. *Nano Lett.* **12,** 758–62 (2012).

5.   Lee, N. S. *et al.* Application of carbon nanotubes to field emission displays. *Diam. Relat. Mater.* **10,** 265–270 (2001).

6.   Cheng, H.-M., Yang, Q.-H. & Liu, C. Hydrogen storage in carbon nanotubes. *Carbon N. Y.* **39,** 1447–1454 (2001).

7.   Mubarak, N. M., Abdullah, E. C., Jayakumar, N. S. & Sahu, J. N. An overview on methods for the production of carbon nanotubes. *J. Ind. Eng. Chem.* **20,** 1186–1197 (2014).

8.   Belin, T. & Epron, F. Characterization methods of carbon nanotubes: a review. *Mater. Sci. Eng. B* **119,** 105–118 (2005).

9.   Arnold, M. S., Green, A. a, Hulvat, J. F., Stupp, S. I. & Hersam, M. C. Sorting carbon nanotubes by electronic structure using density differentiation. *Nat. Nanotechnol.* **1,** 60–65 (2006).

10.   Tu, X., Manohar, S., Jagota, A. & Zheng, M. DNA sequence motifs for structure-specific recognition and separation of carbon nanotubes. *Nature* **460,** 250–3 (2009).

11.   Khripin, C. *et al.* High-Resolution Length Fractionation of Surfactant-Dispersed Carbon Nanotubes. *Anal. Chem.* 121223104234008 (2012). at <http://pubs.acs.org/doi/abs/10.1021/ac303349q>

12.   Tu, X., Hight Walker, A. R., Khripin, C. Y. & Zheng, M. Evolution of DNA sequences toward recognition of metallic armchair carbon nanotubes. *J. Am. Chem. Soc.* **133,** 12998–13001 (2011).

13.   Silvera-Batista, C. a., Scott, D. C., McLeod, S. M. & Ziegler, K. J. A Mechanistic Study of the Selective Retention of SDS-Suspended Single-Wall Carbon Nanotubes on Agarose Gels. *J. Phys. Chem. C* **115,** 9361–9369 (2011).

14.   Liu, H., Nishide, D., Tanaka, T. & Kataura, H. Large-scale single-chirality separation of single-wall carbon nanotubes by simple gel chromatography.

Nat. Commun. **2,** 309 (2011).

15. Liu, H., Tanaka, T., Urabe, Y. & Kataura, H. High-efficiency single-chirality separation of carbon nanotubes using temperature-controlled gel chromatography. *Nano Lett.* **13,** 1996–2003 (2013).

16. Tvrdy, K. *et al.* A Kinetic Model for the Deterministic Prediction of Gel-Based Single Chirality Single-Walled Carbon Nanotube Separation. *ACS Nano* 1779–1789 (2013). doi:10.1021/nn305939k

17. Flavel, B. S., Kappes, M. M., Krupke, R. & Hennrich, F. Separation of single-walled carbon nanotubes by 1-dodecanol-mediated size-exclusion chromatography. *ACS Nano* **7,** 3557–3564 (2013).

18. Ghosh, S., Bachilo, S. M. & Weisman, R. B. Advanced sorting of single-walled carbon nanotubes by nonlinear density-gradient ultracentrifugation. *Nat. Nanotechnol.* **5,** 443–450 (2010).

19. Cambré, S. & Wenseleers, W. Separation and Diameter-Sorting of Empty (End-Capped) and Water-Filled (Open) Carbon Nanotubes by Density Gradient Ultracentrifugation. *Angew. Chemie Int. Ed.* **50,** 2764–2768 (2011).

20. Green, A. A. & Hersam, M. C. Nearly single-chirality single-walled carbon nanotubes produced via orthogonal iterative density gradient ultracentrifugation. *Adv. Mater.* **23,** 2185–2190 (2011).

21. Fagan, J. A. *et al.* Separation of empty and water-filled single-wall carbon nanotubes. *ACS Nano* **5,** 3943–3953 (2011).

22. Fagan, J. A. *et al.* Analyzing Surfactant Structures on Length and Chirality Resolved (6,5) Single-Wall Carbon Nanotubes by Analytical Ultracentrifugation. *ACS Nano* **7,** 3373–3387 (2013).

23. Ihara, K., Endoh, H., Saito, T. & Nihey, F. Separation of metallic and semiconducting single-wall carbon nanotube solution by vertical electric field. *J. Phys. Chem. C* **115,** 22827–22832 (2011).

24. Witkowski, P., Smith, J. A., Fusillo, T. V. & Chiou, C. T. A review of surface-water sediment fractions and their interactions with persistent manmade organic compounds. *USGS Circ.* (1987).

25. Albertsson, P. Å. *Partition of Cell Particles and Macromolecules.* (John Wiley & Sons, 1986).

26. Zaslavsky, B. Y. *Aqueous Two-Phase Partitioning.* (Marcel Dekker, 1994).

27. Liu, Y., Lipowsky, R. & Dimova, R. Concentration dependence of the interfacial tension for aqueous two-phase polymer solutions of dextran and polyethylene glycol. *Langmuir* **28,** 3831–9 (2012).

28.   Forciniti, D., Hall, C. K. & Kula, M. R. Interfacial tension of polyethyleneglycol-dextran-water systems: influence of temperature and polymer molecular weight. *J. Biotechnol.* **16,** 279–296 (1990).

29.   Ryden, J. & Albertsson, P. Interfacial tension of dextran—polyethylene glycol—water two—phase systems. *J. Colloid Interface Sci.* **37,** 219–222 (1971).

30.   Berggren, K., Wolf, A., Asenjo, J. a, Andrews, B. a & Tjerneld, F. The surface exposed amino acid residues of monomeric proteins determine the partitioning in aqueous two-phase systems. *Biochim. Biophys. Acta* **1596,** 253–68 (2002).

31.   Khripin, C. Y., Fagan, J. A. & Zheng, M. Spontaneous Partition of Carbon Nanotubes in Polymer-Modified Aqueous Phases. *J. Am. Chem. Soc.* **135,** 6822–6825 (2013).

32.   Zhang, M. *et al.* Single-Step Total Fractionation of Single-Wall Carbon Nanotubes by Countercurrent Chromatography. *Anal. Chem.* **86,** 3980–3984 (2014).

33.   Fagan, J. a *et al.* Isolation of Specific Small-Diameter Single-Wall Carbon Nanotube Species via Aqueous Two-Phase Extraction. *Adv. Mater.* **26,** 2800–2804 (2014).

34.   Subbaiyan, N. K. *et al.* Role of Surfactants and Salt in Aqueous Two-Phase Separation of Carbon Nanotubes toward Simple Chirality Isolation. *ACS Nano* **8,** 1619–1628 (2014).

35.   Fagan, J. A. *et al.* Isolation of >1 nm Diameter Single-Wall Carbon Nanotube Species Using Aqueous Two-Phase Extraction. *ACS Nano* **9,** 5377–5390 (2015).

36.   Subbaiyan, N. K. *et al.* Bench-top aqueous two-phase extraction of isolated individual single-walled carbon nanotubes. *Nano Res.* **8,** 1755–1769 (2015).

37.   Gui, H. *et al.* Redox Sorting of Carbon Nanotubes. *Nano Lett.* **15,** 1642–1646 (2015).

38.   Wei, L. *et al.* (9,8) Single-Walled Carbon Nanotube Enrichment via Aqueous Two-Phase Separation and Their Thin-Film Transistor Applications. *Adv. Electron. Mater.* **1,** n/a–n/a (2015).

39.   Vaisman, L., Wagner, H. D. & Marom, G. The role of surfactants in dispersion of carbon nanotubes. *Adv. Colloid Interface Sci.* **128-130,** 37–46 (2006).

40.   Arnold, M. S., Suntivich, J., Stupp, S. I. & Hersam, M. C. Hydrodynamic characterization of surfactant encapsulated carbon nanotubes using an

analytical ultracentrifuge. *ACS Nano* **2,** 2291–300 (2008).

41.   Lin, S. & Blankschtein, D. Role of the bile salt surfactant sodium cholate in enhancing the aqueous dispersion stability of single-walled carbon nanotubes: a molecular dynamics simulation study. *J. Phys. Chem. B* **114,** 15616–25 (2010).

42.   Trivedi, V. *et al.* A modular approach for the generation, storage, mixing, and detection of droplet libraries for high throughput screening. *Lab Chip* **10,** 2433 (2010).

43.   Lorber, N., Pavageau, B. & Mignard, E. Droplet-Based Millifluidics as a New Miniaturized Tool to Investigate Polymerization Reactions. *Macromolecules* **43,** 5524–5529 (2010).

44.   Hodges, S. R., Jensen, O. E. & Rallison, J. M. The motion of a viscous drop through a cylindrical tube. *J. Fluid Mech.* **501,** 279–301 (2004).

45.   Ma, S. *et al.* On the flow topology inside droplets moving in rectangular microchannels. *Lab Chip* **14,** 3611–3620 (2014).

46.   Kinoshita, H., Kaneda, S., Fujii, T. & Oshima, M. Three-dimensional measurement and visualization of internal flow of a moving droplet using confocal micro-PIV. *Lab Chip* **7,** 338–46 (2007).

47.   Prat, L. *et al.* Experimental and Numerical Study of Droplets Hydrodynamics in Microchannels. **52,** (2006).

48.   Hui Sophia Lee, S., Wang, P., Kun Yap, S., Alan Hatton, T. & Khan, S. a. Tunable spatial heterogeneity in structure and composition within aqueous microfluidic droplets. *Biomicrofluidics* **6,** 22005–220058 (2012).

49.   Bentley, B. J. & Leal, L. G. An experimental investigation of drop deformation and breakup in steady, two-dimensional linear flows. *J. Fluid Mech.* **167,** 241 (1986).

50.   Squires, T. M. & Quake, S. R. Microfluidics: Fluid physics at the nanoliter scale. *Rev. Mod. Phys.* **77,** 977–1026 (2005).

51.   Gonzalez-Tello, P., Camacho, F. & Blazquez, G. Density and Viscosity of Concentrated Aqueous Solutions of Polyethylene Glycol. *J. Chem. Eng. Data* **39,** 611–614 (1994).

52.   Menech, M. De & Garstecki, P. Transition from squeezing to dripping in a microfluidic T-shaped junction. *J. Fluid …* 1–17 (2008). at <http://journals.cambridge.org/production/action/cjoGetFulltext?fulltextid=1624252>

53.   Christopher, G. F., Noharuddin, N. N., Taylor, J. a. & Anna, S. L. Experimental observations of the squeezing-to-dripping transition in T-

shaped microfluidic junctions. *Phys. Rev. E* **78,** 1–12 (2008).

Chapter 6. Conclusions and Future Work

The precision fluid manipulation techniques afforded by micrometer and millimeter scale flow allow for the measurement of critical material properties of complex fluids, such as interfacial tension and partition coefficients, with greater speed, ease of use, and lower cost than many traditional screening techniques. This thesis has shown that millifluidic devices in particular allow for quantitative measurement of changes in phase behavior and partitioning in multi-phase systems and we have developed several platforms suitable for probing these phenomena. However, due to the enhanced importance of interfacial forces, at these smaller length scales, special care must be taken in the design, construction, and operation of millifluidic and microfluidic devices. This is especially important when mixing multiple components inside droplets, or when choosing materials that will support droplet-based flow of phase forming materials.

In **Chapter 2** we utilize a microfluidic platform for controllably inducing phase separation in initially homogenous polymer-polymer and polymer-salt solutions, and then calculate the very low interfacial tension of the resulting aqueous-aqueous interface. These two tasks are accomplished simultaneously in a single experimental step. By optically measuring the contact angles of compound nanoliter-scale droplets we estimate the interfacial tension of a polyethylene glycol/sodium sulfate or a polyethylene glycol/dextran two phase system as a function of the total concentration of the phase forming components. The increase in interfacial tension with increasing total polymer concentration follows a power law behavior, in good agreement with previously reported models. Further, the

164

device was used to accurately determine the critical concentration for the specific two phase system considered, providing a method to determine phase diagrams.

In **Chapter 3** we present a droplet-based fluid handling technique based on previously published reports of 'millifluidic' devices in which established microfluidic techniques are scaled up and devices are assembled using off the shelf tubing and components. We describe the equations governing the composition of droplets generated in such an apparatus, provide examples for construction and assembly, and perform proof-of-concept experiments to verify the ability to generate trains of droplets with a linear gradient in the composition of one or more components. The composition inside the droplets is probed using in situ absorption spectroscopy, which is possible only because of the increased diameter of the fluid channels and therefore the increased optical path length for detection.

In **Chapter 4** we apply the millifluidic platform developed in Chapter 3 to generate multi-scale emulsions to address an industrially relevant problem. Millimeter scale water-in-perfluorocarbon droplet compartments are generated to encapsulate a micron scale dilute crude-oil-in-water emulsion. Uniquely, the dilute microscale emulsion was prepared by benchtop homogenization, and then formed into the aqueous droplet compartments using syringe pumps. The device is used to quickly and quantitatively measure the effect of water clarifiers (cationic polyelectrolytes) on the stability of a synthetic produced water emulsion. The millifluidic platform exhibits compositional resolution an order of magnitude better than typical macroscale 'bottle tests,' which allows for more precise

determination of the ideal concentration of clarifier. It is found that the concentration of clarifier required to obtain a change in the time-averaged absorbance signal of the droplet compartments decreased with increasing clarifier molecular weight. Additionally, the platform was used to probe the effect of salinity on the stability of the emulsions by dosing droplets with varying concentrations of either sodium chloride or calcium chloride.

In **Chapter 5** we adapt the millifluidic platform from Chapter 3 to generate multi-compartment droplets composed of a phase separated aqueous two phase polymer system. By carefully designing the experiment we are able to thoroughly mix and then spatially separate the two polymer-rich phases of an aqueous two phase system that are encapsulated inside an $8 - 10$ microliter droplet. The concentration of a single surfactant component is varied from droplet to droplet in order to modulate the partition coefficient of carbon nanotubes dispersed in the two phase system. In agreement with the available literature, it is found that the nanotubes generally partition more strongly into the DEX-rich phase at low concentrations of SDS, and more strongly into the PEG-rich phase at higher SDS concentrations. The PEG-rich phase of the aqueous two phase system known to be slightly less hydrophilic than the DEX-rich phase. The partitioning behavior we observe is thought to be a result of the changes in the net hydrophobicity of the SWCNTs that occur in response to the addition of excess SDS. At low SDS concentration, the SWCNTs are primarily covered with DOC, which has been previously reported to be a more hydrophilic dispersant for SWCNTs. As a result, the nanotubes remain in the DEX-rich phase. At high SDS

concentrations, the mixed surfactant micelles, which assemble on the surface of the SWCNTs, become dominated by SDS, which leads to nanotubes with slightly lower hydrophobicity than their DOC-wrapped counter parts. The nanotubes wrapped with more SDS partition in into the PEG-rich phase. The critical concentration at which the partitioning is equal is lower for the metal-sorted nanotube species than for the semiconductor sorted nanotube species. Importantly, this method is much faster and less error prone than the current benchtop methodologies for measuring partition coefficients.

The **primary contribution** of this thesis is the development of tools, techniques, and methodologies tailored to probing the phase behavior of complex fluid systems. The relatively small change in the length scales moving from microfluidics to millifluidics, as discussed in Chapters 3, 4, and 5, facilities the use of facile and low cost optical measurement techniques, such as absorption spectroscopy, while dramatically simplifying the design and construction of droplet-based fluid manipulation devices. Further, the slight increase in characteristic length allows for greater control over the relative impact of interfacial forces, inertia, and gravity, while stilling providing the droplet generation procedures associated with laminar microscale flow. Careful selection of the continuous phase fluid, the presence of surfactants, and the imposed fluid velocity enable the platform to operate over a range of Reynolds, capillary, and Bond numbers, including regimes where these dimensionless groups are of the order 0.01 to 10. This flexibility allows better control of mixing, and allows fine tuning the effect of forces such as gravity to one's advantage. The potential

impact of this work lies in its ability to enable high throughput, high resolution screening of critical parameters such as partition coefficients. Knowledge of this information can aid design of products and processes that exploit complex fluid systems, such in separations, or the design of additives to modify phase separation.

Future Work

There is significant opportunity for further study for the projects presented in Chapters 2, 4, and 5. For example, in Chapter 2, interfacial tension is estimated for systems that contained only two components: the two phase forming polymers. The effect of additives on the interfacial tension and phase separation of these systems is of considerable interest. Adding salts and water soluble surfactants to the droplets would yield practically valuable and fundamentally important data. There are also modifications to the design of the device that would allow for more data to be collected per experiment. Currently the concentration of the 40 droplets in each array is identical. This is beneficial for collecting statistics regarding stochastic processes, but if the composition of the droplets could be modified droplet-to-droplet, and then all of the droplets dehydrated as described, each experiment would yield a three parameter plot.

The work of Chapter 4 could be extended and more fundamental structure-property relationships established by systematically probing the effect of non-proprietary polyelectrolytes on model oil-in-water emulsions, rather than actual crude oil samples.

In Chapter 5, the work presented in this thesis lays the foundation for substantial additional research. The apparatus was able to generate 30 -40 partition coefficients in about a day, compared to the weeks required for benchtop scale methods, and with very good reproducibility. Application of this platform to additional SWCNT samples would dramatically expand the information available for tuning aqueous two phase extraction of nanotubes, and provide data for developing a better fundamental understanding of the partitioning process. The first step for extending the work of Chapter 5 might be to obtain higher purity SWCNT samples containing as few individual SWCNT species as possible. With only one or two species present, correlating absorbance data to specific species, and thus to specific chiral vectors, would be significantly easier. Partitioning phase diagrams for each chirality could be generated as a function of two surfactants and temperature. For SWCNT samples containing a diversity of species, integrating photoluminescence excitation or Raman spectroscopy with the droplet based platform would allow for the precise determination of the partition coefficients of every species present in the sample as a function of surfactant concentration. Additionally, as was described in the chapter, temperature is a critical parameter for phase separation. The low thermal mass of the tubing and droplets as the exist in the platform would allow precise control of the temperature, or for the droplets to experience multiple temperatures. Currently, no data is available regarding the effect of the molecular weight or type of phase forming polymers used to construct the aqueous two phase system. It

seems unlikely that PEG and DEX are the ideal choice in all cases. The platform

described in Chapter 5 is well suited to answering these types of questions.